USE OF FINITE ELEMENT METHOD TO EVALUATE THE STRENGTH RESPONSE OF NOTCHED COMPOSITE LAMINATES UNDER TENSION

By

ARJUN KOTHIDAR

A thesis submitted in partial fulfillment of
the requirements for the degree of

MASTER OF SCIENCE IN MECHANICAL ENGINEERING

WASHINGTON STATE UNIVERSITY
Department of Mechanical and Materials Engineering

December 2008

To the Faculty of Washington State University:

The members of the Committee appointed to examine the thesis of ARJUN KOTHIDAR find it satisfactory and recommend that it be accepted.

_____

Chair

_____

_____

ACKNOWLEDGEMENT

I would like to thank my advisor, Dr. Lloyd V. Smith, for providing me the opportunity to work on this project. He has provided the resources, encouragement and freedom to explore, and his expertise and counsel are greatly appreciated. In addition, thanks are due to my thesis committee, Dr. Jow-Lian Ding and Dr. Vikram Yadama who have been very patient and supportive throughout my work. I would like to thank Daniel P. Stone, my project partner for this project for all his work and discussions.

Thanks to Miles Peppers and Henry Ruff for their assistance in the area of composite fabrication. Thank you to the MME staff, including Mary Simonsen, Bob Ames, Gayle Landeen and Robert Lentz whose helpful nature made life really easy during the course of my study. I'd like to thank Giac Pham and Micheal Shook for their help and competence with technical issues. Thank you to all the undergraduate students of ETRL 122 LAB who have helped me throughout this project, including Brian Seater, Tyler Start, Matthew Jorgensen and Alex Butterfield.

Lastly, and most importantly I would like to thank my family who have been very encouraging throughout my years of learning.

USE OF FINITE ELEMENT METHOD TO EVALUATE THE STRENGTH RESPONSE OF NOTCHED COMPOSITE LAMINATES UNDER TENSION

Abstract

by Arjun Kothidar, M.S.
Washington State University
December 2008

Chair: Lloyd V. Smith

Mechanical attachments can reduce the strength of composites substantially. The following considers the sensitivity of open-hole tension (OHT) test coupons to the laminate fiber orientation. Fiber orientation affects the stress distribution around the hole which can lead to improved laminate strength.

The effect of the hole on the OHT strength was described numerically by using a 3D Finite Element (FE) model. The linear elastic model was used to predict the first ply failure (FPF). Maximum Stress and Maximum Strain failure criteria were found to correlate well with the measured FPF strength and location as verified by SEM.

The results of the 3D model were used with Quadratic Delamination Criterion. The procedure was successful in identifying laminates with delamination failure modes as identified through SEM.

An FE based Representative Volume Element (RVE) has been used to evaluate the homogenized elastic properties of a graphite/epoxy composite material from its constituent properties. The model agreed well with the experimentally obtained elastic properties of the composite lamina. The FE based RVE model approach was found to be

an improvement over the existing analytical and semi-empirical methods, as a single model could be used to generate all the elastic properties of the composite material.

TABLE OF CONTENTS

Page

LIST OF TABLES

LIST OF FIGURES

1. Literature Review

1.1 Introduction

An important problem when designing with composites is that of stress concentrations arising near discontinuities. Knowledge of the magnitude and extent of stress concentrations in these structures is crucial for determining the location of first failure and subsequent damage propagation [1]. This work aims to establish the importance of matrix induced failure in form of the first ply failure in the design of notched laminated composites.

1.2. Terminology

A lamina or ply is a plane (or curved) layer of unidirectional fibers or woven fabric in a matrix. In the case of unidirectional fibers, it is also referred to as unidirectional lamina (UD). The lamina is an orthotropic material with principal material axes in the direction of fibers (longitudinal), normal to the fibers in the plane of lamina (in-plane transverse) and normal to the plane of the lamina. The principal axes are designated as 1, 2 and 3 respectively as shown in Fig. 1.2.1.

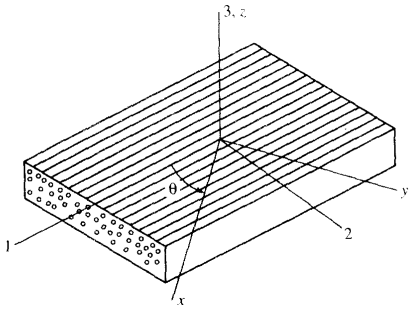

Fig. 1.2.1 Orthotropic lamina with principal and non-principal coordinate system [3]

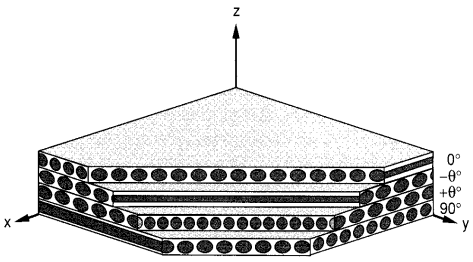

Fig.1.2.2 Multidirectional laminate with reference (non-principal) coordinate system [3]

A laminate is made up of two or more unidirectional laminae or plies stacked together at various orientations as shown in Fig.1.2.2. The laminae can be of various thicknesses and consist of

different materials. Since the orientation of the principal material axes varies from ply to ply, sometimes it is convenient to analyze laminates using a common reference coordinate system (x, y, z). The orientation of a ply is given by the angle between the reference and the major principal material axis measured in a counter clock wise direction on the x-y plane as shown in Fig. 1.2.2. The configuration of the laminate indicating its ply composition is called a lay-up. The configuration indicating, in addition to the ply composition, the exact location of the various plies is called the stacking sequence. Composite laminates are designated in a manner indicating the number, type, orientation and stacking sequence of plies. Some of the commonly used laminate configurations along with their names are provided in Table 1.2.1[3].

Table 1.2.1 Stacking sequence of some of the commonly used laminates [3]

Nomenclature	Stacking Sequence
Unidirectional six-ply	$[0/0/0/0/0/0]=\left[0_6\right]$
Cross Ply	$[0/90/90/0]=[0/90]_s$
Angle-ply symmetric	$[\beta/-\beta/-\beta/\beta]=[\pm\beta]_s$
Angle-ply asymmetric	$[\beta/-\beta/\beta/-\beta/\beta/-\beta]=[\pm\beta]_3$
Multidirectional	$[0/\beta/-\beta/-\beta/\beta/0]=[0/\pm\theta]_s$ $[0/\beta/-\beta/90/90/-\beta/\beta/0]=[0/\pm\theta/90]_s$

In Table 1.2.1 β is the ply angle that has values between 0 and 90 degrees and s indicates symmetric sequence. The slash mark is used to indicate separate lamina orientations with the subscript indicating the number of laminae of the same orientation. The laminae are specified with the one next to the mold surface written first [4]. The laminates used for this thesis are symmetric and balanced. Symmetric laminates are specified by listing only top half of the laminate and by using the subscript "s" outside the brackets. A laminate is balanced if it consists of pairs of layers with identical thickness but having + (plus) and – (minus) β orientation of their

principal material axes with respect to the laminate principal axes. This prevents warpage or unexpected distortions, after the cure cycle is complete and reduces interlaminar stresses.

1.3 Effect of fiber orientation on stress concentration

Investigators [5-13] have used two basic approaches to address the problem of stress concentration around circular cut-outs in composite plates. In one approach [1-5] the problem has been treated analytically by the theory of linear anisotropic elasticity as developed by Lekhnitskii [14]. Based on this approach models have been developed to predict the effect of the notch size on the tensile strength of composites [15-17]. In another approach [10-12], numerical methods such as finite element analysis have been employed. Greszezuk [7] observed that the strength of the composite plates with cut-outs is less sensitive to the stress concentration than plates made of isotropic materials. Tan [5] observed that the stress concentration factor in graphite/epoxy angle-ply laminates could be greater than that of the isotropic case depending on the fiber orientation.

Whitworth, H.A. and Mahase, H. [17] investigated stress concentrations in graphite/epoxy composite plates containing a circular hole. The plates were subjected to unidirectional loading. The study was based on unidirectional laminates with oriented fibers, balanced symmetric angle-ply, cross-ply and $[0/\pm\beta/90]s$ laminates. The authors [17] used the approach of Lekhnitskii to evaluate the stress concentration in graphite/epoxy laminates of varying fiber orientation subjected to uniaxial tension. Some of the important details of their method are discussed below.

1.3.1 Stress Analysis

According to classical lamination plate theory, the strain and resultant force per unit length relation in an orthotropic plate loaded in the plane of the plate is given by:

$$\begin{bmatrix} \varepsilon_x \\ \varepsilon_y \\ \gamma_{xy} \end{bmatrix} = \begin{bmatrix} A'_{11} & A'_{12} & A'_{16} \\ A'_{12} & A'_{22} & A'_{26} \\ A'_{16} & A'_{26} & A'_{66} \end{bmatrix} \begin{bmatrix} N_x \\ N_y \\ N_{xy} \end{bmatrix} \tag{1.3.1}$$

where A'_{ij} is the elastic compliance matrix and is computed from the stiffness coefficient $\bar{Q}_{ij}$ transformed into the x, y, z coordinate system of the individual lamiae by

$$\left(A'_{ij}\right)^{-1} = A_{ij} = \sum_{k=1}^{n} \bar{Q}_{ij}^{\,k} \left(h_{k+1} - h_k\right) \tag{1.3.2}$$

where h is the plate thickness.

From the Lekhnitskii's theory of two dimensional anisotropic elasticity, the stress function F(x, y) satisfying the equilibrium and compatibility condition is the solution of the biharmonic equation

$$A'_{22} \frac{\partial^4 F}{\partial x^4} + \left(2A'_{12} + A'_{66}\right) \frac{\partial^4 F}{\partial x^2 \partial y^2} + A'_{11} \frac{\partial^4 F}{\partial y^4} = 0 \tag{1.3.3}$$

The laminates were loaded uniaxially (N_x= p, N_y= 0, N_{xy}= 0) at an angle ϕ to the principal axis to the plate as shown in Fig.1.3.1 and Fig.1.3.2. The circumferential stress on the boundary of the hole is given by the expression

$$\sigma_\theta = p \frac{A'_{11}}{A'_\theta} \left\{ \begin{array}{l} \left[\cos^2\phi + \left(\mu_1\mu_2 - n\right)\sin^2\phi\right]\mu_1\mu_2\cos^2\phi \\ + \left[\left(1+n\right)\cos^2\phi + \mu_1\mu_2\sin^2\phi\right]\sin^2\phi - n\left(1+n-\mu_1\mu_2\right)\sin\phi\cos\theta\sin\phi\cos\theta \end{array} \right\} \tag{1.3.4}$$

where θ is the location around the hole measured from the principal axis of the plate and μ_1 and μ_2 are roots of the characteristic equation

$$A'_{11}\mu^4 + \left(A'_{66} - 2A'_{12}\right)\mu^2 + A'_{22} = 0 \tag{1.3.5}$$

In equation 1.3.4, the compliance A'_{θ} in a direction tangent to the opening can be obtained from

$$A'_{\theta} = A'_{11}\sin^4\theta + \left(A'_{66} + 2A'_{12}\right)\sin^2\theta\cos^2\theta + A'_{22}\cos^4\theta \tag{1.3.6}$$

The roots of the characteristic equation are related to the elastic compliance by

$$\mu_1\mu_2 = -\sqrt{\frac{A'_{22}}{A'_{11}}} \tag{1.3.7}$$

$$\text{and } \sigma_{\theta} = p\frac{A'_{11}}{A'_{\theta}}\left[\mu_1\mu_2\cos^2\phi + (1+n)\sin^2\phi\right] \tag{1.3.8}$$

If the plate is loaded in a direction parallel to the principal axis of the plate, then $\phi = 0$ and equation (1.3.4) becomes equation (1.3.9).

$$\sigma_{\theta} = p\frac{A'_{11}}{A'_{\theta}}\left[\mu_1\mu_2\cos^2\phi + (1+n)\sin^2\phi\right] \tag{1.3.9}$$

Equation (1.3.4) was used to evaluate the stress distribution for both unidirectional and cross-ply laminates as shown in Fig.1.3.1 and Fig.1.3.2 respectively. From the curves in Fig.1.3.1 it is observed that the maximum stress concentration is obtained where the fibers are aligned with the load direction. As the fiber angle changes, the magnitude of the stress concentration is reduced. Also, the location of the stress concentration varies with the fiber orientation. The results for cross-ply laminates were obtained by varying the loading direction relative to principal axis.

From Fig.1.3.2 it can be observed that as the load direction changes relative to the principal axis, the stress concentration is reduced.

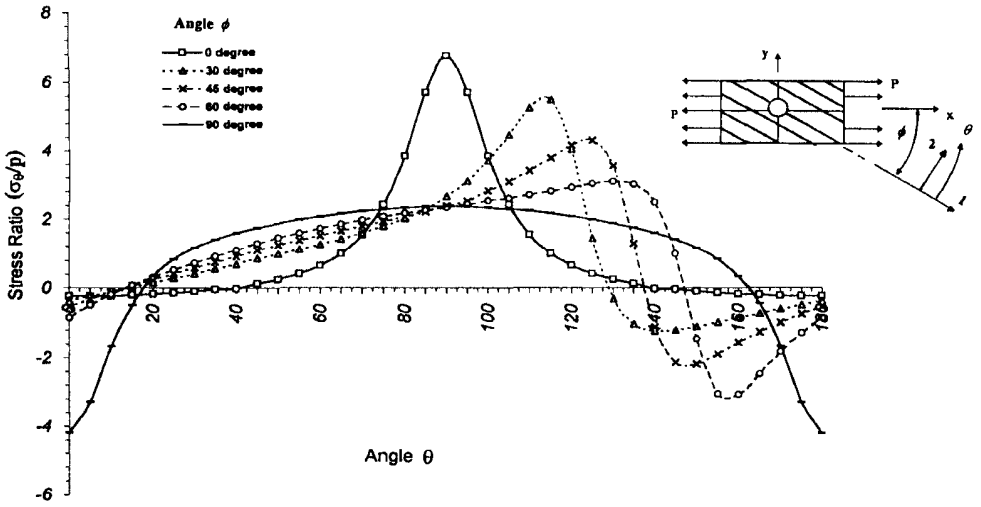

Fig.1.3.1 Effect of fiber orientation on stress concentration in a unidirectional laminate [17].

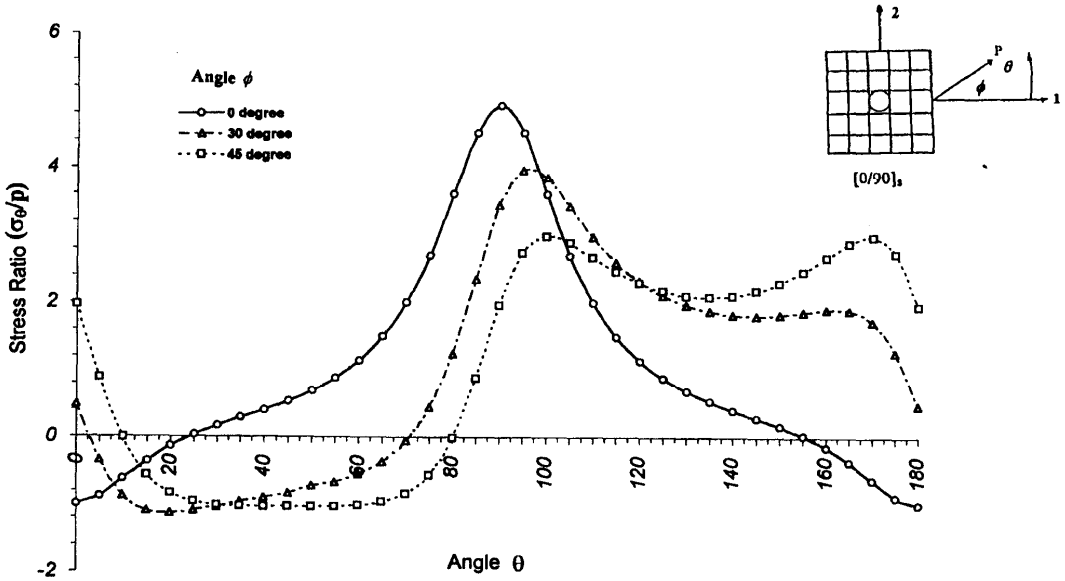

Fig.1.3.2 Effect of loading direction on stress concentration in a cross-ply laminate [17].

The stress distribution for symmetric angle-ply $[\pm\beta]_S$ and the $[0/\pm\beta/90]_S$ laminates was evaluated by equation (1.3.9) which is shown in Fig. 1.3.3 and Fig.1.3.4 respectively. From Fig. 1.3.3 it is observed that unlike unidirectional laminates the location of the maximum stress

concentration for angle ply laminates didn't shift with the ply orientation. In angle ply laminates the maximum value of the stress concentration was observed at a location 90 degrees relative to load axis. From Fig.1.3.1 and Fig.1.3.3 it can be observed that the maximum stress concentration decreases more rapidly for symmetric angle ply laminates than for unidirectional laminates with similar fiber orientation. Thus it can be observed that the angle-ply laminates reduce the maximum stress concentration.

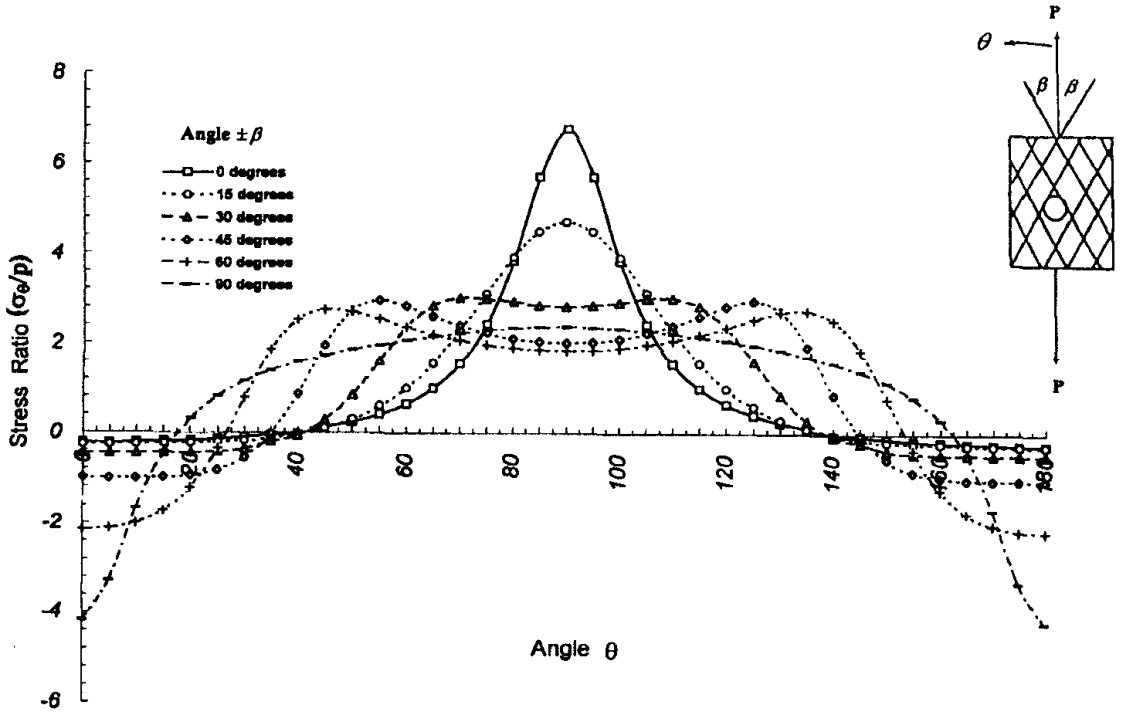

Fig.1.3.3 Effect of ply orientation on stress concentration in angle-ply laminate [17].

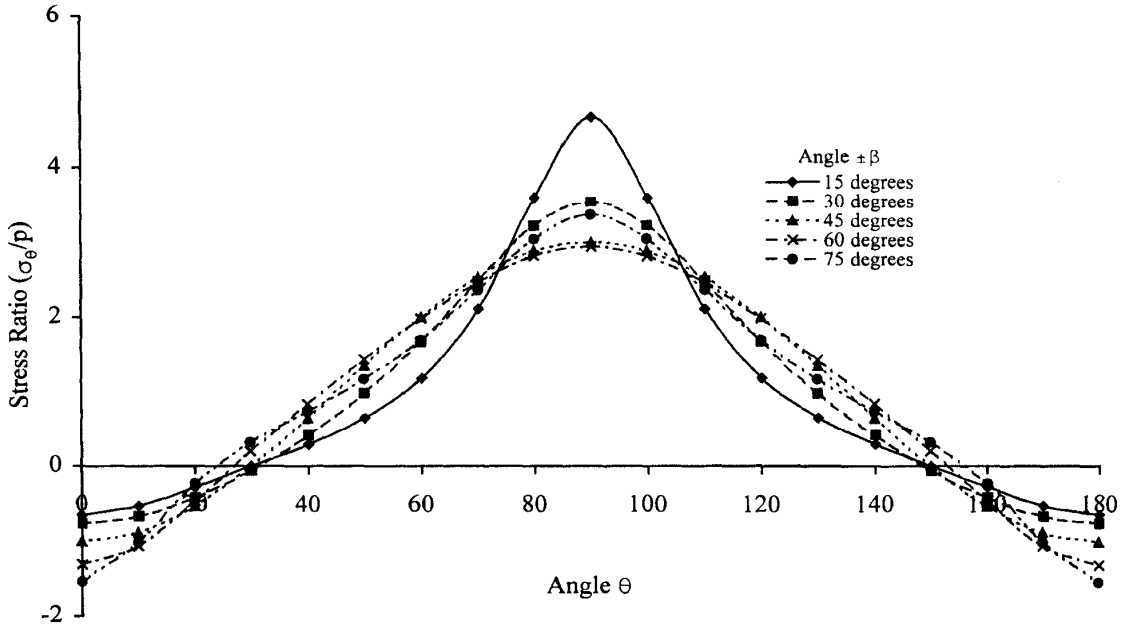

Fig.1.3.4 Effect of fiber orientation of off-axis plies on stress concentration in $[0/\pm\beta/90]_S$ laminates [17].

Fig. 1.3.4 shows that changing orientation of the $\pm\beta$ plies influences the magnitude but not the location of the maximum stress concentration for $[0/\pm\beta/90]_S$ laminates. The Location of the maximum stress concentration in these laminate was observed at 90 degrees to the loading direction. The Stress concentration was found to decrease as plies deviated from the loading direction. However, after approximately $\beta = \pm 60$ degrees, the maximum stress concentration again began to increase. For $[0/\pm\beta/90]_S$ laminates, the off-axis $\pm\beta$ ply orientation within a range of 45 to 60 degrees generated the optimum design to reduce the stress concentration. This motivates the study of non-traditional[1] laminates for reducing the stress concentration and subsequently observing the effect of reduced stress concentration on the laminate strength.

[1] Non-traditional laminates are the ones where β necessarily need not be 45 degrees. 0 and 90 degree can also be altered in such laminates. The name traditional laminates is given to the ones where the lay-up comprises of 0, 90 and 45 degrees.

1.4 Effect of stacking sequence on the strength

Failure in composites can be decomposed into two modes; in-plane failure and out- of- plane failure. The in-plane failure which is the focus of this study is tensile in nature. Out of plane failure is usually referred to as delamination. The aim of this section is to understand the effect of the stacking sequence of plies on these two modes of failure.

1.4.1 Net tension strength

Yan et al. [18] compared the response of notched composite laminates when subjected to open and filled hole tension. The authors considered the effect of ply orientation, lateral constraint and washer size in this study. T800/3900-2 graphite/epoxy prepreg was selected for the study and the laminates were divided into 2 groups. Group 1 comprised of laminates A, B, C and D while Group 2 included laminates E, F, G, H and I.

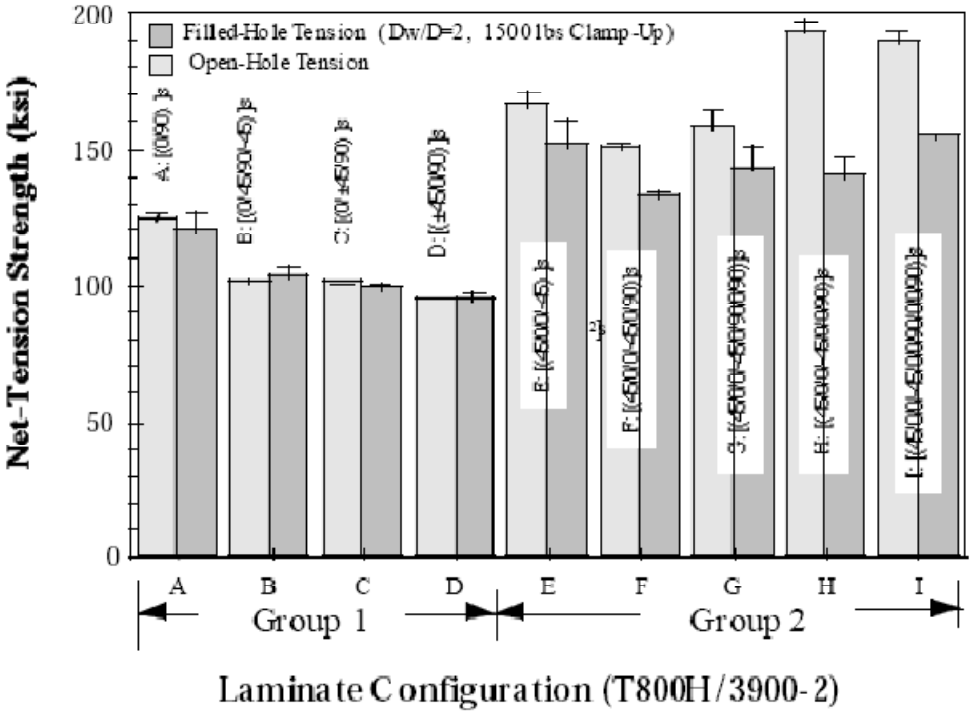

Fig. 1.4.1 Comparison of net-tension strength between open and filled-hole laminates [18]

Fig. 1.4.1 provides a comparison between the 2 groups regarding the open and filled hole tensile strength. The details of the stacking sequence of the two groups are provided in Table 1.4.1.

Table 1.4.1 Stacking sequence of group 1 and group 2[18].

	Laminates	Stacking Sequence
GROUP 1	A	$[0/90]_S$
	B	$[0/45/90/-45]_S$
	C	$[0/\pm 45/90]_S$
	D	$[\pm 45/0/90]_S$
GROUP 2	E	$[45/0/0/-45]_S$
	F	$[45/0/0/-45/0/90]_S$
	G	$[45/0/0/-45/0/90/0/90]_S$
	H	$[45/0/0/-45/0/0/90]_S$
	I	$[45/0/0/-45/0/0/90/0/0/90]_S$

For group 1, no strength reduction was found for filled-hole specimens compared to open hole specimens. For group 2 the notch strength of filled hole laminates was lower than the open-hole laminates. It was observed that the change in stacking sequence in the quasi-isotropic configuration of $[0/\pm 45/90]_S$ had a small effect on the net tensile strength. Radiographic analysis of the two groups led to the conclusion that damage in group 1 was mostly confined near the stress concentration areas and propagated from the hole region toward the free edge. The damage was found to be in form of matrix cracks and fiber breakage. For group 2 additional damage modes like delamination and fiber-matrix splitting were found. Higher strength of group 2 in net tension study is obvious due to presence of higher number of 0^0 plies. However, it seems

that a higher percentage of 0 degree plies also made the laminates of group 2 prone to delamination and fiber-matrix splitting.

1.4.2 Delamination strength.

Delamination in laminated composites is a major cause of strength degradation. Interlaminar stresses generated near free edges are responsible for this mode of failure. Generally multidimensional laminates combining angle-ply and cross ply sub laminates, exhibit effects of both shear coupling and Poisson's ratio mismatch. Thus in the case of multidirectional laminates all three interlaminar stresses ($\sigma_Z, \tau_{XZ}, \tau_{YZ}$) are present and the stacking sequence plays a major role in governing the nature of these stresses. Pipes et al. [18] tested three stacking sequences $[\pm 15/\pm 45]_S$, $[15/\pm 45/-15]_S$ and $[\pm 45/\pm 15]_S$ under a uniaxial tensile load. The distribution of σ_Z through the thickness is shown in Fig. 1.4.2.

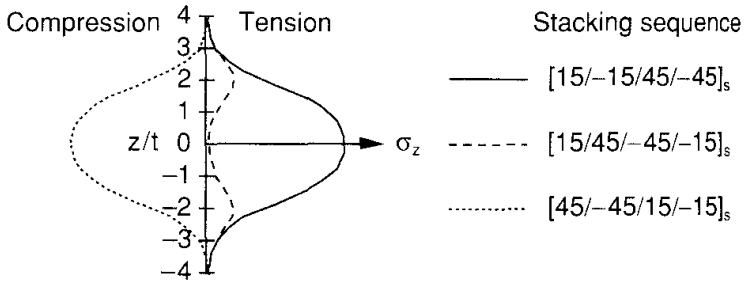

Fig.1.4.2 Effect of stacking sequence on the through thickness distribution of interlaminar stress σ_Z near the free edge [18]

It is evident that both the magnitude and sign of the stress can change drastically with stacking sequence. From a design point of view it seems that stacking sequences that result in minimum σ_Z stresses should be considered. In the case of notched laminates the effect of interlaminar stresses is more detrimental. In this case, edge effects were accentuated by the stress concentration on the edge of the hole. Denial et al. [19] used two boron/epoxy panels of

$\left[0_2/\pm45/\overline{0}\right]_S$ and $\left[\pm45/0_2/\overline{0}\right]_S$ stacking sequence with a circular hole and subjected them to axial tension. The overbar over the 0 degree plies indicates that the laminates are symmetric about the mid plane of the ply. These two stacking sequences resulted in tensile and compressive interlaminar normal stress (σ_z) near the edge of the hole at the point of maximum stress concentration. Fig. 1.4.3 shows the fringe pattern in a photoelastic coating around the hole near failure.

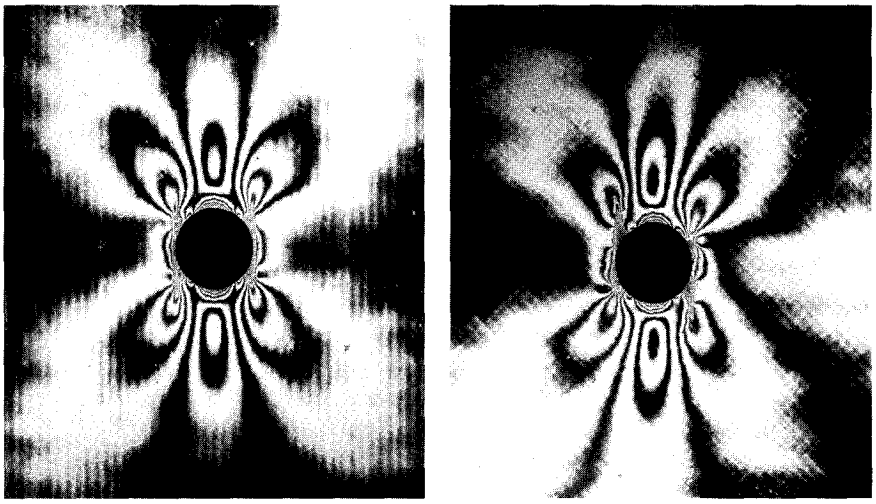

$\left[0_2/\pm45/\overline{0}\right]_S$ $\left[\pm45/0_2/\overline{0}\right]_S$

Fig.1.4.3 Isochromatic fringe patterns in photoelastic coating around the hole in boron/epoxy specimens of two different stacking sequences [19]

The pattern for the $\left[0_2/\pm45/\overline{0}\right]_S$ specimen is fairly symmetric with a lower stress concentration. The pattern for the $\left[\pm45/0_2/\overline{0}\right]_S$ specimen skewed with the higher stress concentration. The failure surface of the two specimens is also very different as is shown in Fig. 1.4.4.

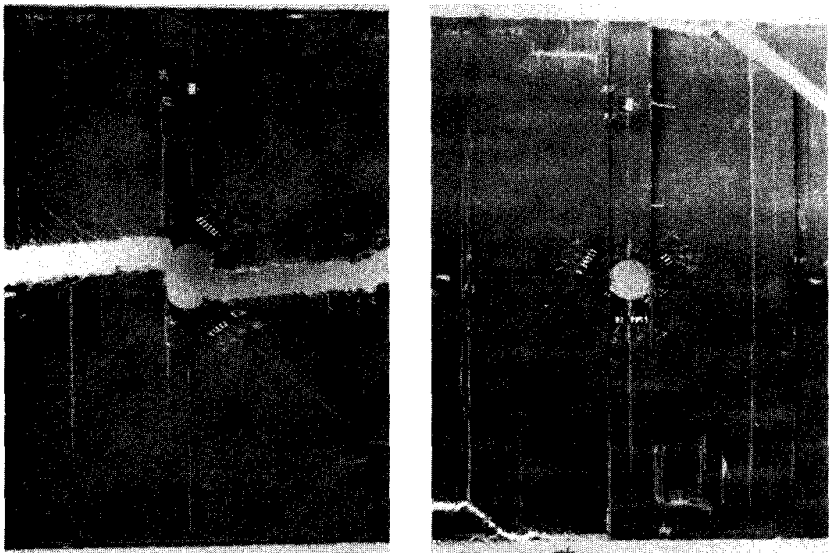

$\left[\pm 45/0_2/\overline{0}\right]_S$ $\left[0_2/\pm 45/\overline{0}\right]_S$

Fig.1.4.4 Failure patterns of boron/epoxy tensile panels with holes of two different stacking sequences [19].

The $\left[\pm 45/0_2/\overline{0}\right]_S$ specimen failed horizontally in catastrophic manner at an average applied axial stress of 61.7 Ksi. The $\left[0_2/\pm 45/\overline{0}\right]_S$ specimen failed by vertical cracking in a non-catastrophic manner at an applied stress of 76.4 Ksi. The specimen then split into two strips that carried a much higher ultimate stress of 105 Ksi.

Park H.J. [20] used finite element analysis to study the effects of stacking sequence and clamping force on delamination bearing strength of mechanical fastened joints in carbon/epoxy composite laminates. 3D contact stress analysis was performed to mimic the bolt-hole interaction. His FEA procedure was based on a layer wise theory along with the Ye-delamination criterion. The problem was studied for $\left[0/90\right]_S$ & $\left[90/0\right]_S$ lay-up. Park found that a stacking sequence of $\left[90/0\right]_S$ was more advantageous than $\left[0/90\right]_S$ from the aspect of delamination

strength. Similar conclusions were obtained by [21, 22, 23] with experimental and finite element analysis. Park [24] also investigated the effect of stacking sequence and clamping force on notched composites using an Acoustic Emission (AE) technique. The effect of stacking sequence on the ultimate and the delamination strength in bolted and pinned joints was compared. The results for both joints were quite similar. The study was based on a stacking sequence of quasi-isotropic lay-ups $[90_3/\pm45_3/0_3]_S$, $[90_3/0_3/\pm45_3]_S$ and $[0_3/\pm45_3/90]_S$. The results indicated that lay-up $[90_3/\pm45_3/0_3]_S$ had the highest bearing strength and the lay-up $[90_3/0_3/\pm45_3]_S$ had the second highest one. The lay-up $[90_3/0_3/\pm45_3]_S$ had the highest delamination strength. Thus the stacking sequence $[90_3/0_3/\pm45_3]_S$ which had the highest delamination strength and second highest ultimate bearing strength should be preferred from the view point of its characteristics of fail-safe delamination failure. The 90 degree layers have been found to play a very important role in the bearing strength of composite laminates. Composite laminates with 90 degree layers on the surface have higher delamination strength than the laminates with 90 degree plies in the center. Kaminski B.E. [25] has reported similar findings using [0/90] glass/epoxy coupons. He found with low scatter that the coupons with 90 degree layers on the surface were 9% stronger than the ones with 0 degree layers on the surface.

1.5 Failure Criteria study

Failure criteria for homogenous isotropic materials, such as the maximum normal stress (Rankine), maximum shear stress (Tresca) and maximum distortional energy (Von Mises) are well established. Macromechanical failure theories for composites have been proposed by extending and adapting isotropic failure theories to account for anisotropy in the stiffness and strength of the composites [3].

Lamina failure theories can be broadly classified into mode based and interactive.

1.5.1. Mode based

Theories such as maximum stress, maximum strain, Hashin-Rothem in which specific failure modes are predicted by comparing individual lamina stress or strains with corresponding strength and ultimate strains are mode based or non-interactive failure theories. The maximum strain theory does allow for some interaction of stress components due to Poisson's effect [3] but is still considered a mode based theory.

Jenkins [26] in 1920 was the first to use an extension of the maximum normal stress theory or Rankine theory for orthotropic laminae. Kelly [27] used the maximum stress theory in 1966 to predict the off axis strength of unidirectional composites as a function of fiber orientation by three different curves corresponding to 3 different failure modes. According to the maximum stress theory, failure occurs when at least one stress component along one of the principal material axes exceeds the corresponding strength in that direction. For a three dimensional state of stress with transverse isotropy on the 2-3 plane the following set of inequalities must be satisfied to avoid failure

$$\begin{aligned} S_{1C} < \sigma_1 < S_{1T} \\ S_{2C} < \sigma_2 < S_{2T} \\ S_{3C} < \sigma_3 < S_{3T} \\ S_{12C} < \sigma_{12} < S_{12T} \\ S_{23C} < \sigma_{23} < S_{23T} \\ S_{13C} < \sigma_{13} < S_{13T} \end{aligned} \quad . \tag{1.5.1}$$

In the above equations S_i (for i = 1, 2, 3) denotes the ultimate value of stress in the principal normal directions and S_{ij} (for ij= 12, 23 and 13) stands for ultimate shear value in the principal shear directions. C and T are used to distinguish between the strength parameters in compression and tension respectively.

In 1967 Waddoups [28] proposed the Maximum Strain Criterion for orthotropic laminae as an extension of the Maximum Normal Strain Theory (or Saint Venant's Theory) for isotropic materials as

$$\begin{aligned} \varepsilon_{1C} < \varepsilon_1 < \varepsilon_{1T} \\ \varepsilon_{2C} < \varepsilon_2 < \varepsilon_{2T} \\ \varepsilon_{3C} < \varepsilon_3 < \varepsilon_{3T} \\ \varepsilon_{12C} < \varepsilon_{12} < \varepsilon_{12T} \\ \varepsilon_{23C} < \varepsilon_{23} < \varepsilon_{23T} \\ \varepsilon_{13C} < \varepsilon_{13} < \varepsilon_{13T} \end{aligned} \tag{1.5.2}$$

Hashin and Rotem found that failure of a lamina under a general in-plane loading can be characterized by two failure criteria, one for fiber failure and the other for inter fiber failure [29] as

$$\left(\frac{\sigma_1}{S_{1T} or S_{1C}} \right) = 1 \tag{1.5.3}$$

$$\left(\frac{\sigma_2}{S_{2T} or S_{2C}} \right)^2 + \left(\frac{\sigma_{12}}{S_{12}} \right)^2 = 1 \tag{1.5.4}$$

These criteria can be extended for a general three-dimensional state of stress in terms of stresses acting on the three principal material planes and related to the expected failure modes on those planes.

$$\left(\frac{\sigma_1}{S_{1T} or S_{1C}} \right) = 1 \tag{1.5.5}$$

$$\left(\frac{\sigma_2}{S_{2T} or S_{2C}} \right)^2 + \left(\frac{\sigma_{23}}{S_{23}} \right)^2 + \left(\frac{\sigma_{12}}{S_{12}} \right)^2 = 1 \tag{1.5.6}$$

$$\left(\frac{\sigma_3}{S_{3T} or S_{3C}} \right)^2 + \left(\frac{\sigma_{23}}{S_{23}} \right)^2 + \left(\frac{\sigma_{13}}{S_{13}} \right)^2 = 1 \tag{1.5.7}$$

The strength parameters used in the equations should be based on the sign of the stresses. That

means if the stress in the longitudinal or 1-direction is tensile (+) then the limiting strength should be tensile and for compressive stress (-) the strength parameter should be compressive. This holds true for transverse and shear stresses[2] as well. In the criteria above, the strength values are the ultimate values when the stress-strain behavior is linear to failure. In case of non-linear behavior, the strength values can be defined as proportional limits of the corresponding stress-strain curves.

Hashin proposed a modification of Hashin-Rotem theory. He proposed more interactive criteria for tensile failure of the fiber and for combined transverse compression and shear. In the latter case he introduced the effect of transverse shear strength in the criterion.

1.5.2 Quadratic Failure Theories

The quadratic failure criteria are interactive and based on curve fitting considerations and not on physical failure modes [30]. The stress terms are included in one expression and failure is predicted without reference to particular failure mode.

The deviatoric and distortional energy has been proposed by many investigators (e.g. Von Mises, Hencky, Nadai) in various forms as a failure criterion for isotropic ductile metals. For a two-dimensional state of stress in the principal stress directions, the von Mises yield criterion has the following form [3]

$$\left(\sigma_1\right)^2+\left(\sigma_2\right)^2-\sigma_1\sigma_2=\left(\sigma_{yp}\right)^2 \tag{1.5.8}$$

Hill modified this criterion for case of ductile metals with anisotropy and proposed the following form.

$$A\sigma_1^{\,2}+B\sigma_2^{\,2}+C\sigma_1\sigma_2+D\sigma_{12}^{\,2}=1 \tag{1.5.9}$$

[2] For in-plane and out of plane shear stress the sign of limiting stress is immaterial as the value of shear in tension and compression is same. Also for the current work $S_{12}= S_{23}= S_{13}$.

where A, B, C, D are material parameters characteristic of the current state of anisotropy. The modified form of the criterion led to Tsai-Hill criterion which in three dimensional form can be written as [31]

$$\begin{aligned}
&\left(\frac{\sigma_1}{S_{1T}orS_{1C}}\right)^2+\left(\frac{\sigma_2}{S_{2T}orS_{2C}}\right)^2+\left(\frac{\sigma_3}{S_{3T}orS_{3C}}\right)^2\\
&-\left(\frac{1}{(S_{1T})^2 or(S_{1C})^2}+\frac{1}{(S_{2T})^2 or(S_{2C})^2}-\frac{1}{(S_{3T})^2 or(S_{3C})^2}\right)\sigma_1\sigma_2\\
&-\left(\frac{1}{(S_{2T})^2 or(S_{2C})^2}+\frac{1}{(S_{3T})^2 or(S_{3C})^2}-\frac{1}{(S_{3T})^2 or(S_{3C})^2}\right)\sigma_2\sigma_3\\
&-\left(\frac{1}{(S_{3T})^2 or(S_{3C})^2}+\frac{1}{(S_{1T})^2 or(S_{1C})^2}-\frac{1}{(S_{2T})^2 or(S_{2C})^2}\right)\sigma_3\sigma_1\\
&+\left(\frac{\sigma_{12}}{S_{12}}\right)^2+\left(\frac{\sigma_{23}}{S_{23}}\right)^2+\left(\frac{\sigma_{13}}{S_{13}}\right)^2\geq 1
\end{aligned} \qquad (1.5.10)$$

Failure is predicted by this theory when the left side of the equation is greater than or equal to one. The theory is similar to Hashin-Rotem theory in the sense that it also takes into account the sign of the stresses in the principal material direction. However unlike Hashin-Rotem theory it fails to provide information regarding the mode of failure. The quadratic nature of the theory has been criticized because it is based on Hill's theory, which is suitable for homogenous, anisotropic and ductile metals, whereas most composites are strongly heterogeneous and brittle. One more problem with the Hill's theory is that it predicts that failure will never occur in hydrostatic state of stress ($\sigma_1= \sigma_2= \sigma_3$, $\sigma_{12}= \sigma_{23}= \sigma_{13}=0$). Due to shear coupling in composites, however, a hydrostatic state of stress can produce shear strains and failure. Hoffman's equation due to its linear terms, could predict failure for a hydrostatic state of stress. The three dimensional form of the Hoffman equation is given as.

$$\frac{1}{2}\left(\frac{1}{S_{1T}S_{1C}}+\frac{1}{S_{2T}S_{2C}}-\frac{1}{S_{3T}S_{3C}}\right)\left(\sigma_1-\sigma_2\right)^2+\frac{1}{2}\left(\frac{1}{S_{2T}S_{2C}}+\frac{1}{S_{3T}S_{3C}}-\frac{1}{S_{1T}S_{1C}}\right)\left(\sigma_2-\sigma_3\right)^2$$
$$\frac{1}{2}\left(\frac{1}{S_{3T}S_{3C}}+\frac{1}{S_{1T}S_{1C}}-\frac{1}{S_{2T}S_{2C}}\right)\left(\sigma_3-\sigma_1\right)^2+\left(\frac{1}{S_{1T}}-\frac{1}{S_{1C}}\right)\sigma_1+\left(\frac{1}{S_{2T}}-\frac{1}{S_{2C}}\right)\sigma_2 \qquad (1.5.11)$$
$$\left(\frac{1}{S_{3T}}-\frac{1}{S_{3C}}\right)\sigma_3+\left(\frac{\sigma_{12}}{S_{12}}\right)^2+\left(\frac{\sigma_{23}}{S_{23}}\right)^2+\left(\frac{\sigma_{13}}{S_{13}}\right)^2\geq 1$$

However, all of the quadratic theories form special case of a more general quadratic interaction criterion. In 1971 Tsai and Wu [32] proposed an improved and simplified version of a tensor polynomial failure theory for anisotropic materials originally proposed by Gol'denblat and Kopnov [33]. The proposed criterion in contracted notation can be written as

$$F_i\sigma_i+F_{ij}\sigma_i\sigma_j=1 \qquad (1.5.12)$$

where contracted notation i, j = 1, 2, ….. , 6. F_i and F_{ij} are experimentally determined strength tensors of second and forth rank, respectively. In order to avoid failure, the left hand side of the equation (1.5.12) should be less than one. The details of finding the coefficients of the stress terms are in [34]. The three dimensional form of the Tsai-Wu criterion which is used for current work is given as

$$\left(\frac{1}{S_{1T}}-\frac{1}{S_{1C}}\right)\sigma_1+\left(\frac{1}{S_{2T}}-\frac{1}{S_{2C}}\right)\sigma_2+\left(\frac{1}{S_{3T}}-\frac{1}{S_{3C}}\right)\sigma_3+\frac{{\sigma_1}^2}{S_{1T}S_{1C}}+\frac{{\sigma_2}^2}{S_{2T}S_{2C}}+\frac{{\sigma_3}^2}{S_{3T}S_{3C}}$$
$$-\frac{\sigma_1\sigma_2}{2\sqrt{S_{1T}S_{1C}S_{2T}S_{2C}}}-\frac{\sigma_2\sigma_3}{2\sqrt{S_{2T}S_{2C}S_{3T}S_{3C}}}-\frac{\sigma_1\sigma_3}{2\sqrt{S_{1T}S_{1C}S_{3T}S_{3C}}} \qquad (1.5.13)$$
$$+\left(\frac{\sigma_{12}}{S_{12}}\right)^2+\left(\frac{\sigma_{23}}{S_{23}}\right)^2+\left(\frac{\sigma_{13}}{S_{13}}\right)^2\geq 1$$

Farsakh et al. [35] proposed an energy based failure criterion for non-linear composite materials which was included as a part of the current work. The three dimensional form of the criterion in contracted notation can be written as

$$\sum \tilde{U}_i = \left(\frac{U_i}{U_{im}}\right) + \left(\frac{U_{ij}}{U_{ijm}}\right) = 1 \qquad (1.5.14)$$

Where *i, j* = 1, 2, 3 and U_i , U_{ij} correspond to extensional and shear strain energy densities respectively. According to the energy criterion, failure can be avoided if the left hand of equation 1.5.14 is less than 1. The strain energy densities can be found as

$$U_i = \frac{1}{2}\sigma_i \varepsilon_i$$
$$U_{ij} = \frac{1}{2}\sigma_{ij} \varepsilon_{ij} \quad . \qquad (1.5.15)$$

The subscript *m* denotes the corresponding maximum value of strain energy density. The stress and strain terms in equation (1.5.15) can be replaced with the maximum strength and strain values for finding values of denominators of equation (1.5.14).

1.6 Applicability of Laminate Failure Theories

The validity and applicability of any failure theory depends on its agreement with experimental results. Recently two main efforts were aimed at evaluation of laminate failure theories. One of them was by Sun [36, 37] and the other by Hinton et al. [38].

Sun [36, 37] reviewed six failure theories and compared theoretical predictions of the laminate strength with experimental results for six composite materials and various loading conditions. He found that for fiber dominated laminates the maximum strain, maximum stress and Hashin-Rotem gave the best predictions. The interactive theories gave good predictions for matrix dominated strength. Hinton et al. [38] conducted a World Wide Failure Exercise (WWFE) over a twelve year period for the purpose of assessing the predictive capabilities of some of the most prominent failure theories of composite materials. The exercise covered nineteen theories, four composite material systems, six laminate configurations and four loading conditions. The leading theories (Tsai, Puck, Zinoviev, Bogetti, Cuntze) were compared. One observation of this exercise

was that even for unidirectional lamina, predictions of these theories differed by up to 200-300% from each other. The authors also found that these theories tended to underperform in situations where shear and matrix behavior plays a significant role in the failure process and where large deformations were present before final failure occurred in the experiment.

One of the findings of the literature concerning failure criteria was that the theories that perform well for a certain set of material properties and under given loading condition may not do well if these variables are changed. This makes the task of generalizing the applicability of failure theories extremely difficult. The best practice is to compare the theoretical predictions with accurate and reliable experimental results. In the current work the strength predictions of seven prominent failure theories were compared with experimental data to check their accuracy in predicting the First Ply Failure strength for notched composite laminates under tensile loading condition.

1.7 FEA Study

A study of some of the established FEA methodologies was carried out to compare their advantages and disadvantages which would assist in the selection of a method most suitable for the current work. Tay et al. [39] presented a new FEA based approach known as the element failure method (EFM) which they claimed to be better than the traditional material property degradation method (MPDM) and the fracture mechanics approach. In the MPDM, the value of certain material properties in the constitutive relation is reduced when damage or failure is determined e.g. if failure is determined to have occurred in the fiber direction (as in the breaking of fibers in tension), the fiber direction Young's modulus (E_{11}) may be set to zero. This is a special case of MPDM and is called the Ply Discount Method. Normally in the published literature the authors set the degraded material properties to a small percentage of the original. This is done to avoid the stiffness matrix of the FEA model from becoming ill-conditioned which

is turn stops the FEA code from converging. MPDM has another major drawback. There is uncertainty regarding the property that should be degraded e.g. if transverse cracking or failure is predicted in a composite it is not clear if only the transverse Young's Modulus E_{22} or both this and the in-plane Shear Modulus G_{12} should be reduced. Additionally, the effect of damage on the Poisson's Ratio ν_{12} and ν_{21} is not obvious or easily determined.

Fracture mechanics has been applied to composites although some have cited some major drawbacks in the traditional approach. First of all in composites it is not easy to clearly identify and define cracks and crack tips as is done with metals. In some exceptional situations a crack may be defined such as in the case of a single delamination in a laboratory fracture test specimen. However, even in such situations, mechanisms such as fiber bridging across crack surfaces, delamination kinking, or branching into other fracture planes greatly complicates the analysis and can lead to wrong results.

The EFM modifies nodal forces to reflect changes in the stress bearing capability of the damaged material. The stiffness matrix remains untouched and drawbacks of MPDM are automatically avoided. The EFM along with the Strain Invariant Failure Theory (SIFT) have been recently proposed by Gosse [40]. An in house 2D FE code was used to implement the methodology. A three point bend test was used as test problem for damage prediction. EFM based approach was very attractive for predicting damage in composites. However the drawback of using EFM based approach for this thesis was the complexity to successfully incorporate it in commercially available software like ANSYS^{TM}, which was used for the numerical work of this study.

Wang et al. [41] used both; linear elastic and a progressive damage approach to predict the strength of un-notched and notched quasi-isotropic laminates. AS4/3501-6 material was used and laminates were subjected to tension and compression tests. It was found that the linear elastic approach underestimated the First Ply Failure strength (FPF) or overestimated the Last Ply

Failure (LPF) strength for un-notched laminates. The progressive damage was able to predict the un-notched strength, provided that the non-linear shear behavior was accounted for and the appropriate failure criterion was used. They used ABACUS FEA software and shell elements to implement material degradation. For the purpose of comparison, a characteristic distance approach was applied to the open-hole strength problem. In this approach the authors had to calibrate the model for tension and compression loading and for a particular hole size. Although they found that no consistent relationship existed between the characteristic distance and the hole size for the tension case, the compression characteristic distance was related to the hole diameter by the following relation

$$d_0 = 0.843 + 0.0606 * d \tag{1.7.1}$$

where d_0 was the characteristic distance and d was the hole diameter.

The predicted accuracy of the tensile test appeared satisfactory with a maximum discrepancy of 2%. However, the prediction of the compression test was less accurate with a maximum error of 15%. Thus this approach does not appear to be very robust.

1.8 Conclusion

The literature review pointed to the fact that stress concentration in composites with a circular hole is a function of the fiber angles. For traditional laminates $[0/\pm\beta/90]_S$ the off axis orientation $\pm\beta$ has been found to generate an optimum design for reducing stress concentration where $45 \le \beta \le 60$. Further, the effect of stacking sequence on the failure modes in laminates is quite evident. For multidirectional laminates which show shear coupling and Poisson's mismatch, interlaminar stresses are present and thus a particular stacking sequence can be generated for resisting delamination growth. Seven failure theories (Max-Strain, Max-Stress, Hashin-Rothem, Tsai-Wu, Tsai-Hill, Hoffman and energy) were presented and would be applied

along with an appropriate FE method. Although some have proposed damage based FE models for strength prediction of laminated composites, but for the current study a linear elastic approach was chosen in order to determine the first ply failure (FPF).

.

2. 3D FEA MODEL

2.1 Introduction

The literature review behind the current study provided a motivation to find the effect of tailoring fiber orientation and stacking sequence on the open-hole tension (OHT) strength of the laminates. This chapter aimed at introducing a 3D FE model that could show the through thickness strain field and the sensitivity of stress concentrations to the fiber orientation and stacking sequence of a laminated composite. A standard quasi-isotropic lay-up $\left[\left(45/90/-45/0\right)_2\right]_S$ was used as baseline and compared with other non-traditional lay-ups.

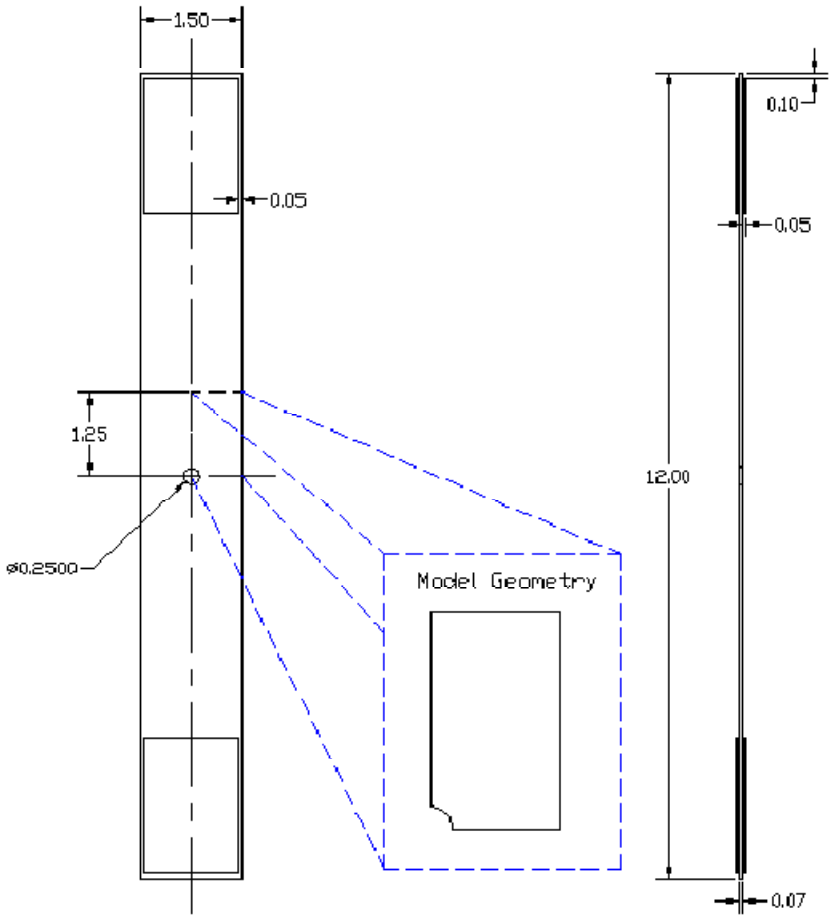

Fig. 2.2.1 Geometry of the laminated plate along with the model geometry

2.2. Laminate Geometry

The laminate geometry under consideration is shown in the Fig.2.2.1. The composite plate was 12 inches in height, 1.5 inches in width and 0.07 inches in thickness with a 0.25 inch hole drilled in the center. The effect of the stress concentration due to the presence of circular notches diminishes at a distance of 9 radii from the edge of the hole [42]. Keeping this in mind, the height of the FE model was restricted to 1.25 inches i.e. ten times the radii of the hole. The model geometry shown in Fig. 2.2.1 is one eighth of the original plate.

2.3 Material Properties

The properties of T600:125-33 carbon/epoxy material were found using in-plane tests of five specimens of $[0]_6$, $[90]_{16}$ and $\left[\left(\pm 45\right)_3\right]_s$ laminates. The 0 and 90 degree coupons were used to determine the in-plane ultimate tensile strength in longitudinal and transverse direction respectively. Due to a linear relationship between stress and strain in unidirectional (i.e. 0 and 90 degree) laminates, the ultimate stress and strain is equivalent to the yield stress and strain. However, the in-plane shear behavior is non-linear. For the non-linear shear behavior, the yield strength should be used in order to determine the First Ply Failure of a laminate [3]. To determine this yield point, two methodologies were considered. One is the double notch shear test and other is the cyclic loading and unloading of ± 45 degree coupons. The double notch shear test was found unsuitable for finding in-plane shear properties as described in detail in section 2.6. The uniaxial loading of a ± 45 degree coupon can be used to find out the in-plane shear stress and shear strain. Using the stress transformation relation [34] and referring to Fig. 1.2.1 we get

$$\begin{bmatrix} \sigma_1 \\ \sigma_2 \\ \tau_{12} \end{bmatrix} = \left[T_{2D}\right] \begin{bmatrix} \sigma_x \\ \sigma_y \\ \tau_{xy} \end{bmatrix} \tag{2.3.1}$$

where T_{2D} is a two dimensional transformation matrix given by

$$[T_{2D}] = \begin{bmatrix} \cos^2(\theta) & \sin^2(\theta) & 2\cos(\theta)\sin(\theta) \\ \sin^2(\theta) & \cos^2(\theta) & -2\cos(\theta)\sin(\theta) \\ -\cos(\theta)\sin(\theta) & \cos(\theta)\sin(\theta) & \cos^2(\theta)-\sin^2(\theta) \end{bmatrix} . \qquad (2.3.2)$$

For uniaxial loading condition ($\sigma_y = \tau_{xy} = 0$) of $\left[\left(\pm 45\right)_3\right]_s$ laminate,

$$\tau_{12} = \frac{\sigma_x}{2} \qquad (2.3.3)$$

Using the transformation relation for strain we get

$$\begin{bmatrix} \varepsilon_1 \\ \varepsilon_2 \\ \gamma_{12}/2 \end{bmatrix} = [T_{2D}] \begin{bmatrix} \varepsilon_x \\ \varepsilon_y \\ \gamma_{xy}/2 \end{bmatrix}, \qquad (2.3.4)$$

and solving for shear strain in the principal material direction we obtain

$$\gamma_{12} = -\varepsilon_x + \varepsilon_y . \qquad (2.3.5)$$

The stress-strain curve obtained by the repeated loading and un-loading of $\left[\left(\pm 45\right)_3\right]_s$ is shown in Fig.2.3.1. The ± 45 degree coupons were loaded in steps, starting from 3651 Psi to 14604 Psi. The material yielded well within a tensile stress of 14604 Psi. Hence, further increase in load was not necessary. At the end of each load step, the test was stopped and the load was allowed to drop to the initial value (approx. 3-4 lbs). The load was held at this stage and one of the grips holding the coupons was relaxed. The spike marked by O in Fig.2.3.1 indicates this sudden release of grip. This relaxation in the load allowed for viscoelastic strain recovery. This is

marked by V in Fig. 2.3.1. The time dependent recovery strain is shown in appendix A-1. Unlike metals, the 0.2% strain rule may provide misleading results for polymers. Few steps were followed to come up with a yield stress and corresponding yield strain suitable for this study. Firstly, damage induced in the material due to each loading cycle was found by plotting the recovered viscoelastic shear strain after each stress cycle with the shear stress. One of the recovered shear strain points is denoted as V_P in Fig. 2.3.1. Ten such points could be extracted from Fig.2.3.1 and were plotted with respect to their corresponding shear stress values. This is shown in Fig.2.3.2.

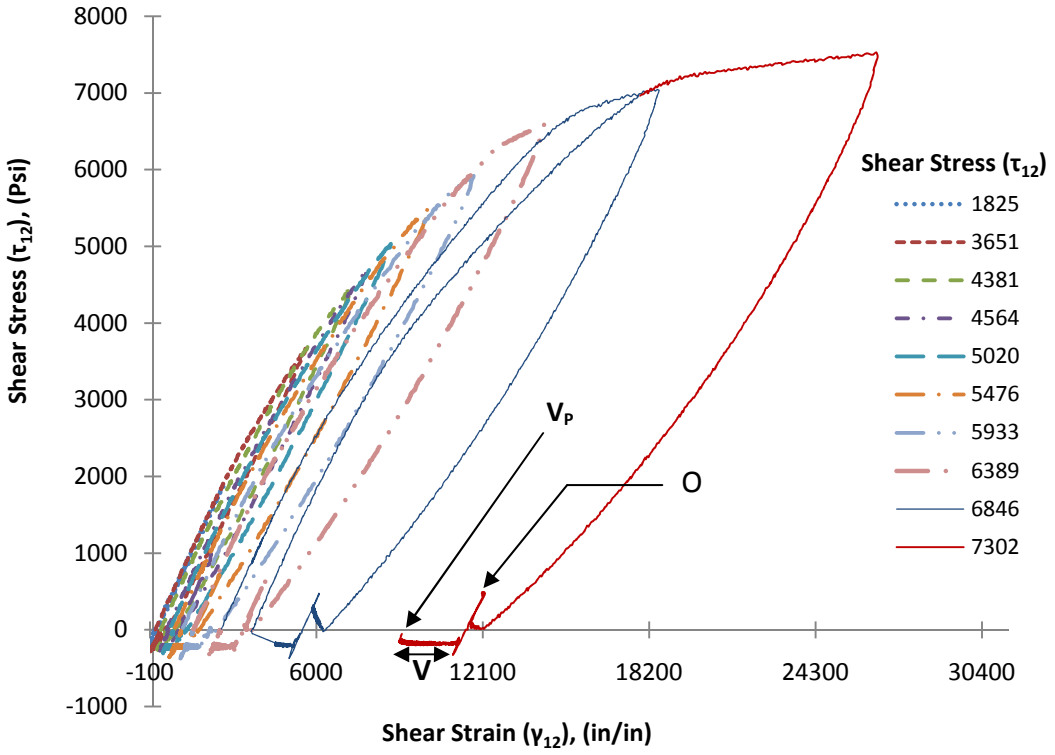

Fig.2.3.1 Shear Stress Vs Shear Strain curve for cyclic loading and unloading of $\left[(\pm 45)_3\right]_s$ laminate.

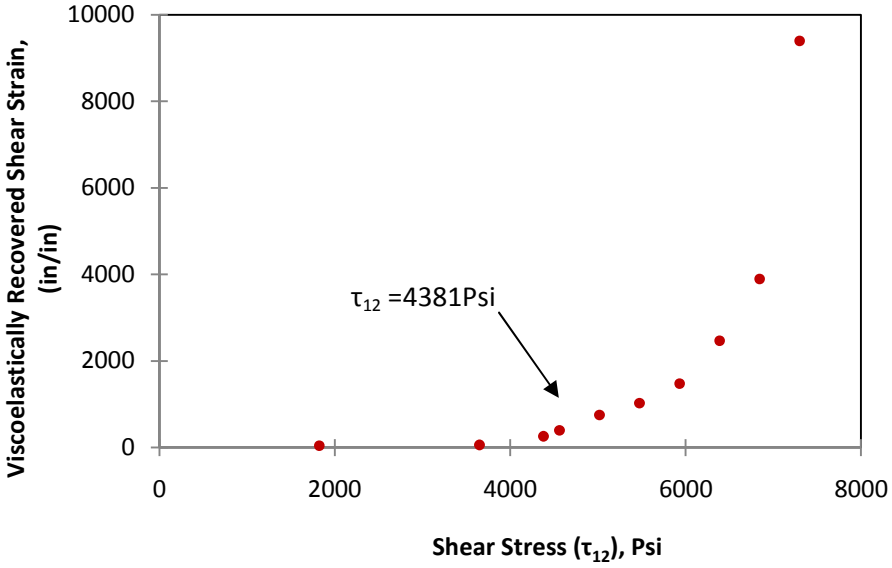

Fig.2.3.2 Viscoelastically recovered Shear Strain Vs Shear Stress

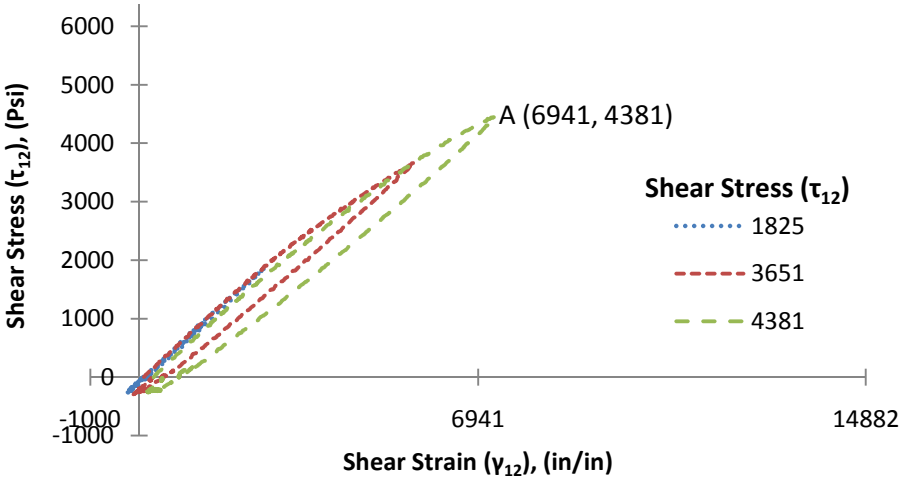

Fig.2.3.3 Shear Stress Vs Shear Strain for defining Yield Stress

From Fig. 2.3.2 it can be seen that up till the shear stress of 4381 Psi, the strain recovered completely. However, during the third repetitive load cycle there was some damage in the material. Thus the maximum shear stress corresponding to the third repetitive loading cycle can be assumed as the yield shear stress in the material. It is denoted by the Y axis value of point A in Fig. 2.3.3. Fig. 2.3.3 is same as Fig. 2.3.1 except that it shows only the first three stress cycles. The X axis value of point A in Fig. 2.3.3 denotes the yield shear strain of the composite material.

The properties from the in-plane tests and from Fig.2.3.3 were used to define the tensile orthotropic behavior of each lamina. From [55] we could assume that $S_{13} = S_{23}$. Further, this assumption didn't affect the results as during FEA it was observed that out of plane stresses were smaller (10 times) as compared to in-plane stresses. The compression properties were obtained from [43].

Table 2.3.1 Material Properties of T600:125-33 carbon/epoxy.[3]

$E_1 = 19.73\times10^6$	$E_2 = 1.38\times10^6$	$E_3 = E_2$
$G_{12} = 0.81\times10^6$	$G_{13} = G_{12}$	$G_{23} = \dfrac{E_2}{2(1+\upsilon_{23})}$
$\upsilon_{12} = 0.298$	$\upsilon_{23} = 0.35$	$\upsilon_{13} = \upsilon_{12}$
$S_{1T} = 332.8\times10^3$	$S_{2T} = 6.28\times10^3$	$S_{3C} = S_{2C}\ S_{3T} = S_{2T}$
$S_{1C} = 209\times10^3$	$S_{2C} = 33\times10^3$, $S_{3C} = S_{2C}$	$S_{12} = 4.381\times10^3, S_{13} = S_{23} = S_{12}$

2.4 Model Formulation

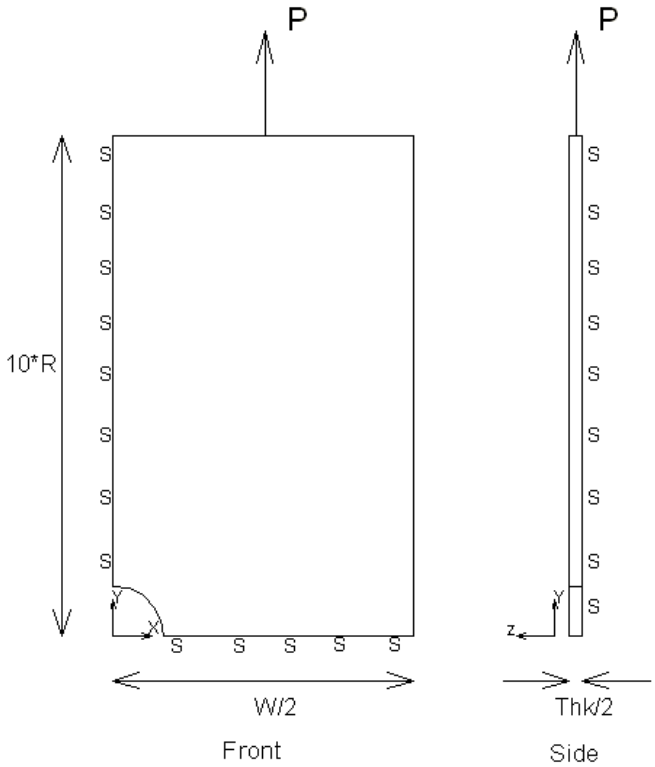

Fig. 2.4.1 Geometry used for the FEA study.

[3] Modulus and strength properties are in Psi.

The numerical simulation was carried out using the ANSYS^{TM} 10.0 FEA package. A static tensile pressure P was applied on the top face of the model in the Y direction as shown in Fig. 2.4.1. The model geometry used 3 symmetric boundary conditions (BCs) on three mutually perpendicular planes. The front view in Fig.2.4.1 shows symmetric B.C. applied to the faces resting on the X-Z and the Y-Z reference plane. Thus the new width was half the original width of the plate i.e. W/2. The height was reduced to 10×R, R being the radius of the hole. The reason for choosing this height has been explained in section 2.2. Since the laminates were symmetric through the thickness, so the model thickness was reduced to half i.e. Thk/2. Thus, effectively, one-eighth section of the actual plate was used for the FEA.

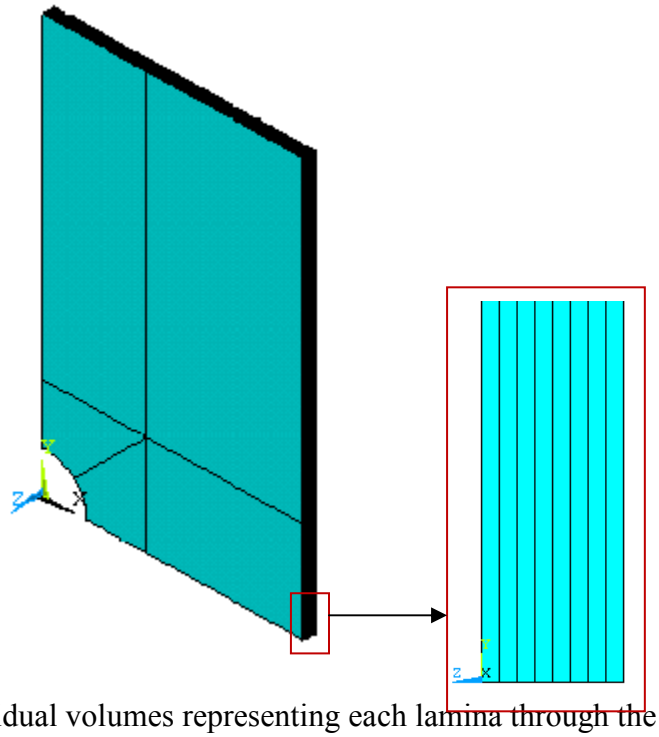

Fig. 2.4.2 Individual volumes representing each lamina through the thickness

A one eighth model meant that only 8 plies needed to be created instead of 16 as shown in Fig. 2.4.2. Each of the plies in the laminate geometry was represented by a single volume layer. The ANSYS^{TM} material model interface allows the stiffness matrix input to represent each lamina. The coefficients of the stiffness matrix are a function of fiber orientation. Since the model

geometry was in the global coordinate system (C.S.), represented by the X-Y-Z reference frame, the stiffness matrix for each lamina was transformed from the principal material to the global C.S. by the following relations [3].

$$[\sigma]_{1,2,3} = [T_{3D}][\sigma]_{x,y,z} \tag{2.4.1}$$

Or

$$[\sigma]_{x,y,z} = [T_{3D}]^{-1}[\sigma]_{1,2,3}, \tag{2.4.2}$$

where $[\sigma]_{x,y,z}$ and $[\sigma]_{1,2,3}$ are the contracted 3D stress matrices in the global (X, Y, Z) and the principal material (1, 2, 3) C.S. respectively. $[T_{3D}]$ represents the three dimensional form of the coordinate transformation matrix given by

$$[T_{3D}] = \begin{bmatrix} \cos^2(\theta) & \sin^2(\theta) & 0 & 0 & 0 & 2\cos(\theta)\sin(\theta) \\ \sin^2(\theta) & \cos^2(\theta) & 0 & 0 & 0 & -2\cos(\theta)\sin(\theta) \\ 0 & 0 & 1 & 0 & 0 & 0 \\ 0 & 0 & 0 & \cos(\theta) & -\sin(\theta) & 0 \\ 0 & 0 & 0 & \sin(\theta) & \cos(\theta) & 0 \\ -\cos(\theta)\sin(\theta) & \cos(\theta)\sin(\theta) & 0 & 0 & 0 & \cos^2(\theta) - \sin^2(\theta) \end{bmatrix} \tag{2.4.3}$$

From Hooke's law

$$[\sigma]_{1,2,3} = [Q]_{1,2,3}[\varepsilon]_{1,2,3}, \tag{2.4.4}$$

where $[Q]_{1,2,3}$ is the contracted form of 3D stiffness matrix in the principal material C.S. and can be expressed in terms of the material properties of Table 2.3.1 as

$$[Q]_{1,2,3} = \begin{bmatrix} \frac{1}{E_1} & \frac{-\upsilon_{12}}{E_1} & \frac{-\upsilon_{13}}{E_1} & 0 & 0 & 0 \\ \frac{-\upsilon_{12}}{E_1} & \frac{1}{E_2} & \frac{-\upsilon_{23}}{E_2} & 0 & 0 & 0 \\ \frac{-\upsilon_{13}}{E_1} & \frac{-\upsilon_{23}}{E_2} & \frac{1}{E_3} & 0 & 0 & 0 \\ 0 & 0 & 0 & \frac{1}{2G_{23}} & 0 & 0 \\ 0 & 0 & 0 & 0 & \frac{1}{2G_{31}} & 0 \\ 0 & 0 & 0 & 0 & 0 & \frac{1}{2G_{12}} \end{bmatrix}^{-1} . \quad (2.4.5)$$

By substituting the value of $[\sigma]_{1,2,3}$ from equation (2.4.4) into equation (2.4.2), we get

$$[\sigma]_{x,y,z} = [T_{3D}]^{-1}[Q]_{1,2,3}[\varepsilon]_{1,2,3} \quad (2.4.6)$$

and replacing $[\varepsilon]_{1,2,3}$ by $[T_{3D}][\varepsilon]_{x,y,z}$ we obtain

$$[\sigma]_{x,y,z} = [T_{3D}]^{-1}[Q]_{1,2,3}[T_{3D}][\varepsilon]_{x,y,z} \quad (2.4.7)$$

Equation (2.4.7) can also be written as

$$[\sigma]_{x,y,z} = [Q]_{x,y,z}[\varepsilon]_{x,y,z}, \quad (2.4.8)$$

$$\text{where } [Q]_{x,y,z} = [T_{3D}]^{-1}[Q]_{1,2,3}[T_{3D}] \quad (2.4.9)$$

$[Q]_{x,y,z}$ was used as stiffness matrix in the FE model. Solid 64 brick element was used for this work. The element shown in Fig. 2.4.3 is defined by eight nodes having 3 degrees of freedom (D.O.F) at each node in the form of translations in the nodal x, y, z direction. The element has large deflection capabilities. The element coordinate system was set parallel to the global xyz

coordinates using the setting ***Keyopt (1)=0*** as shown in the Appendix-A2. Then using equation (2.4.9) the orientation of the elements in each lamina was defined.

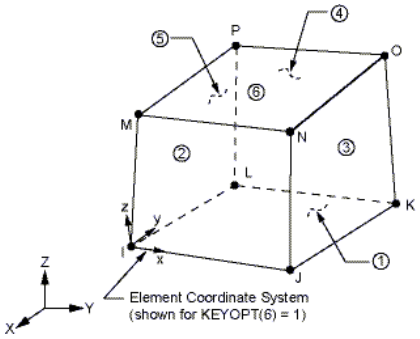

Fig.2.4.3. Solid 64 element used for the FE model

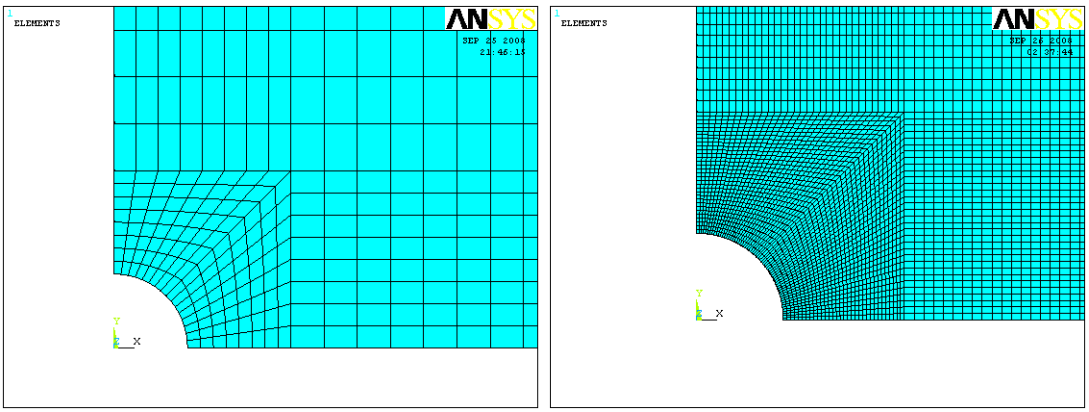

(a) (b)

Fig. 2.4.4 (a) Preliminary mesh of Baseline laminate with 3072 elements **(b)** Refined mesh of Baseline laminate with 55296 elements

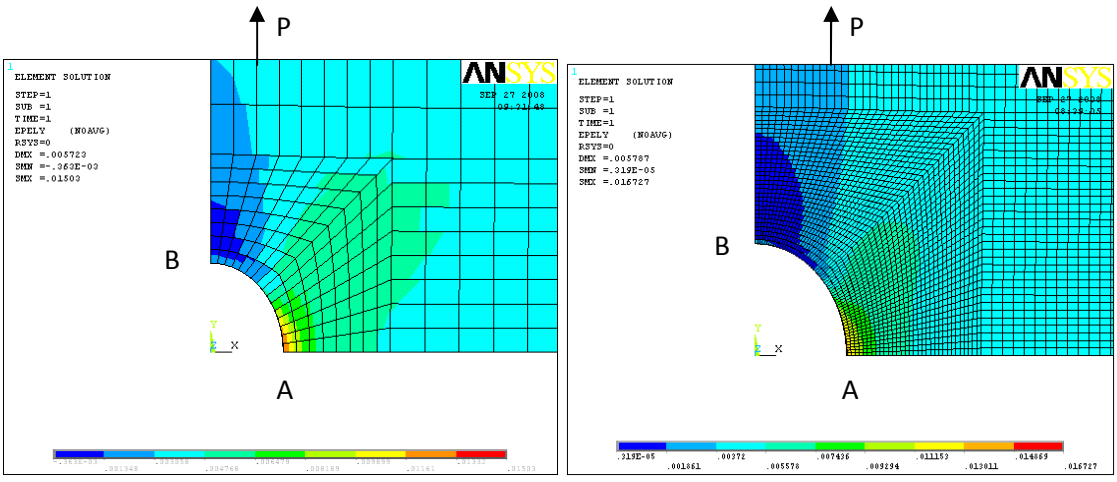

Fig. 2.4.5 Comparison of longitudinal direction (y) strain contours for meshes (a) and (b) of Fig. 2.4.4. Stress P is acting along y direction.

The mesh refinement of the model was carried out in two stages. In the first stage, elements were increased in the XY plane of the laminate. The preliminary mesh as shown in Fig. 2.4.4 (a) had only 3072 elements. Progressive refinement was carried out until convergence was achieved and the final mesh had 55296 elements. The convergence study was carried out at two points, A and B on the surface of the laminate as shown in Fig. 2.4.5. A static tensile stress of 30,000 Psi was applied throughout the convergence study. Longitudinal direction strain (ε_y) was used for checking convergence.

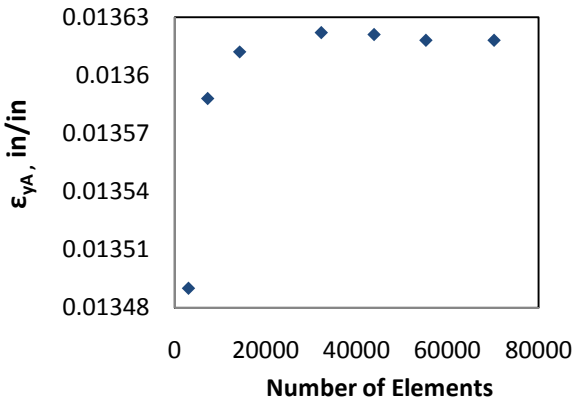

Fig.2.4.6 Variation of longitudinal direction strain at point A (ε_{yA}) with increase in number of elements

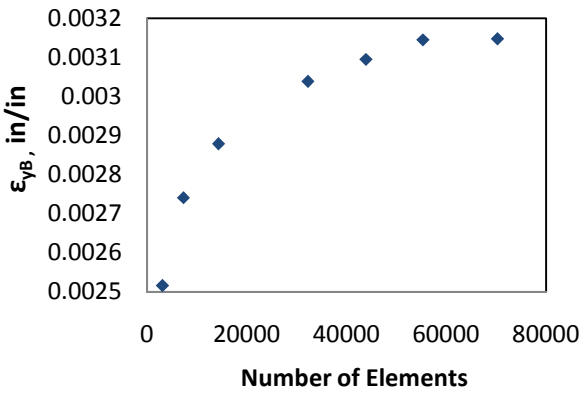

Fig.2.4.7 Variation of longitudinal direction strain at point B (ε_{yB}) with increase in number of elements

Fig. 2.4.6 and Fig. 2.4.7 show the variation in the longitudinal direction strain (ε_y) at point A and B respectively with mesh refinement. After 55296 elements, further refinement didn't seem to have any effect on the strain values.

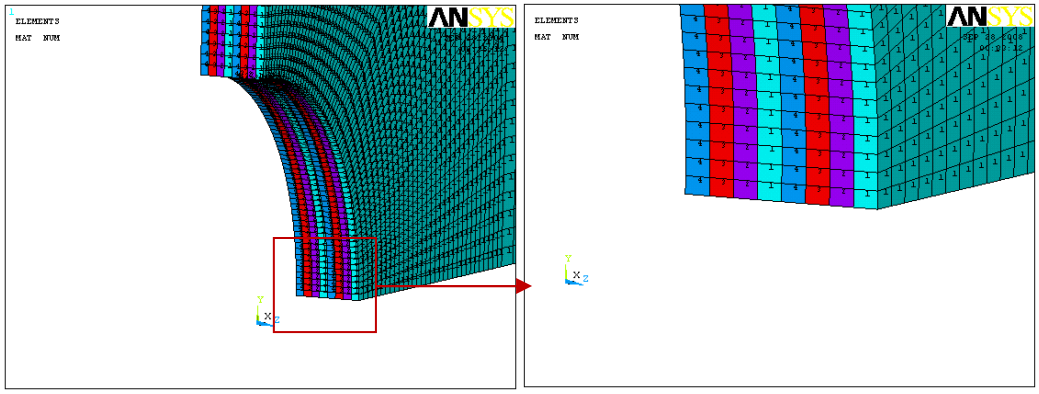

(a)

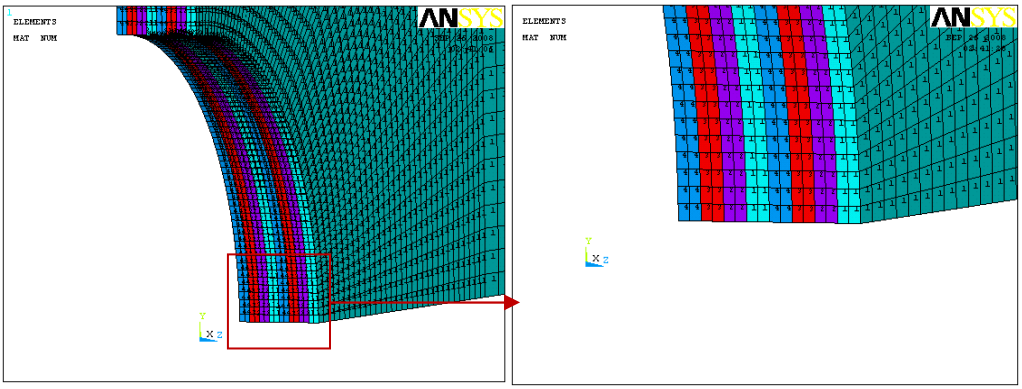

(b)

Fig.2.4.8. (a) Through thickness mesh with one element per ply. **(b)** Mesh with two elements per ply.

In the next stage, elements through the thickness were refined. Instead of one element per ply (Fig.2.4.8 (a)), two elements per ply were used (Fig.2.4.8 (b)). The result of increasing the elements in thickness direction is evident from Fig.2.4.9 (a) and Fig.2.4.9 (b), with 2 elements per ply mesh giving a better strain contour. The term "better" is qualitative in nature. Strain contours with a two elements per ply mesh were much smoother and thus meant reduced error estimation. Further refinement with 3 elements per ply was not possible as the aspect ratio[4] of the elements was too large and so no mesh was generated. The final refinement thus comprised of 110592 elements.

[4] Aspect ratio of an element in FE model is the ratio of the longest and the shortest side of the element. Typically this ratio should be between 2 to 4.

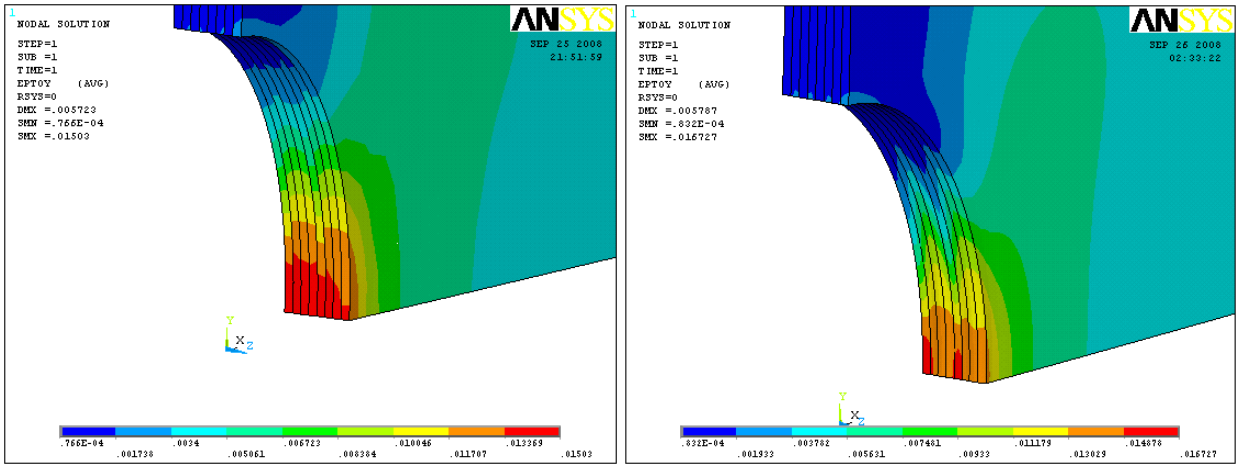

(a) (b)

Fig.2.4.9 (a) Longitudinal direction strain contour of Baseline laminate for mesh with one element per ply **(b)** Longitudinal direction strain contour of Baseline laminate for mesh with 2 elements per ply.

2.5 Model Validation.

The material properties of Aluminum 7075 from Table 2.5.1 were used in the 3D FE model. The strain concentration factors (K_t) from the FEA study were compared with the analytical results [43] for different hole diameter (d) to width (w) ratios.

Table 2.5.1 Material properties of Aluminum 7075 [43]

$E = 10.3 \times 10^6$ Psi	$\upsilon = 0.33$	$G = \dfrac{E}{2(1+\upsilon)}$

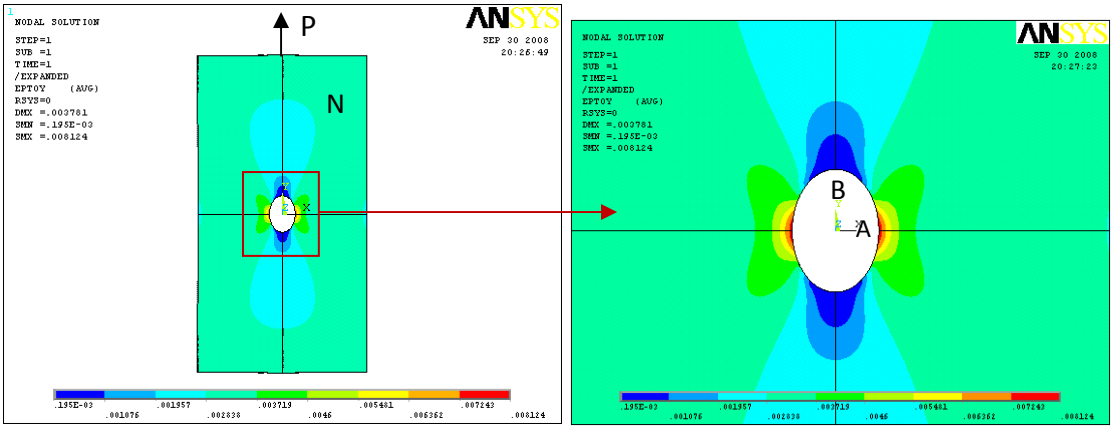

Fig.2.5.1 Longitudinal direction strain (ε_y) contour of 3D model having Aluminum 7075 properties

Fig.2.5.1 shows the contours of the longitudinal direction strain, when the 3D model with isotropic properties from Table 2.5.1 was subjected to a tensile stress (P) of 30,000 Psi. This corresponded to a load of 3150 lbs over an area of 0.105 square inches. The edge of the hole marked as A experienced a maximum longitudinal strain of 0.008124 while B had a minimum value of 0.000195. The symbol N is an approximate nominal strain location.

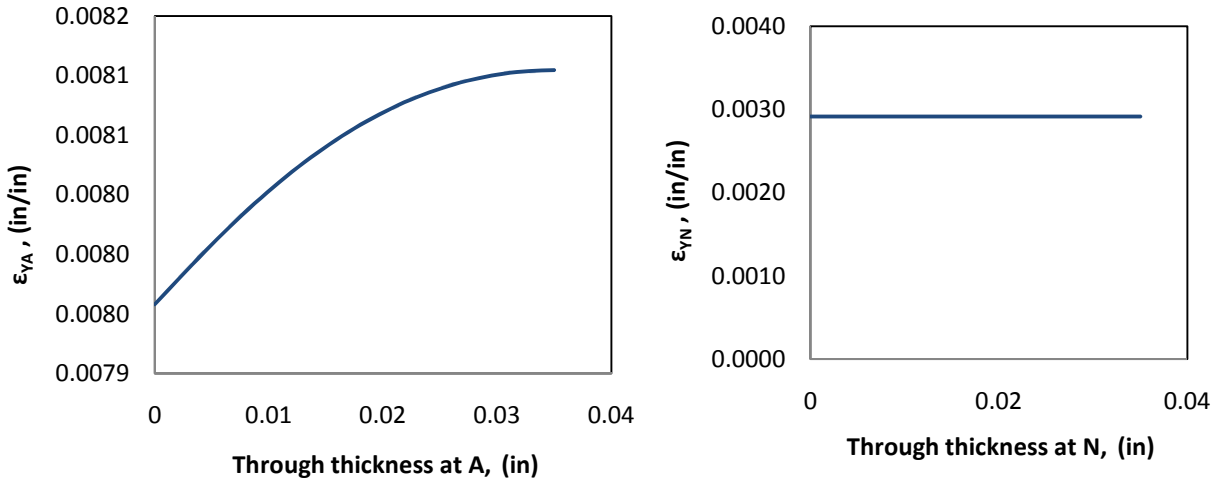

(a) (b)

Fig. 2.5.2 (a) Through the thickness variation of longitudinal direction strain at location A (ε_{YA}). **(b)** Through the thickness variation of longitudinal direction strain at location N (ε_{YN}).

Fig.2.5.2 (a) and (b) show the variation in the longitudinal direction strain through the thickness of the model at locations A and N respectively. Since the model is symmetric through the thickness so the results have been plotted for half the thickness i.e. 0.035 inch. From Fig.2.5.2 (a) we concluded that although the strain change through the thickness of the hole was small but unlike Fig.2.5.2 (b) it was not constant.

Theoretically, the stress concentration factor can be defined as

$$K_t = \frac{\sigma_{\max}}{\sigma_{nom}} \qquad (2.5.1)$$

where $\sigma_{\max}$ is the stress near the point of highest stress concentration. In the Fig. 2.5.1 this point is represented by A. σ_{nom} is to the nominal value of the stress and corresponds to the value of the stress in a plate without hole. Theoretically, nominal stress can be obtained as

$$\sigma_{nom} = \frac{P}{A_{net}} \tag{2.5.2}$$

and $$A_{net} = A_{gross} - A_{hole} \tag{2.5.3}$$

However, there is no way to get the stress or strain for the net area directly in Ansys. In Ansys the nominal stress is

$$\sigma_{FEA,nom} = \frac{P}{A_{gross}} \tag{2.5.4}$$

For this study $\sigma_{FEA,nom}$ is selected from the region marked N in Fig.2.5.1. This region approximately describes the stress state that is unaffected by the presence of hole. However, after applying correction factor K_t can be found as

$$k_t = \frac{\sigma_{\max}}{\sigma_{FEA,nom}} \frac{A_{net}}{A_{gross}} = \frac{\varepsilon_{\max}}{\varepsilon_{FEA}} \frac{A_{net}}{A_{gross}} \tag{2.5.5}$$

For a 2D model, equation 2.5.5 can be applied to find the k_t. However, from Fig.2.5.2 (a) it is evident that for a 3D model the strain through the thickness is not constant and an average of strain should be taken for finding maximum strain ($\varepsilon_{\max}$). Fig. 2.5.3 shows the variation of longitudinal and transverse direction strains through the thickness of baseline laminate when subjected to a tensile stress of 17040 Ksi (24% baseline UTS). It supports the argument of using average strain through the thickness of the laminate near the point A (Fig. 2.5.1). From both Fig. 2.5.2 (b) and Fig. 2.5.3 it is observed that the nominal strain values from the FEA models remain almost constant throughout the thickness. But it is still advised to use the average of all the strain

values through the thickness near the region where nominal strain values are assumed (point N in Fig. 2.5.1). Point B, which also lies on the hole experiences minimum strain concentration.

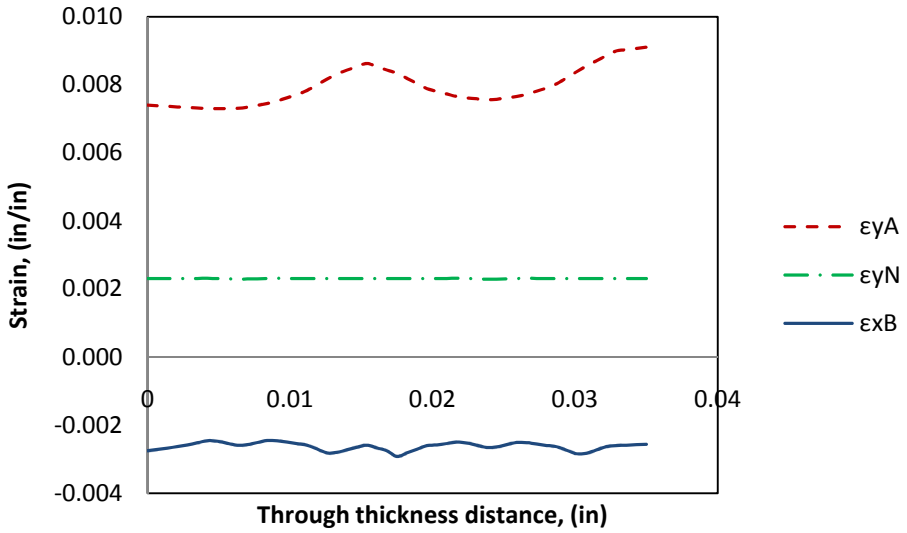

Fig. 2.5.3 Variation of longitudinal and transverse direction strain of baseline laminate through the thickness

Thus the strain concentration factor (K_t) for the 3D model can be defined as

$$K_t = \frac{\varepsilon_{avg.\max}}{\varepsilon_{avg.nom}} \frac{A_{net}}{A_{gross}} \tag{2.5.6}$$

which can be further simplified as

$$K_t = \frac{\varepsilon_{avg.\max}}{\varepsilon_{avg.nom}} \frac{(W-d)}{W} \tag{2.5.7}$$

where $\varepsilon_{avg.\max}$ and $\varepsilon_{avg.nom}$ are the average of the longitudinal direction strain values through the thickness of laminate at locations A and N (Fig. 2.5.1) respectively. W and d are the width of the plate and the diameter of the hole respectively.

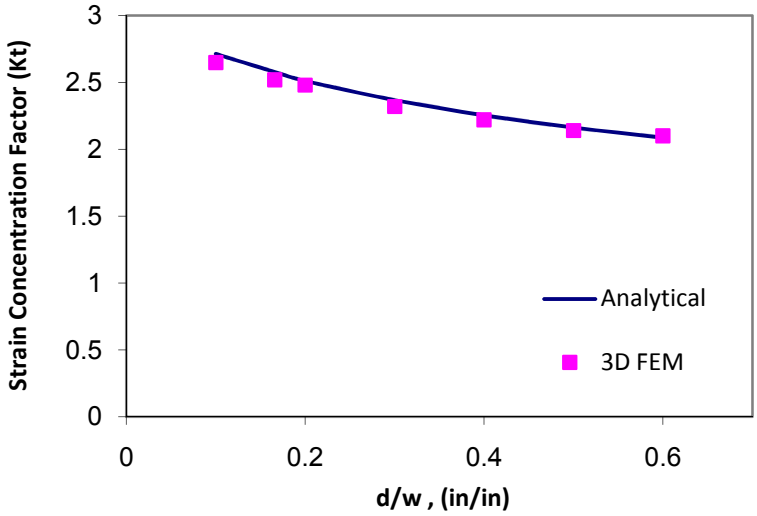

Fig. 2.5.4 Strain concentration factor Vs hole diameter to width (d/w) ratio for Aluminum 7075.

From Fig.2.5.4 it is clear that the strain concentration values from the 3D model closely follow those of the text book for isotropic material properties [43]. Another way of validating the 3D model is by comparing it with analytical solutions. Arjyal et al. [44] derived an expression for longitudinal direction stress (σ_y) as a function of distance from the edge of the hole along x direction. The stress distribution is given as

$$\sigma_y(x) = \left[P + \frac{P}{\beta_1 + \beta_2} \left[\frac{(\beta_1)^2}{1-\beta_1} \left[1 - \frac{\beta_1 x}{\sqrt{r^2 + (\beta_1)^2 (x^2 - r^2)}} \right] - \frac{(\beta_2)^2}{1-\beta_2} \left[1 - \frac{\beta_2 x}{\sqrt{r^2 + (\beta_2)^2 (x^2 - r^2)}} \right] \right] \right] FWC \quad (2.5.8)$$

$$\text{where } \beta_1 = \sqrt{\frac{\beta_0 - \alpha_0}{2}} + \sqrt{\frac{\beta_0 + \alpha_0}{2}} \quad (2.5.9)$$

$$\beta_2 = -\sqrt{\frac{\beta_0 - \alpha_0}{2}} + \sqrt{\frac{\beta_0 + \alpha_0}{2}} \quad (2.5.10)$$

$$\alpha_0 = \sqrt{\frac{E_x}{E_y}} \quad (2.5.11)$$

$$\beta_0 = \frac{E_x}{2G_{xy}} - \upsilon_{xy} \tag{2.5.12}$$

$E_x, E_y, \upsilon_{xy}, G_{xy}$ are obtained from classical lamination plate theory. In equation (2.5.8) the term FWC or finite width correction factor is a scale factor used to multiply the infinite plate solution for a notched plate to obtain the corresponding finite width plate solution. Tan [45] derived an expression for FWC applicable to the orthotropic plate solution

$$FWC = \left\{ 1 - \left(\frac{2r}{W}\right)^4 + \left(\frac{2r}{W}\right)^6 \left(K_T^{\infty} - 3\right) \frac{\left[1 - \left(\frac{2r}{W}\right)^2\right]}{2} \right\}^{-1}, \tag{2.5.13}$$

where r and W are the radius of the hole and the width of the plate respectively.

$$\text{and} \quad K_T^{\infty} = 1 + \frac{1}{\mu}\sqrt{\frac{2}{A_{66}}\left(\sqrt{A_{11}A_{22}} - A_{12} + \frac{A_{11}A_{22} - A_{12}^2}{2A_{66}}\right)}, \tag{2.5.14}$$

where K_T^{∞} is the stress concentration at the opening edge on the axis normal to the applied load for an infinite plate. A_{ij} for $i, j = 1, 2, 6$ are the effective laminate in-plane stiffnesses with 1 and 2 parallel and transverse to the loading direction, respectively. μ is defined as the ratio of the small axis over the large axis of an elliptical hole and therefore $\mu = 1$ for a circular hole. The stress distribution from equation (2.5.8) can be easily converted into a strain distribution by

$$\varepsilon_y = \frac{\sigma_y}{E_y} \tag{2.5.15}$$

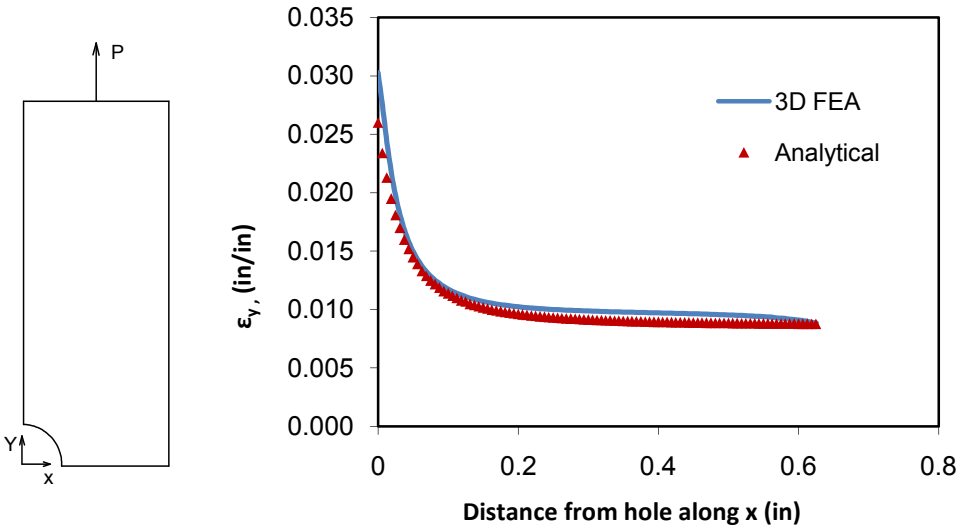

Fig.2.5.5 Comparison of longitudinal direction strain distribution between 3D FE model and analytical solution for stress state around the hole for baseline laminate

Fig.2.5.5 shows the comparison between the longitudinal direction strain distribution of the 3D FE and analytical model along the X direction. The Baseline lay-up of $\left[\left(45/90/-45/0\right)_2\right]_s$ was subjected to a tensile load of 7000 lbs for this comparison. The comparison between the 3D and analytical model indicated that the linear elastic model had the ability to accurately predict the strain profile in the vicinity of the hole.

2.6 Double notch shear test

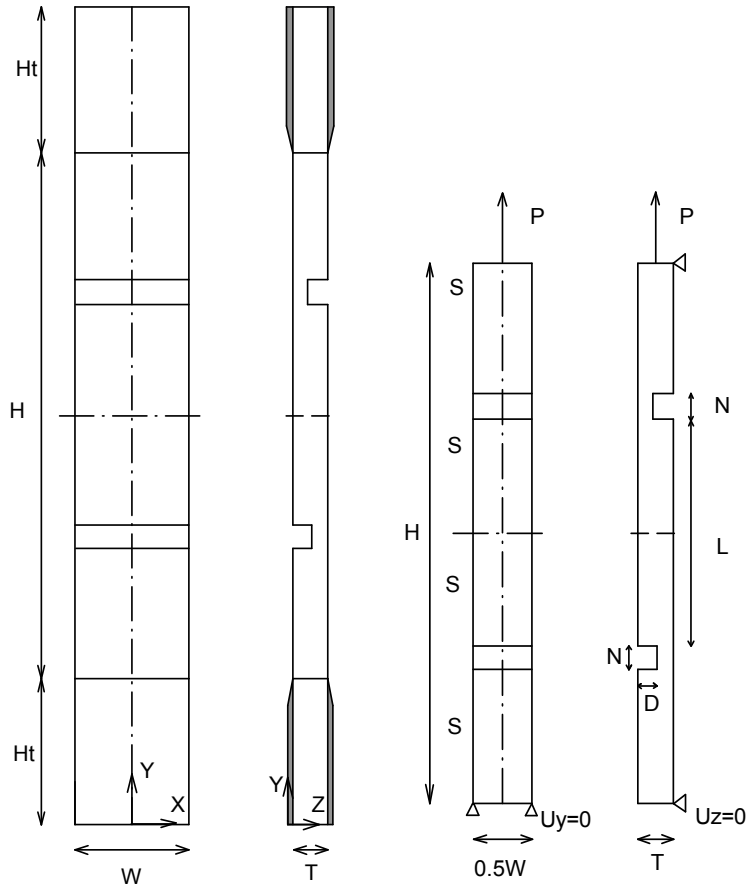

(a) (b)

Fig.2.6.1 (a) Geometry of double notch coupon **(b)** FE model geometry of double notch coupon

Validation of the 3D FE model encouraged its use to determine the feasibility of a double notch shear test for estimating the in-plane yield strength of T600:125-33 material. The Double notch shear test was originally devised to find the interlaminar shear strength. However, for most cases the shears stress in principal material directions is assumed to be identical i.e. $\tau_{12} = \tau_{13} = \tau_{23}$. The laminate fabricated for this test comprised of 38 zero degree laminae with the fiber axis aligned with y direction (Fig. 2.6.1). The specimen as shown in Fig. 2.6.1 (a) was 7.5 inches in height (H+ $2H_t$), 0.996 inches in width (W) and 0.1715 inches in thickness (T). H_t denotes the part of the coupon covered with tabbing. This portion of the coupon is held by the grips of the MTS

tensile test machine. Two grooves ran parallel to each other throughout the width of the sample. The notches were 0.089 inches in depth (D) and 0.16 inches in width (N). The gauge length (L) between the two notches was 0.55 inches. D and T are related by

$$D > T/2 \tag{2.6.1}$$

Equation (2.6.1) ensured that the gauge region remained under pure shear effect when the coupon was subjected to a tensile load.

The FE model geometry is shown in Fig. 2.6.1 (b). Owing to symmetry along the YZ plane, only half width of the sample was modeled. The height of the FE model geometry was restricted to 4.07 inches which is denoted by H in Fig. 2.6.1 (a).

The other boundary conditions used for restricting the rigid body motion and to simulate the effect of grips are given by

$$U_y = 0 \begin{Bmatrix} x = 0, y = 0, z = T/2 \\ x = 0.5W, y = 0, z = T/2 \end{Bmatrix} \tag{2.6.2}$$

$$U_z = 0 \begin{Bmatrix} x = 0, y = 0, z = T \\ x = 0, y = H, z = T \end{Bmatrix} \tag{2.6.3}$$

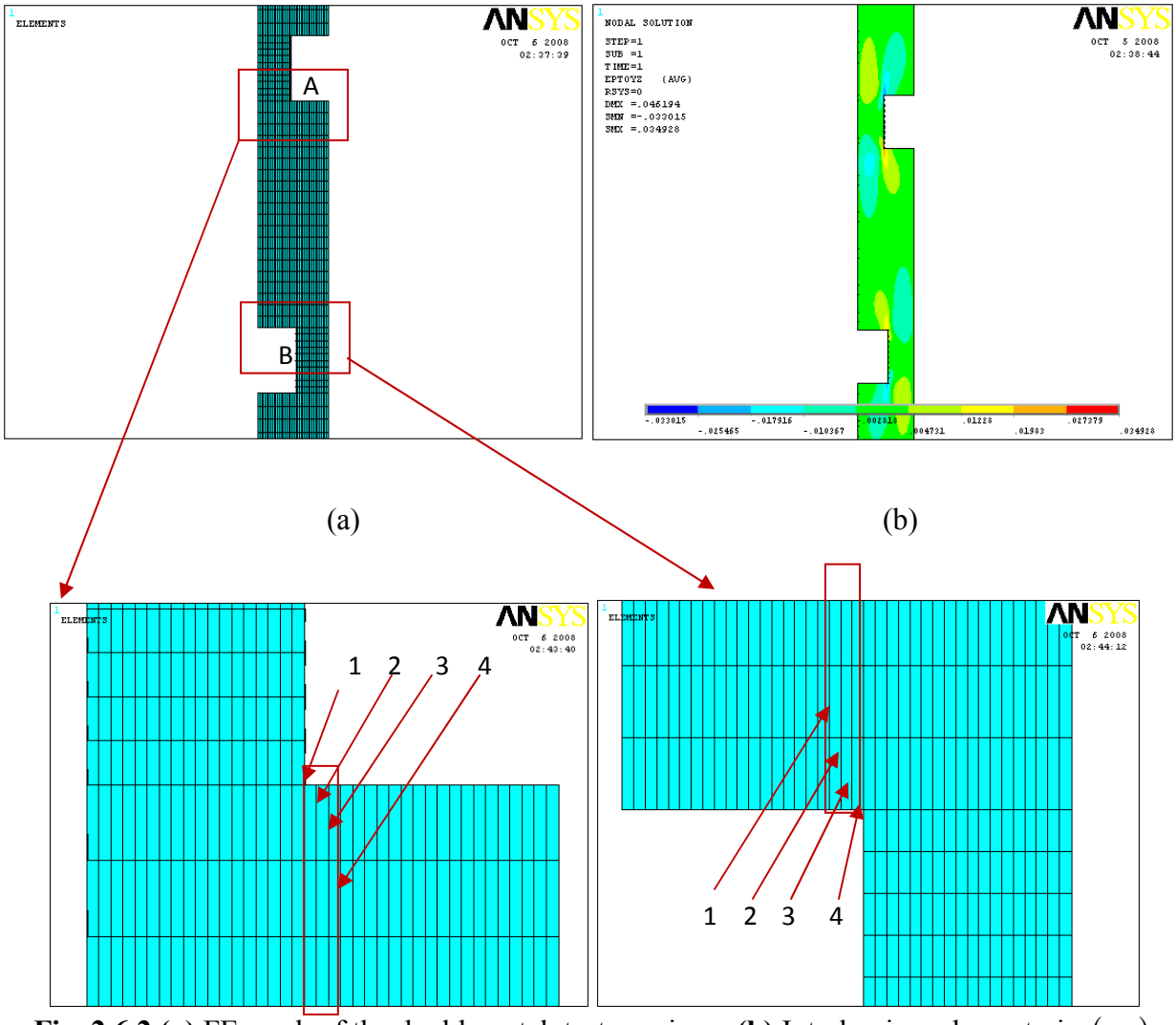

Fig. 2.6.2 (a) FE mesh of the double notch test specimen **(b)** Interlaminar shear strain (ε_{13}) contours of the double notch test specimen.

The model was subjected to a static tensile stress (P) of 30000 Psi as shown in Fig. 2.6.1 (b). Fig. 2.6.2 (a) shows the mesh of the FE model geometry. The two arrows point to the zoomed in image of the A and B regions. As per equation (2.6.1) the depth (D) of the 2 notches exceeded the line of symmetry by 0.00325 inches through the thickness creating a gauge region. The FE model divided this gauge region into 3 laminae. That meant that shear could occur along four paths depending where the shear strain was maximum. These four paths have been numbered as 1, 2, 3 and 4 in the zoomed in image in Fig. 2.6.2 (a). Fig. 2.6.2 (b) shows the contours of the interlaminar shear strain (ε_{13}) in the gauge area. Fig. 2.6.3 shows the change in the interlaminar

shear strain (ε_{13}) along the nodes on the four paths. The nodes that formed these four paths were located on the surface of the gauge area. Although there is a small decrease in strain values from path 1 to path 4 but the general trend is same. The strain field in the gauge area is non-uniform with a relatively high strain concentration at the two notch ends.

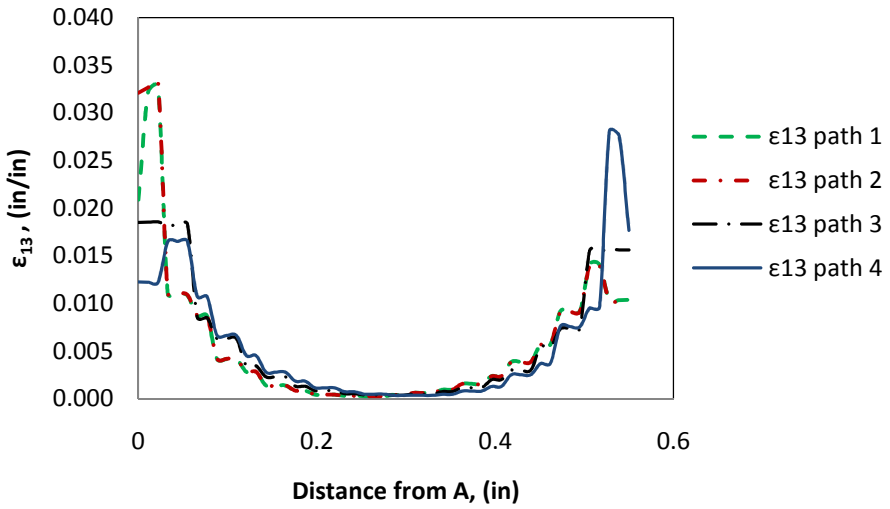

Fig.2.6.3 Variation of interlaminar shear strain (ε_{13}) along the gauge length (L) from A to B

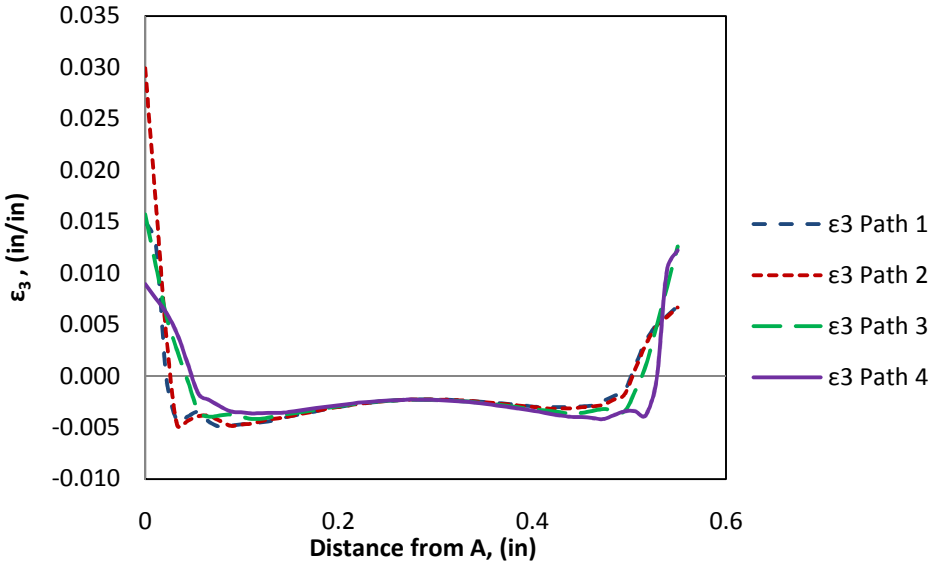

Fig.2.6.4 Variation of interlaminar normal strain (ε_3) along the gauge length (L) from A to B

From Fig. 2.6.3 it is clear that the tensile loading condition created only little shear in the middle of the gauge region. From Fig. 2.6.4 it is observed that the interlaminar normal strain is tensile at the ends and compressive in the middle. This showed that the failure in the gauge region is likely to initiate near the notches due to both shear and normal forces and not pure shear alone. Shokrieh et al. [46] reported similar results by using a double notched coupon of 90 degree laminae. For inducing pure interlaminar shear in the gauge area, Shokrieh et al. [46] performed a FEA study to find out the influence of notch size, gauge length and coupon thickness on the interlaminar shear response of the coupon and also to come up with a geometry that best suited shear failure. The optimized geometry was subjected to compressive loading condition. The gauge region showed very little shear effect in the middle and high stress concentrations at the notched ends as shown in Fig.2.6.5. To reduce the notch effect, the gauge region was subjected to compressive force in clamped condition as shown in Fig.2.6.6. The results improved a bit but the notch effect wasn't totally eliminated as shown in Fig.2.6.7. Thus a double notch shear test is not the most reliable experiment for finding yield shear stress in the composite.

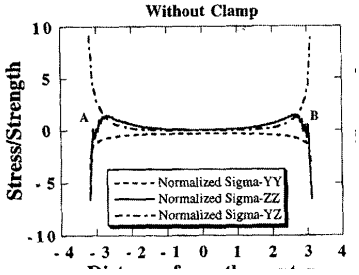

Fig.2.6.5 Interlaminar and normal stress in un-clamped double notch coupon [46]

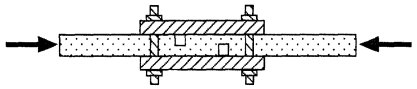

Fig.2.6.6 Clamped double notched coupon under compressive load [46].

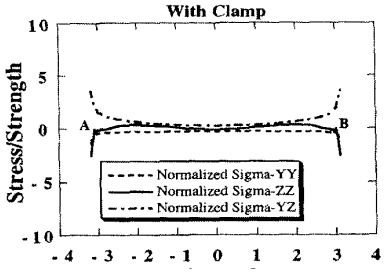

Fig.2.6.7 Interlaminar and normal stress in clamped double notch coupon [46]

2.7 Results

The 3D linear elastic model proposed in section 2.4 demanded a computational time of 40 minutes on a system running with a 3.14 GHz processor. This turned out to be a major drawback of the 3D model. For the current work, the strength optimization study was carried out by Stone [46] using a 2D FE model based on Classical Lamination Plate Theory. Because of a large number of runs required, 3D FE model for such a study was impractical. In order to use the results of 2D model in the current work it was necessary to compare its results with the proposed 3D model. The basis of such a comparison was that the in-plane stresses were dominant in the optimized laminate configurations until the yield point. The relevance of 3D model to strength prediction of laminates became evident when delamination was considered.

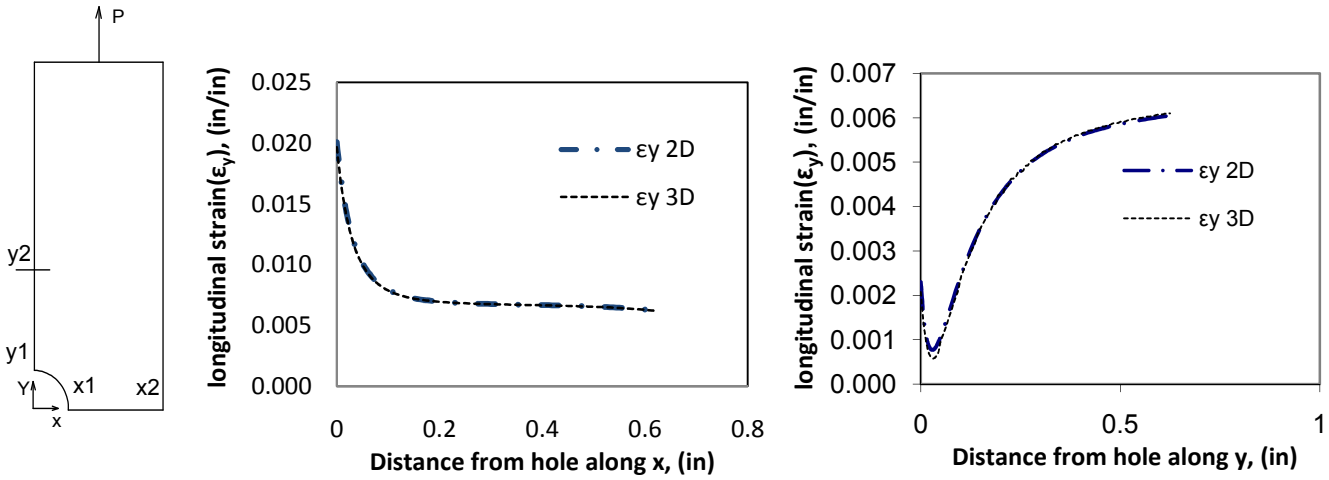

(a) (b)

Fig.2.7.1 (a) Variation of longitudinal direction strain (ε_y) along X direction using 2D and 3D FE model for Aluminum properties **(b)** Variation of longitudinal direction strain (ε_y) along Y direction using 2D and 3D FE model for Aluminum properties

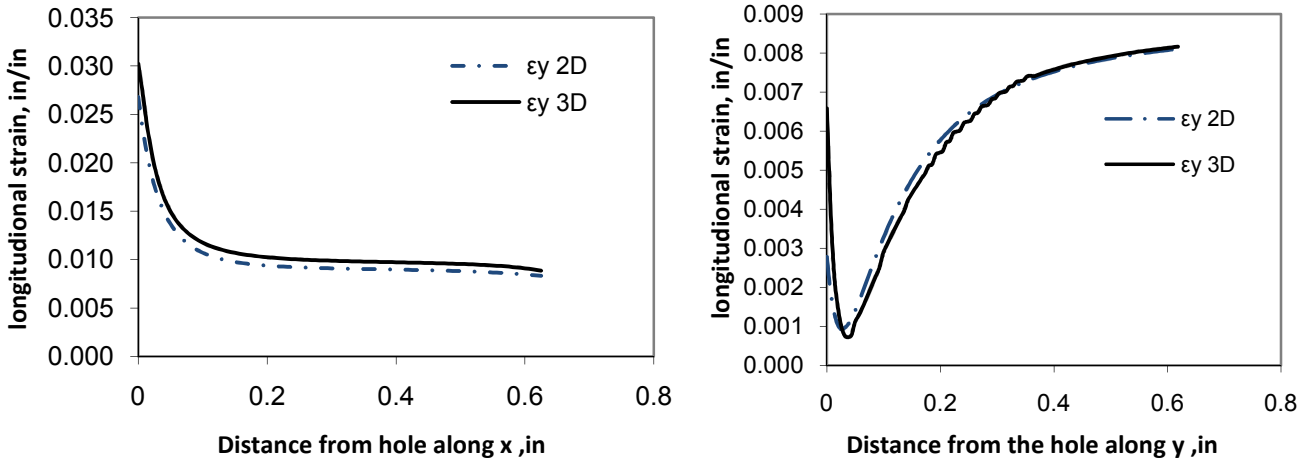

(a) (b)

Fig.2.7.2 (a) Variation of longitudinal direction strain (ε_y) along X direction using 2D and 3D FE model for T600:125-33 properties **(b)** Variation of longitudinal direction strain (ε_y) along Y direction using 2D and 3D FE model for T600:125-33 properties

Fig.2.7.1 draws a comparison between the 2D and the 3D model for longitudinal direction strain along x (from x1 to x2 in Fig.2.7.1) and y (from y1 to y2 in Fig.2.7.1). Both models used isotropic properties of Aluminum (Table 2.5.1). Identical results were obtained using both models. A similar comparison was drawn in Fig.2.7.2, but using T600:125-33 carbon/epoxy material properties for the Baseline laminate. The 3D model prediction was 13% higher than that of the 2D model at point x1 and 137% higher at point y1. Point x1 is the point of the maximum strain concentration and point y1 corresponds to that of minimum strain concentration. Both the strain concentration (K_t) and the First Ply Failure (FPF) predictions were based on the point x1 and hence the 137% difference in prediction of two models was of no consequence for the current work. The difference in the 2D and 3D models is a direct consequence of the free edge effect which seems to be more prominent at point y1 than at x1.

For the strength optimization study two approaches were used. One of the approaches had strain concentration as the governing parameter and the other was based on First Ply Failure (FPF) methodology. In the former, ply angles were altered one angle at a time and the corresponding

strain concentration factors were observed. The assumption of such an approach was that the decrease in strain concentration would mean a corresponding increase in the open-hole tension (OHT) strength of the laminated composite. The laminate configurations that were obtained are given in Table 2.7.1 along with their strain concentration factors and the ultimate tensile strengths (UTS).

Table 2.7.1 K_t optimized lay-ups

Description	Orientation	K_t 3D FEA	UTS[5] (Ksi)
Baseline (BL)	[(45/90/-45/0)2]s	2.86	71
Vary 45 (A)	[(54/90/-54/0)2]s	2.79	73
Vary 90 (B)	[(45/51/-45/0)2]s	2.67	73
Vary order 1 (C)	[(45/0/-45/90)2]s	2.89	69
Vary 0 (D)	[(45/90/-45/57)2]s	2.22	29
Vary 45 & 90 (E)	[(54/54/-54/0)2]s	2.36	69
Vary 0 & 90	[(45/52/-45/52)2]s	1.96	-
Vary 0 & 45	[(62/90/-62/62)2]s	1.99	-

Taking the baseline configuration and altering the 45 degree plies resulted in optimized configuration "vary 45". Similarly, the nomenclature was given to the lay-ups depending on which ply or plies were altered. An exception is "vary order 1" which was obtained by changing the stacking sequence of the 90 and the 0 degree plies. Some of the laminates in Table 2.7.1 have also been designated as BL, A, B, C, D and E. Vary0&90 and Vary 0&45 laminates were not among the other laminates (BL-E) that were fabricated. That reason being that after analyzing the vary 0 laminate it was clear that altering the main load bearing plies[6] caused drastic decrease in the OHT of the coupons.

[5] The UTS is average of 3 sets of coupons that were fabricated during the course of the research. The fabrication process was completed by collaborating with Stone, D.P. [46].

[6] The load bearing plies are the one which have the fiber axis parallel to the loading direction.

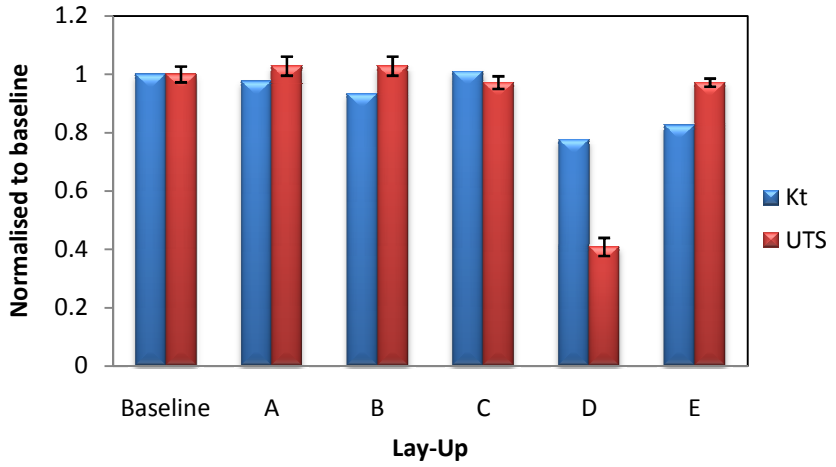

Fig. 2.7.3 Comparison of strength response of laminates using K_t and UTS.

To compare the strength response of laminates their K_t and UTS were normalized with respect to the baseline laminate (Fig.2.7.3). Laminates A (vary 45) and B (vary 90) had a 3% increase in the strength than the baseline. Laminate C (vary order 1) which showed a higher strain concentration than the baseline had a correspondingly lower UTS (3%). Both laminates D and E were expected to show higher strength than the baseline due to their reduced strain concentration factors. However, in both cases the results were lower, 2.8% and 59 % for E and D respectively. These results indicated that the strain concentration factor method is not a reliable measure of strength for composites.

To improve the optimization, failure criteria were considered. This demanded that a suitable failure criterion be chosen that could predict the strength of the laminates accurately. The 2D and 3D models were linear elastic in nature. Thus, First Ply Failure (FPF) Strength was considered since it occurs in the linear range of the composites.

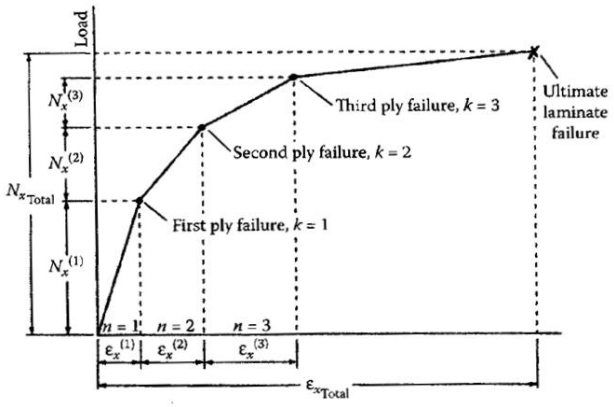

Fig. 2.7.4 Load strain curve for uniaxially loaded laminate showing multiple ply failures leading up to ultimate laminate failure [34]

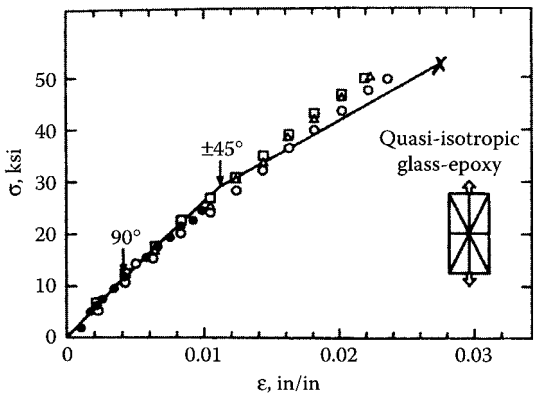

Fig.2.7.5 Comparison of predicted and measured stress-strain response of $[0/\pm45/90]_s$ glass/epoxy laminate [34]

The FPF of a laminate occurs when the first ply (or group of plies) fails. Thus the load corresponding to the FPF is not necessarily the laminate failure load. Fig.2.7.4 shows a piecewise linear laminate load-deformation curve with several "knee" points due to ply failure. The first knee point is considered to represent the FPF. Fig.2.7.5 shows a comparison between the FPF predicted by the maximum strain theory and the corresponding experimental data for a $[0/\pm45/90]_s$ glass/epoxy laminate. This curve has two knee points- the first one is at the strain corresponding to the failure of the 90 degree plies and the second one at the strain corresponding to the ±45 degree plies. However unlike Fig. 2.7.4 these knee points are not clearly defined. At high strains the experimental data does not show as much change in slope at the knees as the theoretical curve does. The actual ply failure occurs gradually over a finite strain range, whereas instantaneous ply failure at a single strain level is assumed in the analysis.

To find the FPF experimentally a new technique called the digital image correlation method (DICM) was used. This technique measures specimen displacements by finding correspondence between an image of the specimen in an undeformed or reference configuration and a second

image under load. The software for the current research was provided by Correlated Solutions, Inc. The system uses two high resolution digital cameras as shown in Fig.2.7.6 to record surface changes of the object under investigation. The cameras were placed at an angle to focus on the hole where damage was expected to occur.

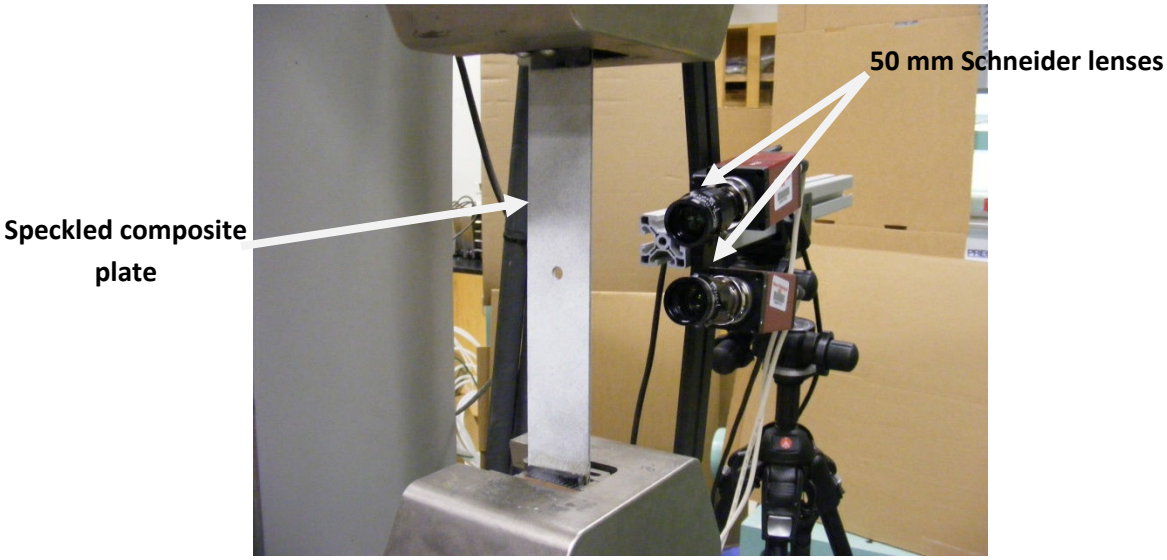

Fig. 2.7.6 Set up of the DICM instrument.

DICM is based on the principle of matching the pixel grey level values of a reference image and the deformed image. To generate these pixels the surface of the specimen was coated with a layer of paint to form speckle pattern as shown in Fig. 2.7.7 (a). The speckle should be uniform throughout the specimen and should not degrade with the application of load.

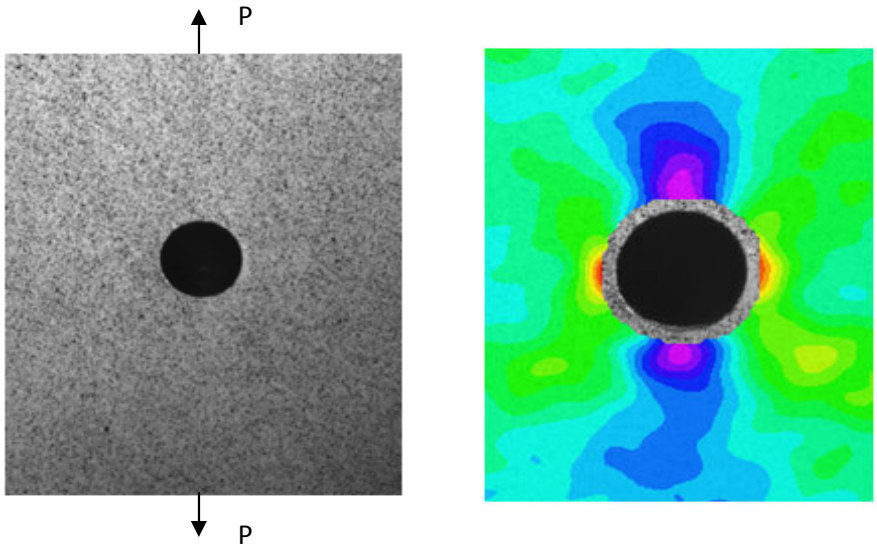

(a) (b)

Fig. 2.7.7 (a) Speckle pattern near the hole of Baseline laminate **(b)** Longitudinal strain profile of 3D model near the hole of baseline laminate at 70.5 Ksi (90 % UTS)

Once the load is applied, the speckled images are registered by the software and discretized into subset. Each subset is an n×n pixel window that surrounds a data point forming a strain section. Each subset of a reference image is then matched with the corresponding subset of a deformed image creating a displacement field. The displacement field information is then used to calculate strain at each data point (Fig.2.7.8). There are algorithms and error functions that used to perform this correlation which are explained elsewhere [46, 47, 48, 49]. Fig. 2.6.7 (b) shows the longitudinal direction strain field near the hole of the baseline laminate at 18% UTS.

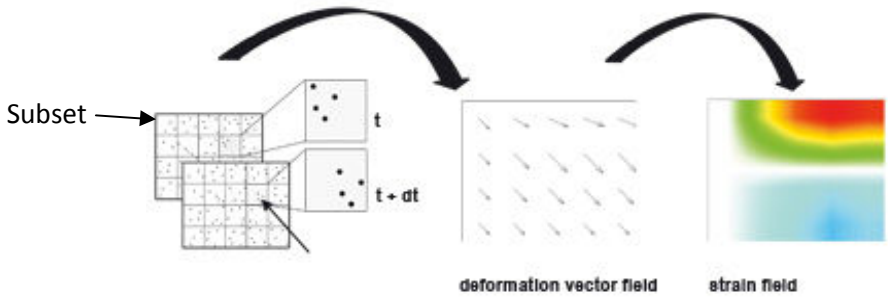

Fig.2.7.8 Steps in extraction of strain field in DICM.

The subsets are spaced by a step size. Each step size denotes the increment that should be applied to a subset. This is equivalent to the elements of FEA mesh with the exception that subsets can

overlap if the step size is smaller than the subset size. A higher element density in the region of interest improves the accuracy of the solution. Similarly, a smaller step size yields more data points and better surface contours but requires more analysis time. For the current research a step size of 10 and subset size of 40 was chosen. The detailed description of the choice this subset and step size can be found somewhere else [46]. This combination resulted in higher accuracy with less computation time. From Fig.2.7.7 (b), the strain contours do not start from the edge of the hole. DICM can only go half a subset size from the edge of the hole, which is 0.022 inches for the subset of 40.

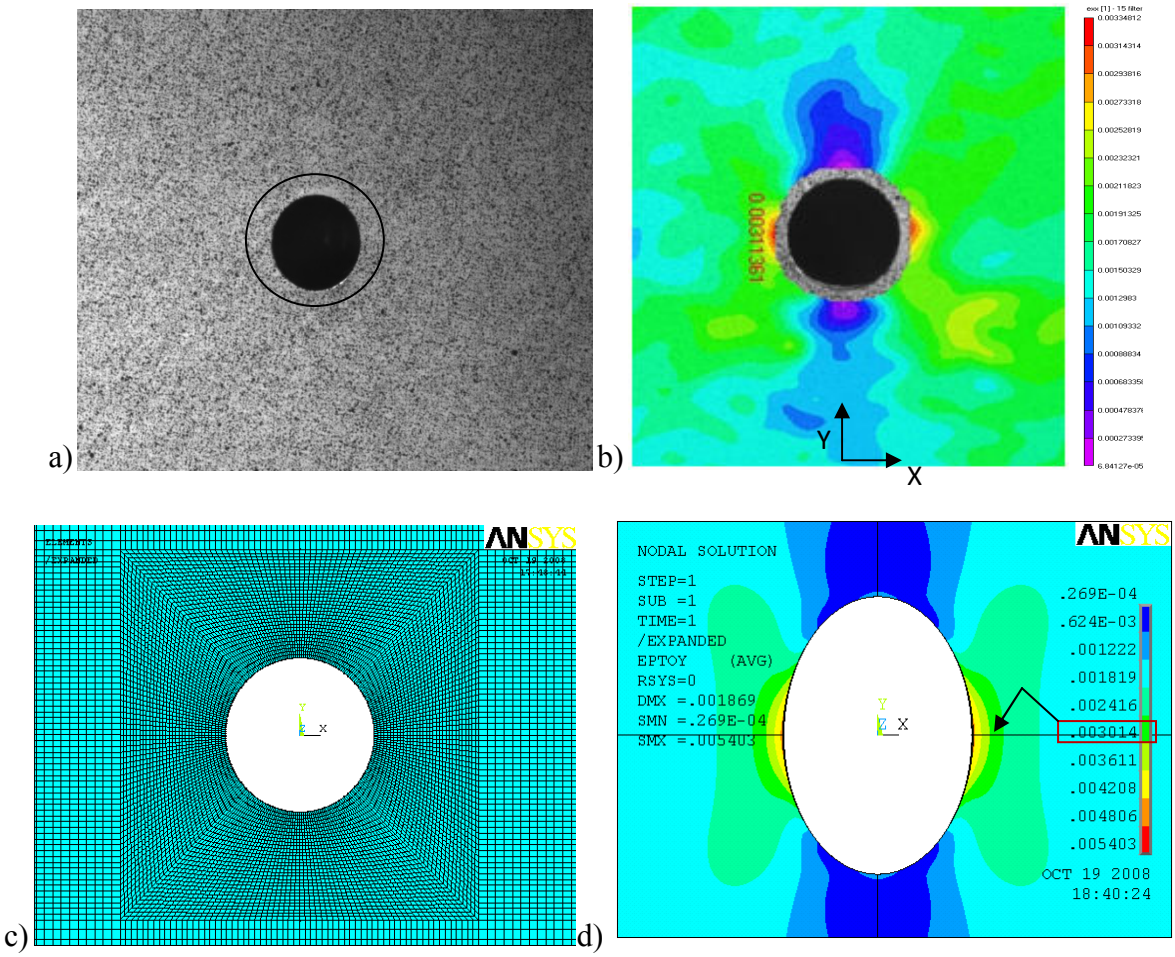

Fig.2.7.9 (a) DICM speckle pattern of baseline laminate with circular offset zone. **(b)** Longitudinal strain contour of baseline at 13 Ksi (18% UTS) **(c)** 3D model mesh of baseline laminate **(d)** Longitudinal strain contour of 3D FE model of baseline at 13 Ksi (18% UTS).

Fig. 2.7.9 (b) and (d) compare the longitudinal strain contours of baseline laminate using DICM and 3D FEA respectively. The load in both cases was 18% of the UTS. The maximum strain concentration is 90 degrees to the loading direction (Y). To compare the FEA result the same offset was applied by calculating the node number which corresponded to the 0.022 inch distance from the edge of the hole. The best approximation of the required distance was achieved at the 5th node from the edge of the hole. DICM and 3D FEA predicted a longitudinal strain value of 0.0031161 and 0.003014 respectively at the point of interest with a difference of 3.38%.

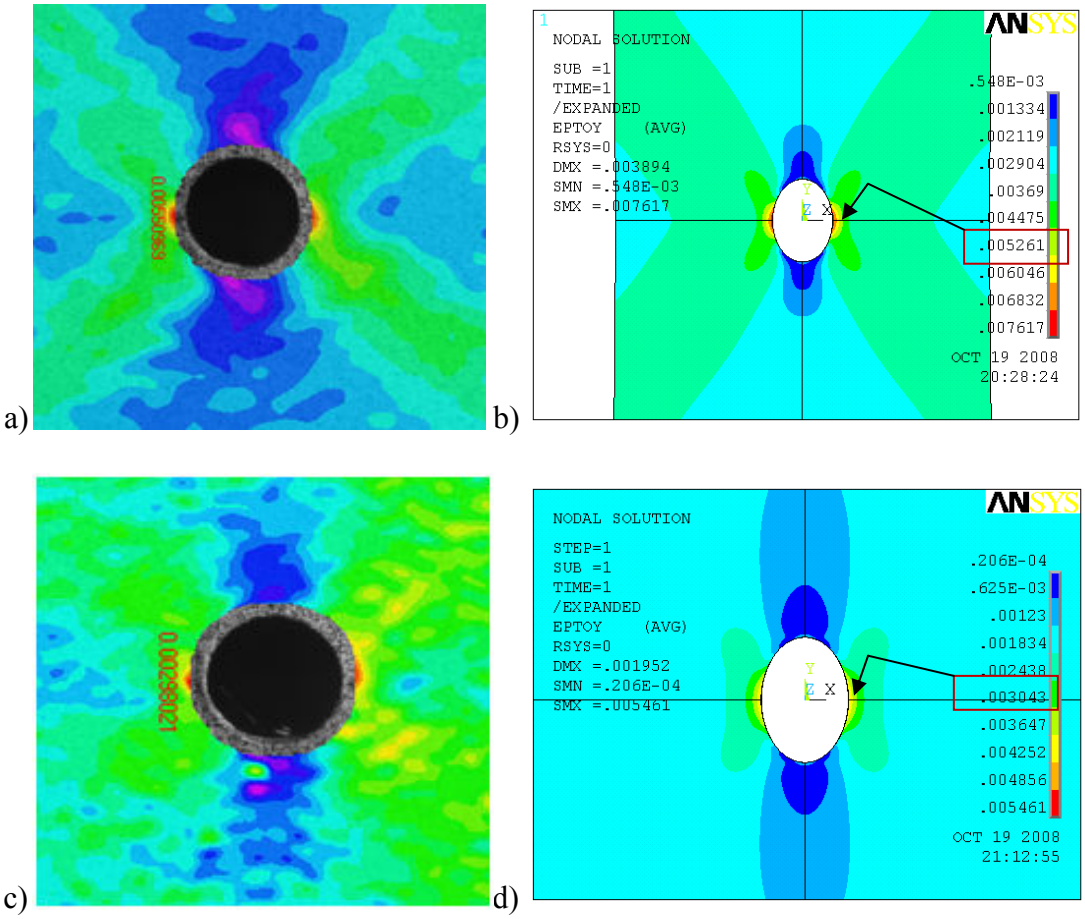

Fig.2.7.10 (a), (b) Longitudinal strain contour for $\left[(\pm 45)_4\right]_s$ at 7.5Ksi (41% UTS) using DICM &3D FEA respectively **(c), (d)** Longitudinal strain contour for A laminate at 9Ksi (13% UTS) using DICM &3D FEA respectively

Fig. 2.7.10 (a) and (b) compare the longitudinal direction strain contour of DICM and 3D FEA respectively at 41% UTS for a $\left[(\pm 45)_4\right]_s$ laminate. This laminate was introduced to compare the strain prediction of DICM and FEA and was not part of the optimization process. DICM and FEA predicted a strain of 0.055 and 0.005261 respectively at the offset distance of 0.022 inch from the point of the maximum strain concentration. A Similar process was repeated by using laminate A at 14% UTS as shown in Fig. 2.7.10 (c) and (d). In Fig. 2.7.9 and Fig. 2.7.10 DICM and FEA agreed well with each other in the zone of maximum strain concentration.

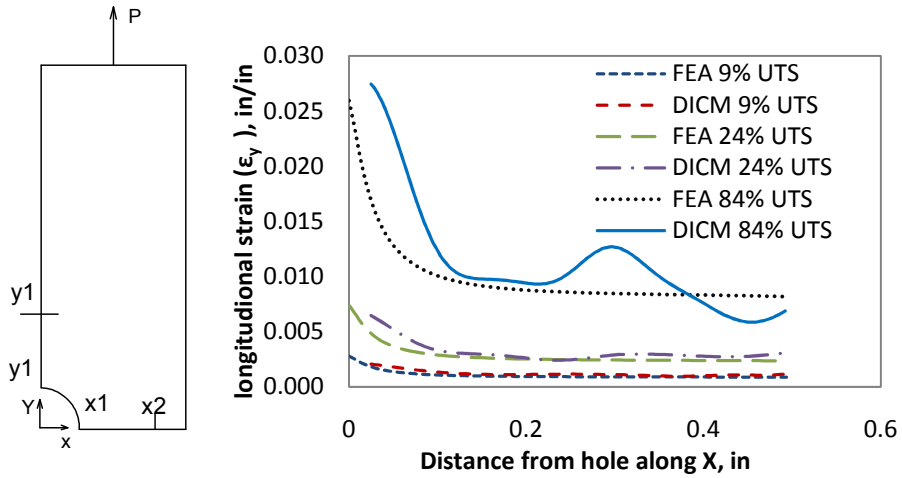

(a)

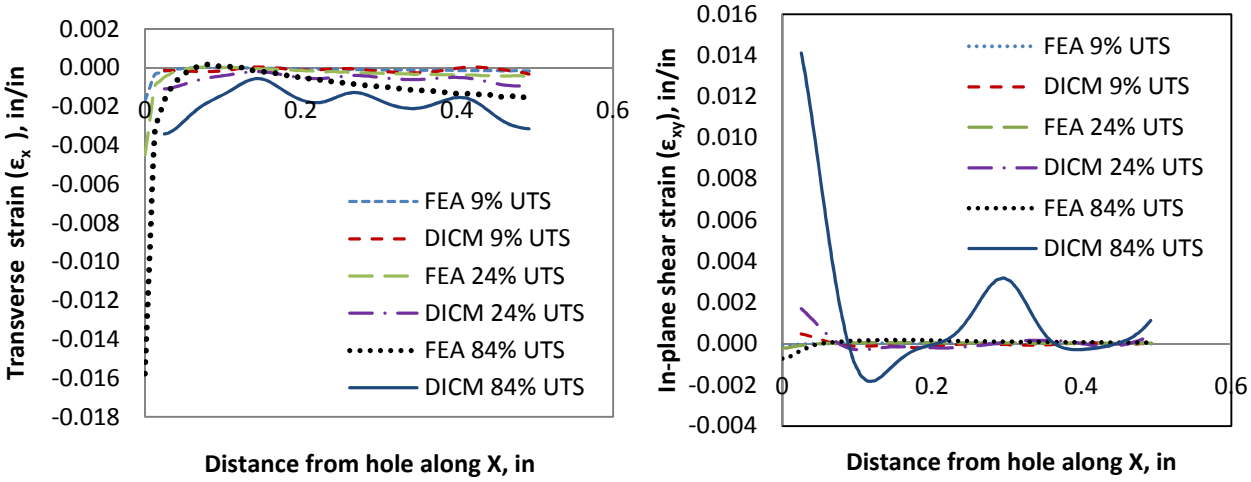

Fig. 2.7.11 (a), (b), (c) Comparison of 3D FEA with DICM for longitudinal, transverse and in-plane shear strain respectively along X direction of the hole for BL-1-4.

The coupons were fabricated in three groups with 4 to 5 coupons in each group. BL-1-4 stands for the forth coupon of group one of baseline series. Fig. 2.7.11 (a), (b), (c) provide a comparison between DICM and FEA strain predictions in longitudinal, transverse and in-plane shear direction respectively along X. The strains for FEA and DICM were extracted along the edge of the hole on the surface from x1 (0.125, 0) to x2 (0.5, 0) as shown in Fig. 2.7.10 (a). The comparison of the strain state along X was drawn for 3 load steps of 7ksi (9% UTS), 17 Ksi (24% UTS) and 60 Ksi (84% UTS). The longitudinal strain was positive for all load steps as expected for a tensile loading condition while the transverse strain was negative due to the Poisson's effect. In Fig. 2.7.11 (a) the correlation between 3D FEA and DICM changed from 12% at 7ksi (9%UTS) to 38% at 60Ksi (84% UTS). For the transverse strain the difference ranged from 10% at 7Ksi (9% UTS) to 56% at 60 Ksi (84% UTS). For the in-plane shear the difference corresponding to 84% UTS was 102% making it the worst case scenario.

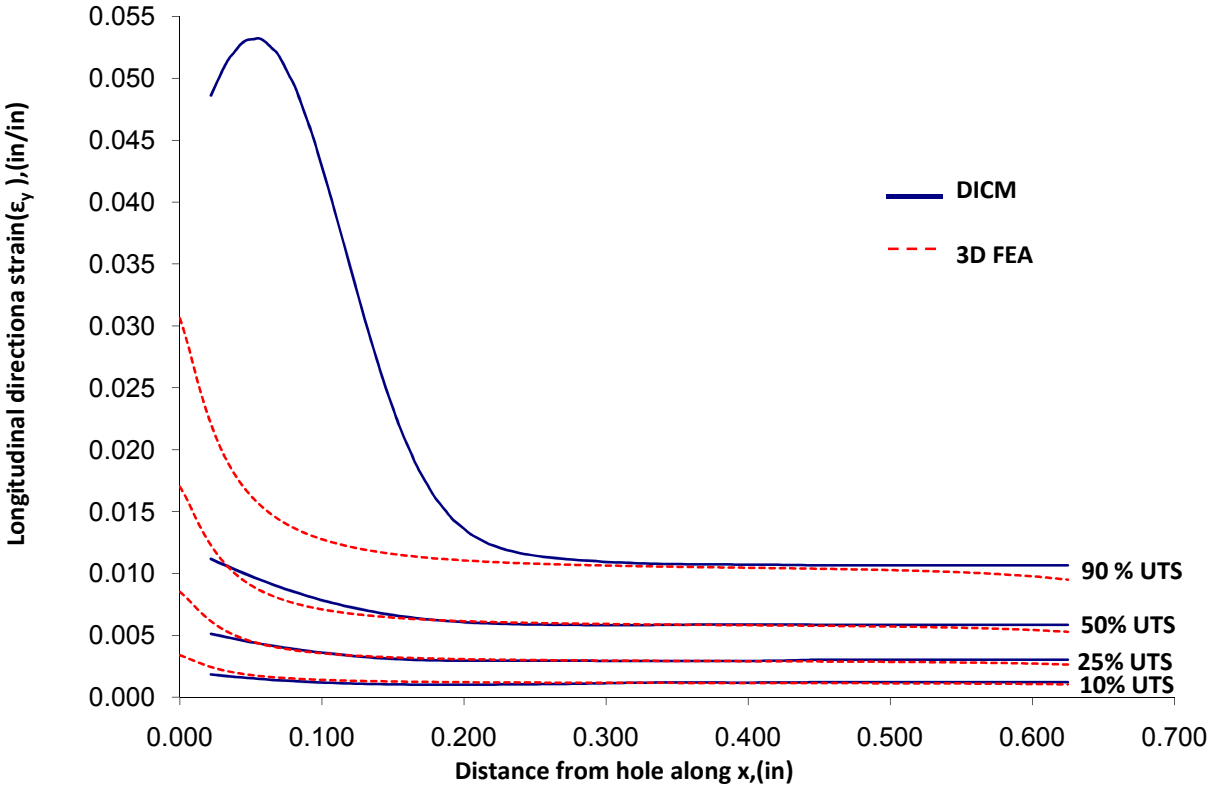

Fig.2.7.12 DICM Vs 3D FEA for laminate A

Fig. 2.7.12 compares the longitudinal direction strain between DICM and 3D FEA model for 10%, 25%, 50% and 90% of the UTS. Laminate A was selected for this comparison. The longitudinal direction strain profile between DICM and 3D FEA agreed well till 25% UTS. At loads approaching 90% UTS the correlation deteriorated. From Fig. 2.7.11 (a), (b), (c) and Fig. 2.7.12 it is clear that the DICM and 3D FEA correlate well with each other under 25% UTS. At higher loads (≥84) geometric and material non-linearity effects lead to poor correlation between the two methods.

Using DICM, FPF was defined as the point where the proportional line and the stress-strain curve deviated from each other. Fig. 2.7.13 shows the applied stress Vs longitudinal strain curve for the three sets of baseline laminates that were fabricated for this work. In depth study of the use of DICM for obtaining the stress-strain curves and deriving FPF from them can be found in [46].

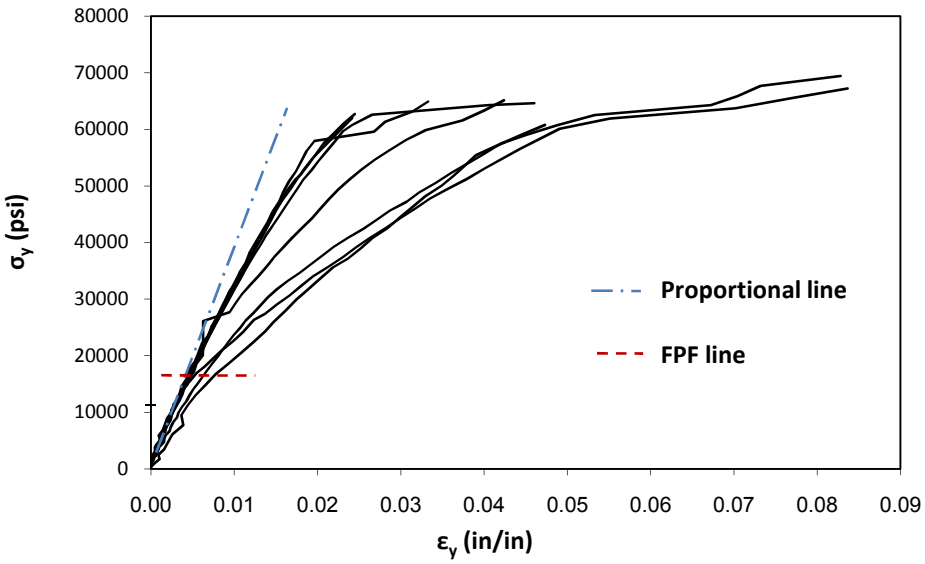

Fig.2.7.13 Applied stress Vs Longitudinal strain for set of Baseline laminates [46]

The purpose behind using the DICM for OHT test was its ability to spatially extract strains near the edge of the hole where the damage was expected to occur. These predictions could then be

compared with the FPF prediction of the failure criteria introduced in sections 1.5.1 and 1.5.2. The failure criteria application for the current work was concentrated near point A (Fig. 2.3.5). The 3D model had two elements per ply as shown in Fig. 2.7.14 which meant that each ply along the edge of the hole had 3 nodes of which 2 were shared with the neighboring plies except for the free edge plies.

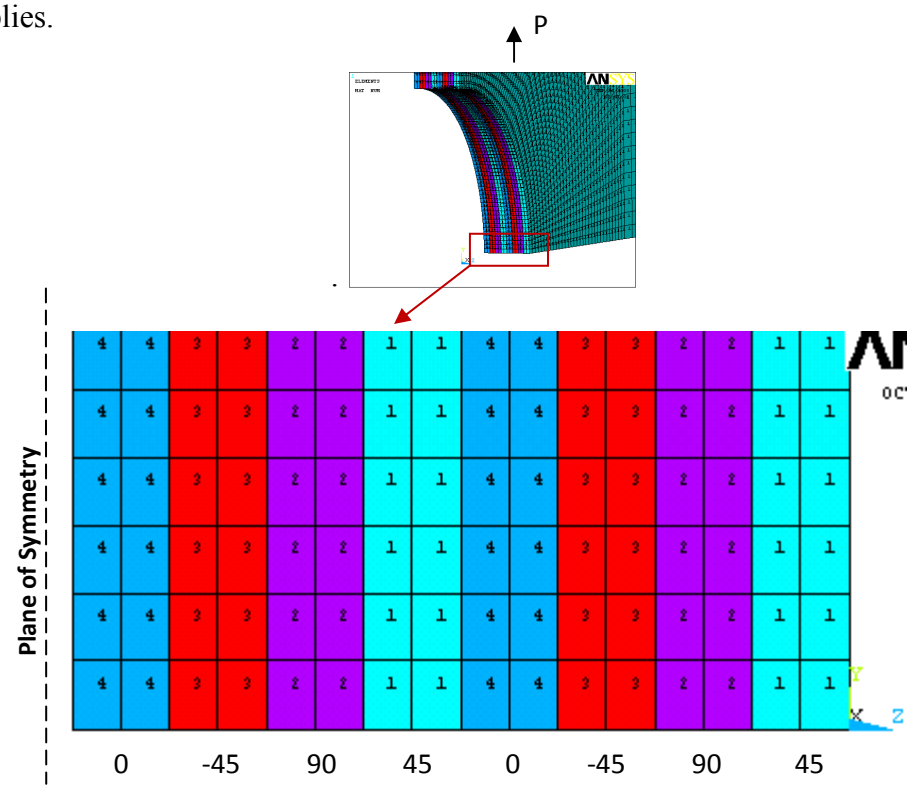

Fig.2.7.14 FE mesh of one-eighth model near the edge of the hole for baseline laminate.

A static load applied to the FE model in the y direction produced a 3D strain state at each node along the edge. The strains extracted from ANSYS were in the reference coordinate system (X-Y-Z). The values were converted into the principal material coordinate system by using 3D form of equation 2.3.4. For a node shared by two plies this transformation resulted into two strains one for each of the plies that share it. It is because the transformation matrix T_{3D} is a function of ply angle and would thus generate two sets of strains for the shared node. Principal stresses were obtained from principal strains from equation 2.3.3. Each failure criterion generated a failure index (*f.i*) at each node along the edge of the hole. The tendency of failure was governed by the

magnitude of *f.i*. The node with highest *f.i* would have the tendency to fail first and hence result in FPF. The FPF stress was calculated for each node by the equation.

$$FPF = \frac{P}{f.i.} \tag{2.7.1}$$

where P is the applied tensile stress as shown in Fig. 2.7.14 and *f.i* is the failure index which is defined as

$$f.i = \frac{\varepsilon_{iFEA}}{\varepsilon_{iMax.}} = \frac{\sigma_{iFEA}}{\sigma_{iMax.}} \tag{2.7.2}$$

$$f.i = \frac{\varepsilon_{ijFEA}}{\varepsilon_{ijYield.}} = \frac{\sigma_{ijFEA}}{\sigma_{ijYield}} \tag{2.7.3}$$

where *i, j* = 1, 2, 3. Equations 2.7.2 and 2.7.3 were used for maximum strain and maximum stress failure theories. As explained in section 2.3 the normal stress and strain components show linear behavior and hence their ultimate or maximum stress and strain values can be used to find the failure index as shown in equation 2.7.2. However, we have found that the shear is non-linear in nature and hence to find the *f.i.* in this case the stress and strain values should be divided with the corresponding yield stress and yield strain as shown in equation 2.7.3. Failure index for the interactive criteria is the left hand side of their 3D failure criteria equations.

Table 2.7.2 provides comparison between the FPF strength of lay-ups optimized by strain concentration method. Fig.2.7.15 provides the same comparison in graphical form. The error bars in Fig.2.7.15 are the standard deviations of 3 sets of coupons tested using DICM. The FPF predicted by the DICM [46] agreed well with that predicted by Max-Stress and Max-Strain theories. Hashin-Rotem, Tsai-Hill, Tsai-Wu and Hoffman under predicted the FPF strength of all the laminates. The energy criterion results were also conservative for all but one laminate (Laminate C), for which case the FPF strength was over predicted.

Table 2.7.2 FPF strength values for Kt optimized laminates using DICM and 3D failure criteria.

lay-up	DICM	Max-Stress	Max-Strain	Hashin-Rotem	Tsai-Hill	Tsai-Wu	Hoffman	Energy
Baseline	10.88	9.43	9.69	0.64	1.75	1.09	1.06	4.76
A	9.82	9.03	9.183	0.88	2.48	2.32	2.15	5.32
B	16.51	14.7	16.12	0.24	2.44	2.12	2.3	2.88
C	11.76	11.24	11.30	3.1	0.45	0.21	0.2	14.76
D	6.68	6.12	6.23	0.013	0.03	0.08	0.012	0.23
E	18.37	17.7	17.02	0.2	0.45	0.31	0.32	2.12

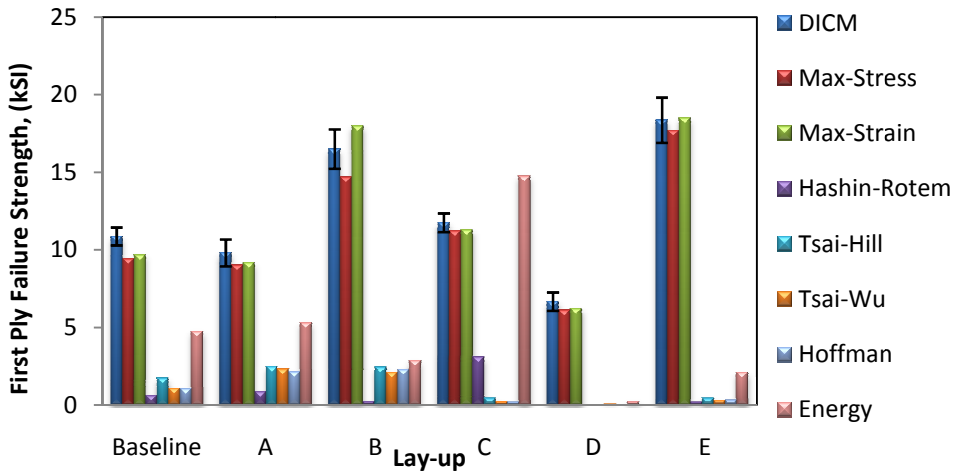

Fig.2.7.15 Comparison of FPF strength of Kt optimized laminated using DICM and failure theories.

Of the two theories, Max-Strain was able to predict FPF more accurately than Max-Stress. Thus the optimization study was continued using the Max-Strain theory with FPF strength as the governing parameter.

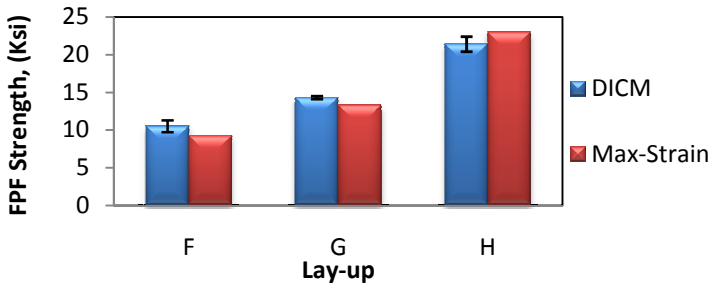

Fig.2.7.16 Comparison of FPF of laminates optimized using Max-Strain theory with DICM.

Fig.2.7.16 compares the FPF strength of the laminates optimized by the Max-Strain criterion. Laminate C (vary order 1) was found to have higher FPF strength than the baseline. This supported the theory than stacking sequence change can alter the FPF. Vary order 2 (Laminate F) was thus included in the current study to observe the effects of further change in the stacking sequence. It was not the part of K_t or FPF optimization methodology. Using the Max-Strain theory the orientation of 45 and 90 degree plies was altered to find maximum FPF. Laminate G was obtained by varying the 45 and laminate H was obtained by varying the 90 degree ply. Varying 0 degree layer reduced the FPF and UTS and thus was not considered. H had the greatest improvement in strength, 97% higher than the baseline FPF. It was followed by laminates E, B, G, and C with 69%, 52%, 31% and 8% increase in FPF strength respectively than the Baseline. Laminates A, D and F had FPF strength lower than the baseline by 9%, 38% and 4% respectively. The final set of laminates is summarized as

Table 2.7.3 Final set of fabricated laminates along with the method of optimization.

Orientation	**lay-up**	**Optimization method**
$[(45/90/-45/0)2]_S$	Baseline	-
$[(54/90/-54/0)2]_S$	A	Kt
$[(45/51/-45/0)2]_S$	B	Kt
$[(45/0/-45/90)2]_S$	C	literature
$[(45/90/-45/57)2]_S$	D	Kt
$[(54/54/-54/0)2]_S$	E	Kt
$[(45/-45/90/0)2]_S$	F	literature
$[(21/90/-21/0)2]_S$	G	FPF
$[(45/0/-45/0)2]_S$	H	FPF

Table 2.7.4 Mode of first ply failure along with the ply failed.

Orientation	Lay-up	FPF Stress (Ksi)	Ply Failed at FPF	Mode of FPF
$[(45/90/-45/0)2]_S$	BL	9.69	90	ε_2
$[(54/90/-54/0)2]_S$	A	9.18	90	ε_2
$[(45/51/-45/0)2]_S$	B	16.12	45	ε_{12}
$[(45/0/-45/90)2]_S$	C	11.30	90	ε_2
$[(45/90/-45/57)2]_S$	D	6.23	90	ε_2
$[(54/54/-54/0)2]_S$	E	17.02	54	ε_{12}
$[(45/-45/90/0)2]_S$	F	9.23	90	ε_2
$[(21/90/-21/0)2]_S$	G	13.3	90	ε_2
$[(45/0/-45/0)2]_S$	H	23	-45	ε_{12}

Max-strain failure theory was also used to find out the modes of first ply failure and the laminae which were supposed to fail at FPF load (Table 2.7.4). According to Max-Strain failure theory FPF in most of the laminates was predicted to occur transverse to the fiber direction, indicating matrix cracking. However, as shown in Table 2.7.4 some laminates had tendency to have FPF in form of in-plane shear. From the optimization study and the mode of FPF failure of the laminates some conclusion could be drawn. In case of H laminate the 90 degree plies were replaced with the 0 degree plies that dramatically enhanced it load bearing capability. Apart from H the other laminates that showed increase in FPF strength were E, B, G and C. Again G was optimized by Max-Strain theory and thus its FPF strength increase was not surprising. However, the FPF results of laminates E, B and C that were optimized using K_t were quite surprising. In laminates B and E the FPF failure mode was in-plane share, the same as in case of laminate H. This can be due to shifting of 90 degree plies. In all other laminates with 90 degree plies, the FPF failure mode was transverse in nature which would mean matrix cracking and relatively lower resistance to applied stress than an in-plane shear mode where the fibers would redistribute some of the applied stress in the lamina and increase its resistance to failure. In laminate C it seems that moving the 90 degree laminate further inside and away from the free edge lead to higher FPF. Apart from these there were laminates that performed poorly in terms of FPF strength. As

mentioned earlier laminates A, D and F had FPF strength lower than the baseline. D laminate had the lowest K_t and still was the weakest of all the laminates. Due to removal of the primary load bearing plies this laminate basically behaved as a shear coupon and showed least FPF and UTS strength. In laminate A ±45 degree laminae were replaced by ±54 degree plies. This seems to have lowered the FPF strength as the plies were moved away from the main load bearing angle.

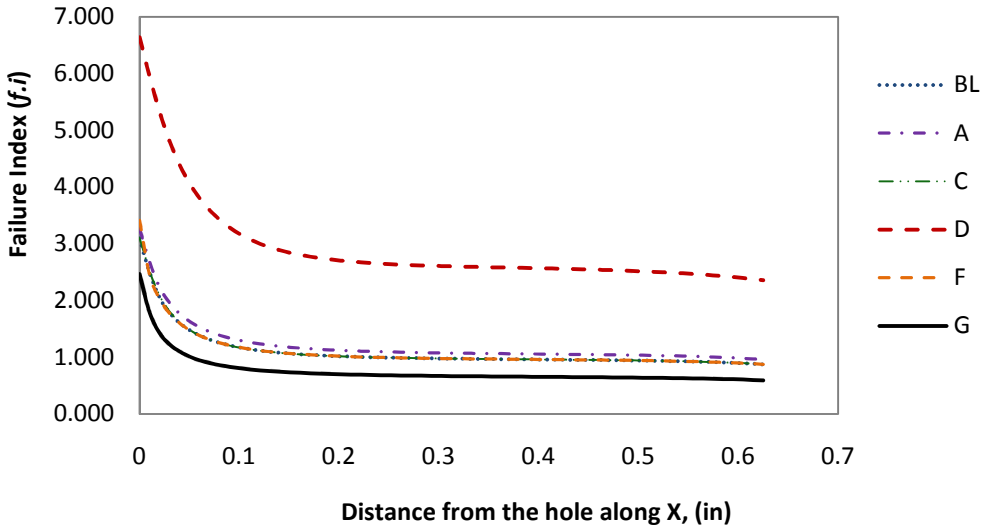

Fig.2.7.17 Failure Indices (*f.i*) Vs X distance along the hole at the lamina location where FPF is predicted in transverse mode

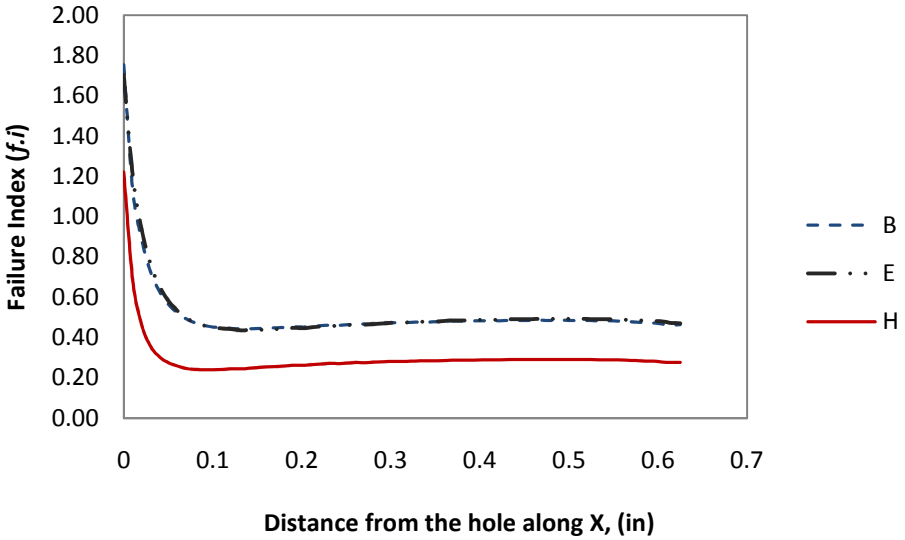

Fig.2.7.18 Failure indices (*f.i*) Vs X distance along the hole at the lamina location where FPF is predicted in in-plane shear mode

Fig.2.7.17 shows the variation in the failure indices (*f.i*) along the x axis at the location along the edge of the hole where Max-Strain theory predicted FPF in transverse direction. Fig. 2.7.18 provides the similar comparison for laminates where FPF was expected in shear. Both these figures provide a qualitative method of comparing laminates having higher FPF when all lay-ups were exposed to the same load. In Fig.2.7.17 the D laminate showed the highest failure index in the transverse direction in a 90 degree ply. Laminate G showed a minimum failure index in the 90 degree ply which obviously contributed to its high FPF. In Fig.2.7.18 the *f.i* of the 54 degree ply of B laminate was higher than that of -45 degree ply of E laminate which in turn was higher than the *f.i*. in -45 degree ply of H laminate. The FPF strength followed the reverse order with H being the strongest and B being the weakest.

The plots in Appendix A-3 compare the failure indices (*f.i*) of the laminates involved in this study. These failure indices were determined at the location near the edge of the hole where Max-Strain failure theory predicted FPF. The failure indices have been derived for all six strains (3 normal and 3 shear) along X direction (Fig. 2.7.11 (a)) of the hole. By comparing the *f.i.* derived for strains in 1, 2, 3, 12, 23 and 13 directions one can observe that among all the laminates involved in this study, failure modes in transverse (2) and in-plane shear (12) direction dominated the FPF. An important observation was with regard to laminate G where the *f.i* in out of plane shear (23) direction was very close to the *f.i* of transverse (2) direction. This meant that the interlaminar shear in this laminate could affect its strength as the damage progressed. G laminate has been treated separately in section 4.4.

The FPF mode was verified using SEM. The region of interest was the edge of the hole at 90 degrees to the loading direction (y direction). The process of creating specimen for SEM analysis is explained in section 3.2 of chapter 3. Before sectioning, the laminates were subjected to the FPF load. If the predicted FPF was correct, cracks would be visible at the desired location.

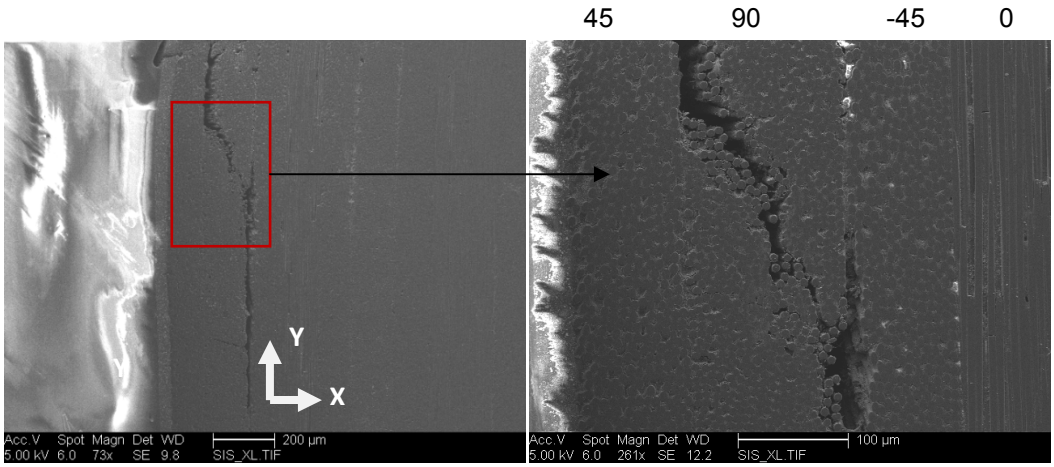

Fig.2.7.19 Crack in the 90 degree ply of baseline laminate in 2 direction at FPF

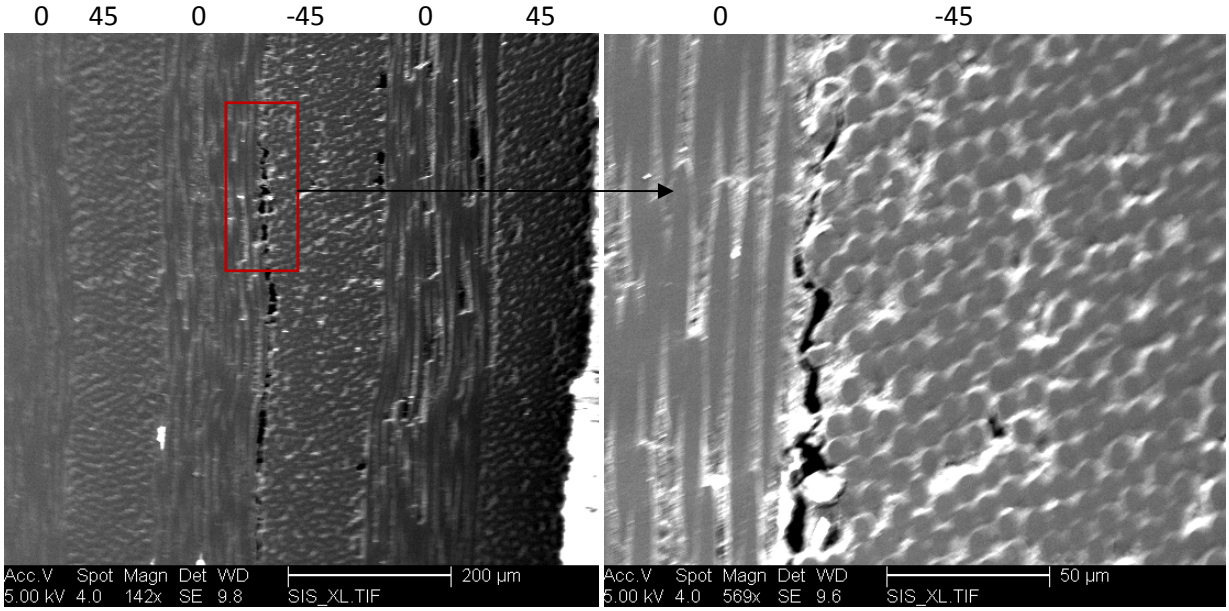

Fig.2.7.20 Crack in the -45 degree ply of H laminate in 12 direction at FPF

Fig. 2.7.19 shows a crack in the 90 degree lamina in baseline laminate in transverse (2) direction. The load was acting in the Y direction as shown in the same figure. The FE model predicted the FPF at the node shared between 45 and 90 degree lamina. From the image it can be assumed that the crack initiated at the interface of 45/90 lamina and propagate through the 90 degree lamina splitting it along transverse direction. Fig.2.7.20 shows a crack at the interface of -45 and 0 degree lamina of the H laminate. The 3D FE model for H laminate using Max-Stain theory predicted FPF at the interface of -45 and 0 degree lamina in form of in-plane (12) shear.

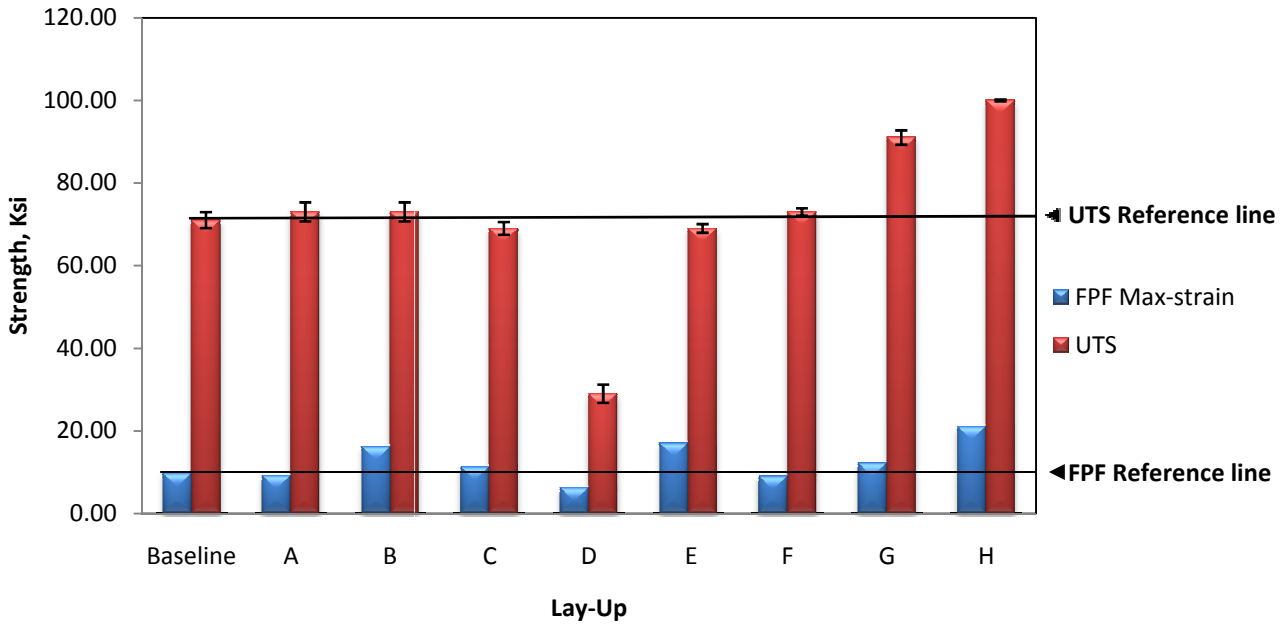

Fig.2.7.21 Trend followed by FPF and UTS of laminates

Fig.2.7.21 compares the FPF predicted by Max-Strain theory of the 3D FE model with the measured UTS. The FPF and the UTS reference lines are to compare with the baseline lay-up. Lay ups A, D and F have FPF strength less than the Baseline. The UTS of lay-ups A and F is higher than the baseline while that of D is lower than the baseline. B, C, E, G and H have FPF strength higher than the baseline. The UTS of B, G and H is higher than the baseline UTS while that of C and E is lower. This indicated that although increasing FPF is a novel method of finding laminates that can resist damage initiation but it is not a guarantee that the laminates having higher FPF will have a higher UTS too. For most applications the FPF methodology of strength optimization is a conservative one.

2.8 Chapter Summary

A 3D linear elastic model was proposed to capture the through thickness strain field near the hole of the composite plate. The model was linear elastic in nature and compared well with the analytical solution as well as with the experimental method (DICM). 3D model and DICM had good correlation for applied stresses less than 25% UTS. At stresses approaching 50% and higher this correlation degraded due to material and geometric non-linearity. The model evaluated the strength response of non-traditional laminates using strain concentration factor and FPF strength methodology. Strain concentration factor was not found to be a reliable test of the strength of a laminate e.g. the D laminate had the lowest strain concentration factor and was still the weakest of all the laminates. Hence, an FPF based study should be preferred. Seven failure criteria were used to estimate the FPF strength of the laminates. Max-Strain failure theory was found to correlate best with the FPF predicted by the DICM. Max-Strain failure theory was also able to predict the location and the mode of FPF near the hole of the composite laminate. SEM was used to verify the "mode of failure" results for baseline and H laminate. Both laminates had FPF at the locations and in the mode in which they were predicted by the 3D model. The chapter ended with a note of caution that the FPF and the UTS of a composite laminate may or may not be linearly related. Increase in FPF strength can lead to increase in UTS like in laminates B, G and H whereas in some laminates like C and E, the UTS was found to be lower than the baseline even though they had a comparatively higher FPF.

3. Manufacturing

3.1 Fabrication

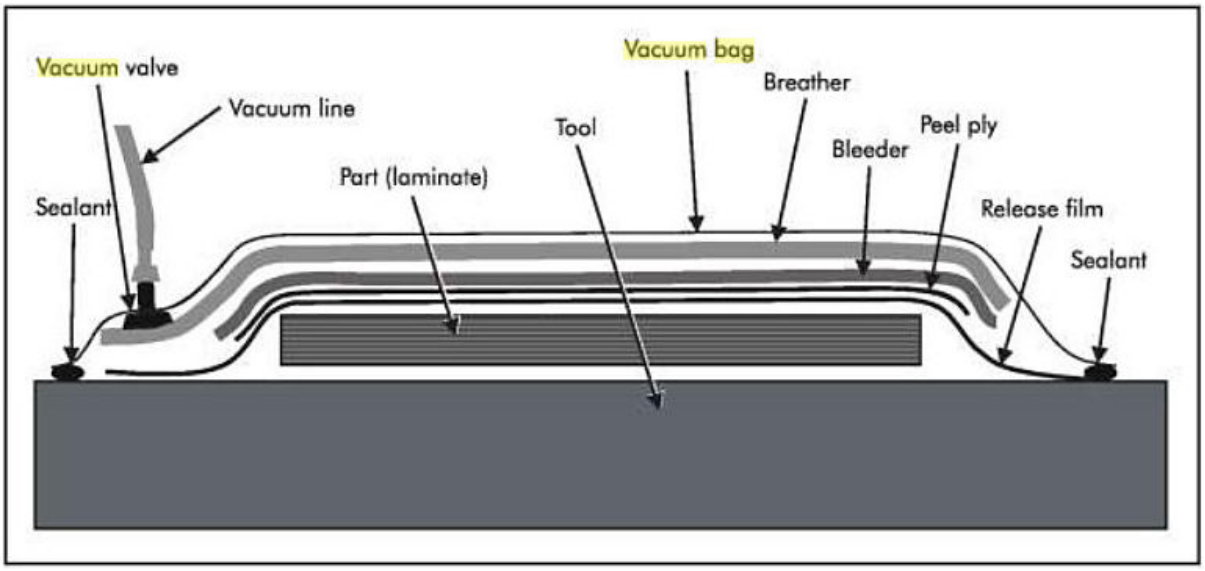

Fig.3.1.1. Schematic of fabrication set up [50]

The composite plates were fabricated using hand lay-up system. Fig.3.1.1 shows the schematic of a typical hand lay-up system. This system involved lying plies of precut prepreg into a mold. Prepreg stands for pre-impregnated materials. They are reinforcement fibers or fabrics into which a pre-catalyzed resin system has been impregnated by a machine. The prepreg resins can only be fully cured by heating them to the prescribed cure temperature. Prepreg is usually rolled into tape and kept in a freezer to slow down the cure process. Care should be taken while handling the prepreg material as direct contact with hand can contaminate them and degrade the material properties. Prepreg was cut to form plies of desired angles on a clean table to prevent contact with any impurities. The mold or tool was an aluminum plate of 30.5in×8in×0.25in dimensions. Before placing the plies on the mold it was cleaned with acetone. A water based P.T.F.E. mold release agent was applied on the mold. Care was taken than no air bubbles formed on the surface as this could lead to non-uniform application of release agent. Mold release agents

are thermally stable and can withstand a temperature of 450^0 F. Mold release was allowed to dry up for 20 minutes.

The plies were stacked on top of each other to form the part as shown in Fig.3.1.1. Pressure was applied on the stack of plies with a roller to take out any voids between two prepreg layers. Voids cause non-uniform properties and also reduce the fiber volume fraction. Release film or peel ply covered the laminate stack. The purpose of peel ply is to provide a simple method of removing the bagging material off the part after curing. Generally, the release film material is porous to permit excess resin to flow through it. As shown in Fig.3.1.1 a breather cloth covered the peel ply and a vacuum valve was placed on top of it. The breather material acted as distributor for air (vacuum) and for escaping volatile gases. Butyl tape was placed around the part. It acted as a sealant. The whole part was then covered by vacuum bagging. A small cross shaped cut was made on the vacuum bagging so that a vacuum valve would fit into vacuum nozzle.

After the bagging system was assembled it was placed in the autoclave for curing. The curing process used both vacuum and heat. Vacuum helps in consolidating the laminate's layers. This reduces the void content in the composite. This is important as interlaminar shear strength reduces by 7% for each 1% of void content present up to maximum of about 4%. A reasonable goal for void content in the finished laminate is 0.5% or less [50]. The curing was carried out at 350 ^{0}F and 90 Psig. The process started with a 10 minute ramp period with a soaking time of 45 minutes. This was followed by a slow cooling for another 45 minutes. After the part was cured the laminate plate was taken out and sent to WSU machine shop for cutting in 12in×1.5in plates. Waterjet system and an aerospace quality abrasive mixture was used for the cutting operation. The holes were drilled using a drill press.

3.2 SEM Sample Preparation

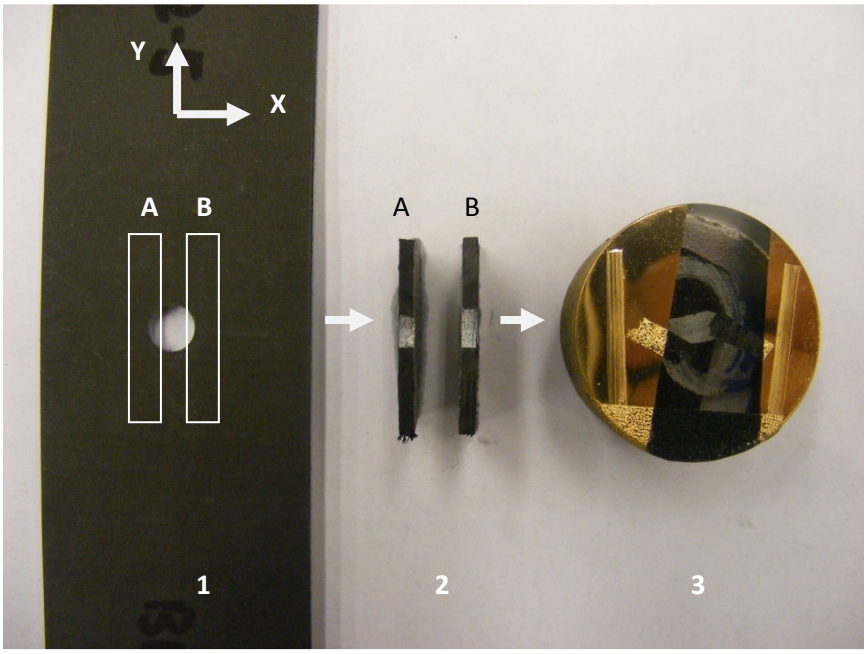

Fig.3.2.1. Steps in preparing SEM sample for FPF and Delamination study

Fig.3.2.1 shows the stages in preparing samples for analysis using SEM. The load was applied along Y direction. The laminates were first subjected to FPF or Delamination initiation load and then taken to a diamond saw cutter where two pieces were cut near the hole marked as A and B in image 1 of Fig.3.2.1. Care was taken while cutting near the hole so that the cutting process itself won't introduce any damage. The edge of the hole was not exposed to the cutter so the point was slightly depressed relative to the sample surface. Two white dots were put on the depressions as shown in image 2 of Fig. 3.2.1. An epoxy mold was prepared by mixing 6ml hardener with 35 ml resin. The two samples from image 2 were placed in 3M^{TM} Scotch-Weld^{TM} translucent epoxy adhesive with the dots facing down. Once the epoxy cured, the samples were ground to expose the dotted layer. Samples were polished with a 1µm solution, followed by a 0.05µm solution and finally a 0.03µm solution. The samples were cleaned in an ultrasonic cleaner and then rinsed with alcohol. Pressurized air was used to dry the samples. Before mounting the samples in the SEM, a conductive link was placed between the samples and the

base of the sample. This was done by running a strip of carbon tape all the way round the epoxy so that it touched the samples and the holder on which it was to be mounted. Image 3 in Fig. 3.2.1 was a sample for G laminate. The surface of the sample was sputtered with gold. Sputtering is a technique of applying a molecular layer of atoms to a surface. The image of the crack before sputtering was very blurry. Sputtering improved the electrical conductive of the sample and resulted in a much better image. Due to cost concerns this technique was used only for G laminate. The SEM images of other laminates used in this study (Baseline, H) were clearly visible without any sputtering treatment. Use of sputtering for other laminates (A, B, C, D, E, F) was redundant as damage due to manufacturing defects or during sample preparation made them unfit for further analysis.

4. Delamination

4.1 Introduction

A limitation of 2D models is that stresses in the z-direction are neglected (Fig.4.1.1). The accuracy of the 2D model decreases in regions with geometric discontinuities and free edges. Free edge perturbations decay rapidly with the distance from the laminate edge. These out of plane stresses are responsible for premature failure of laminates in the form of delamination. Pipes and Pagano [51] used a 3D elasticity approach to quantify interlaminar stress fields near free edges.

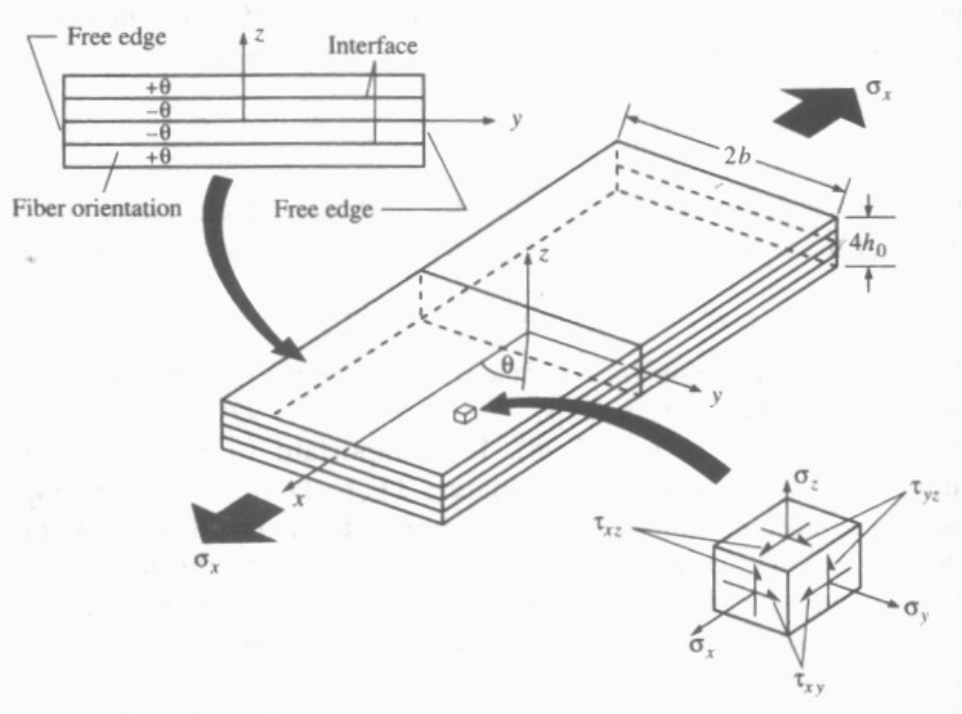

Fig.4.1.1 Pipes and Pagano model for analysis of interlaminar stresses in a laminate under uniaxial tension [51]

The three stress equilibrium equations from the theory of elasticity are [51]

$$\left(\frac{\partial \sigma_X}{\partial X}\right)+\left(\frac{\partial \tau_{XY}}{\partial Y}\right)+\left(\frac{\partial \tau_{XZ}}{\partial Z}\right)=0 \tag{4.1.1}$$

$$\left(\frac{\partial \tau_{YX}}{\partial X}\right)+\left(\frac{\partial \sigma_Y}{\partial Z}\right)+\left(\frac{\partial \tau_{YZ}}{\partial Z}\right)=0 \tag{4.1.2}$$

$$\left(\frac{\partial \tau_{ZX}}{\partial X}\right)+\left(\frac{\partial \tau_{YZ}}{\partial Y}\right)+\left(\frac{\partial \sigma_Z}{\partial Z}\right)=0 \tag{4.1.3}$$

The laminate in the Pipes and Pagano model was loaded uniaxially in the x direction and stresses near the free edge y = $\pm$b were considered. Since load does not vary along x, $\frac{\partial \sigma_X}{\partial X}=0$. Thus from equation 4.1.1, interlaminar shear stress $\tau_{XZ}(z)$ is given by

$$\tau_{XZ}(z)=-\int_{-\frac{t}{2}}^{Z}\frac{\partial \tau_{XY}}{\partial Y}dZ \tag{4.1.4}$$

The in-plane shear τ_{XY} has a constant value given by Classical Lamination Plate Theory in the interior regions of the laminate. As y approaches $\pm$b, τ_{XY} must decrease to zero. In other words as y$\rightarrow$ $\pm$b, $\frac{\partial \tau_{XY}}{\partial Y}$ must increase. From equation 4.1.4 we can conclude that τ_{XZ} must increase from zero in the interior of the laminate to large value as y$\rightarrow$ $\pm$b. From equations 4.1.2 and 4.1.3, the other interlaminar stresses are

$$\tau_{YZ}(z)=-\int_{-\frac{t}{2}}^{Z}\frac{\partial \sigma_Y}{\partial Y}dZ \tag{4.1.5}$$

$$\sigma_Z(z)=-\int_{-\frac{t}{2}}^{Z}\frac{\partial \tau_{YZ}}{\partial Y}dZ \tag{4.1.6}$$

Pipes and Pagano [51] used a finite difference numerical scheme to solve the three governing equations. The distribution of in-plane and interlaminar stress in a ± 45 degree laminate by Pipes and Pagano's elasticity solution is shown in Fig. 4.1.2. As explained earlier τ_{xy} is expected to decay to zero near the free edge of the laminate while τ_{xz} is expected to progressively increase near the same edge. Both these stresses were calculated along the interfaces of +45/-45 degree lamina.

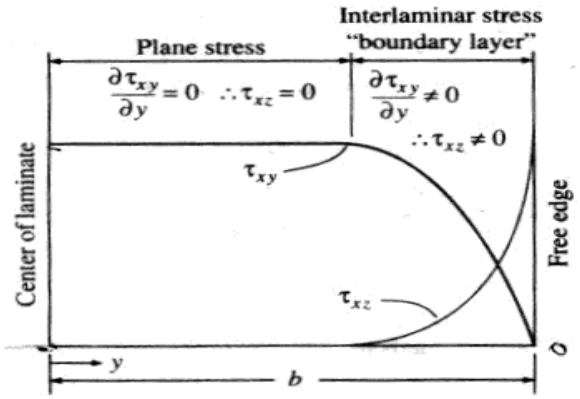

Fig.4.1.2 Distribution of stress in free edge region by elasticity method [51]

4.2. Finite Element Comparison

Analytical results obtained by Pipes and Pagano [51] were compared with the 3D FEA solution. The model introduced in chapter 2 was for a composite plate with a hole in it. However, the analytical results derived by Pipes and Pagano were for an un-notched composite plate. Hence, the hole in the geometry of the 3D model was eliminated to obtain an un-notched geometry for FE analysis. In order to maintain consistency in the coordinate system used in chapter 2, the coordinate system of the unnotched laminated plate was not altered. It should thus be kept in mind that the X axis of the analytical solution used by Pipes and Pagano corresponds to Y axis of the 3D model. The interlaminar stresses were determined by FEA for the $[45/-45/45/-45]_s$

laminate using the properties of T600/125-33 material given in Table 2.3.1. Fig.4.2.1 shows the geometry used for comparing the FEA results with the analytical results in Fig.4.1.2 [51]. The dimensions of the FE model of chapter 2 were retained for this analysis. Fig.4.2.1 also shows the BCs used for the un-notched FE model. Symmetry was used along the three mutually perpendicular faces of the model. Since the comparison was for the $[45/-45/45/-45]_s$ lay-up, only 4 layers were included in the FE. The width (b) of the model was 0.75 in, height was limited to 1.25 in and the thickness (h) of the 4 laminae was 0.0175 in. Solid 64 brick element was used. The model was subjected to a tensile stress (P) of 30,000 psi along y-direction.

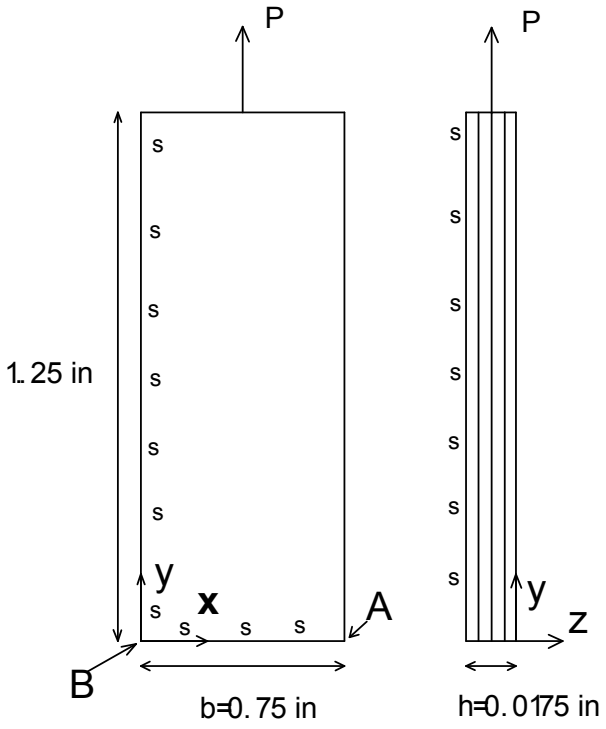

Fig.4.2.1 Geometry and BCs used for FEA of un-notched $[45/-45/45/-45]_s$ laminate.

The in-plane stress τ_{XY} and interlaminar shear stress τ_{XZ} were plotted with respect to distance from free edge as shown in Fig.4.2.2. The coordinate system followed for the plots in Fig. 4.2.2

is shown in Fig. 4.2.1. Free edge is denoted by point A in Fig. 4.2.1 and B denotes a point at the plane of symmetry. Both A and B lie at the interface of +45 degree and -45 degree lamina. The region near the free edge where the change in stress field was appreciably higher is the boundary layer. This region was approximately twice the thickness of laminate. The results from Fig. 4.2.2 were compared with the stress distribution in Fig.4.1.2. FEM results confirmed the predictions of Pipes and Pigano that as one moves closer to the free edges of a laminated composite, the in-plane shear decreases rapidly and the interlaminar shear stress simultaneously increases. In Fig.4.2.2 y/b = 0 represents the free edge and y/b=1 represents the plane of symmetry.

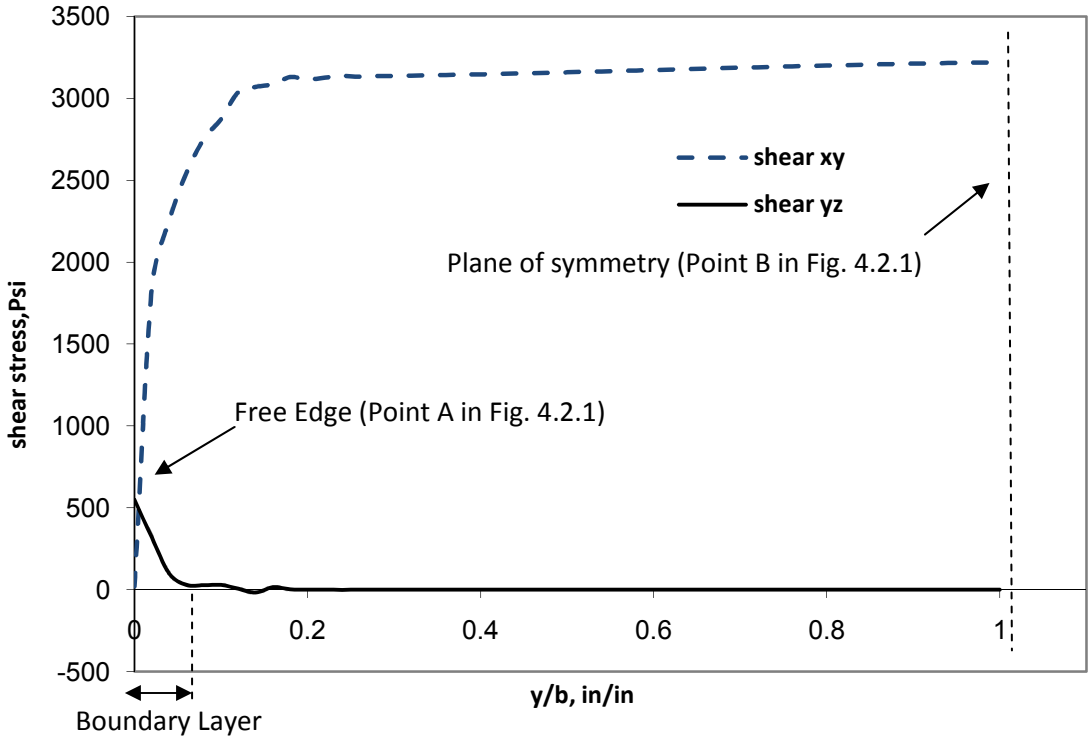

Fig.4.2.2 Distribution of stresses in the free edge region by FEM for $[+45^0/-45^0/+45^0/-45^0]_s$

Pipes and Pagano [52] also considered the $[+15^0/-15^0/+45^0/-45^0]$s laminate They kept the loading condition the same as that for $[+45^0/-45^0/+45^0/-45^0]_s$ which is shown in Fig.4.1.1. They used the elastic coefficients of Foye and Baker [53], namely,

$$E_L = 30\times10^6\,Psi\,,E_T = 2.15\times10^6\,Psi\,,G_{LT} = 0.68\times10^6\,Psi\,,\upsilon_{LT} = 0.19$$

where L is fiber direction, T is transverse direction and υ_{LT} is the major Poisson's ratio.

Placing $\pm 15^0$ on the outside they observed that for b/h > 10 the interlaminar stress (σ_Z) resembled the plot shown in Fig. 4.2.3. For small ratios the authors [2] predicted a steep gradient near the free edge with infinite stress value at $y/b = \pm 1$.

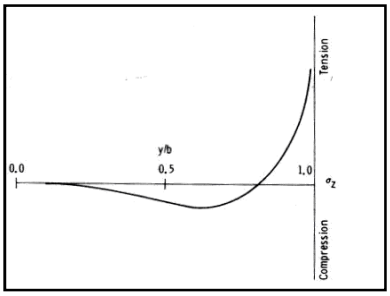

Fig.4.2.3 Predicted variation of interlaminar normal stress field along y [52]

The stress field was compared with the FEM solution which was obtained by replacing the $[+45^0/-45^0/+45^0/-45^0]$s orientation by $[+15^0/-15^0/+45^0/-45^0]$s. Interlaminar normal stress between $+15^0/-15^0$ interface was plotted as a function of x/b (y axis of Pipes and Pagano corresponds to x of FE solution) for two b/h ratios. In Fig.4.2.4, x/b = 0 symbolizes the free edge and x/b=1 is the plane of symmetry.

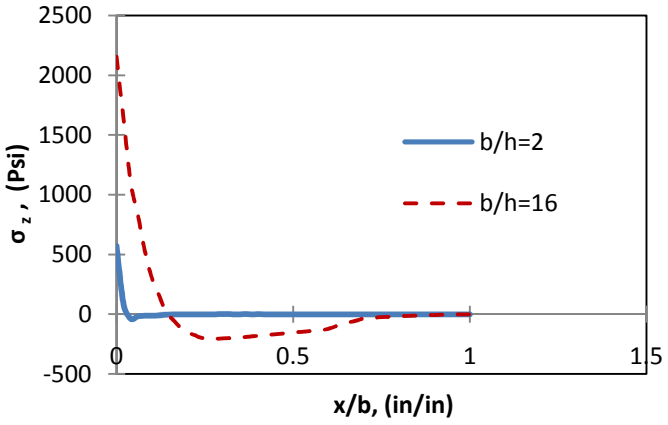

Fig.4.2.4 Variation of interlaminar normal stress along x for 2 different b/h ratios

4.3 Notch Effect:

As shown in the preceding sections, analytical work has been done in the area of the free edge effect and delamination occurring in un-notched laminates. The FE model results agreed well with the analytical model predictions. However the main focus of this thesis was to estimate the effect of notches on interlaminar stresses and ultimately delamination. It has been found that the presence of discontinuities such as holes, ply drops and joints results in higher interlaminar stresses and thus increases the probability of delamination [54].

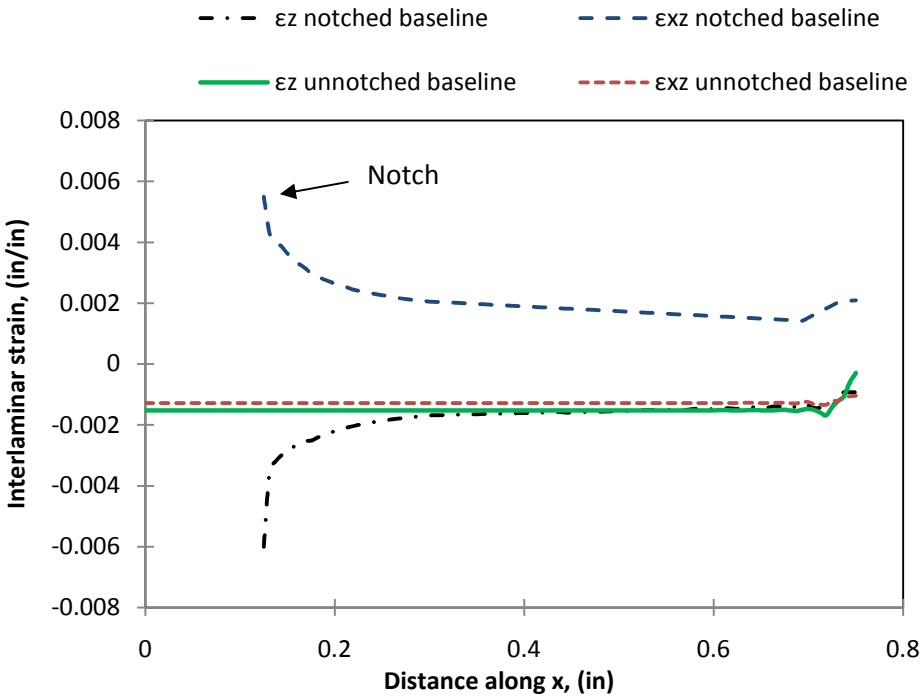

Fig.4.3.1 Interlaminar strain comparison between notched and un-notched coupon.

Fig.4.3.1. provides a comparison of the interlaminar strain between the notched and unnotched baseline laminate. The interface between ($0^0/45^0$) lamina was considered in this case. Both plates were of the same half width b. The presence of high out-of-plane shear and normal stresses near the hole clearly indicates the sensitivity of interlaminar stress to the presence of any notch in the body.

4.4 Results

Delamination is an initiation and growth process. After initiation, the delamination can undergo stable growth. Eventually due to unstable growth and interaction with in-plane failure modes, the final fracture occurs [55]. There are two basic approaches to predict delamination in laminates. Some use a mechanics of materials approach. Using strength parameters the local state of stress in the nterplay matrix layer where delamination occurs is found [56]. Others have used fracture mechanics techniques. The most common approach involves the strain energy release rate. O'Brian [57] derived a single equation for the calculation of the total strain energy released per unit delaminated area along a straight edge:

$$G = \frac{t \times \varepsilon^2}{2}\left(E_{LAM} - E_W\right) \tag{4.4.1}$$

where G is the strain energy release rate or energy per unit delaminated area, t is the laminate thickness, ε is the longitudinal strain level, E_{LAM} is the longitudinal modulus of the un-delaminated laminate and E_W is the weighted average longitudinal modulus of the sub laminate remaining after delamination.

O'Brian has shown that critical values of the strain energy release rate are in fact laminate dependent and has suggested that critical strain energy release rate (G_c) is a function of the percentage of the total strain energy release rate that can be attributed to mode I. However for the current work a mechanics of materials approach. The reason being that in composites a large number of failure modes co-exist and thus a fracture based approach would not be able to provide an accurate solution. Quadratic Delamination Criterion is based on mechanics of materials.

4.4.1 Quadratic Delamination Criterion

Brewer and Lagace [55] proposed the Quadratic delamination criterion which can be written as

$$\left(\frac{\sigma_{13}}{S_{13}}\right)^2+\left(\frac{\sigma_{23}}{S_{23}}\right)^2+\left(\frac{\sigma_{3T}}{S_{3T}}\,or\,\frac{\sigma_{3C}}{S_{3C}}\right)^2=1 \tag{4.4.2}$$

where σ_{13} and σ_{23} are interlaminar shear stresses, σ_{3T} and σ_{3C} are interlaminar tensile and compressive normal stresses respectively, S_{13} and S_{23} are interlaminar shear strengths, S_{3T} and S_{3C} are interlaminar tensile and compressive strengths respectively.

Transverse isotropy was assumed, so that:

$$S_{3T}=S_{2T} \tag{4.4.3}$$

$$S_{3C}=S_{2C} \tag{4.4.4}$$

where S_{2T} and S_{2C} are ultimate transverse strengths in tension and compression.

The authors in [55] also observed that:

$$S_{13}=S_{23}=S_{12} \tag{4.4.5}$$

where S_{12} is the in plane shear strength as given in Table 2.3.1. Fig.4.3.1 shows that interlaminar stresses near notches are higher than the interior of laminates. So, quadratic delamination criterion was applied near the edge of hole and throughout the thickness of the FE model as shown in Fig.4.4.1. The delamination initiation stress (σ_D) is predicted by

$$\sigma_D=P/f.i \tag{4.4.6}$$

where P is the applied tensile stress and *f.i.* stands for the failure index and is equal to the left hand side of the equation 4.4.2 for a given P. Delamination initiation was expected at the

interface separating two lamina. So the quadratic failure criterion was applied to the nodes separating two layers.

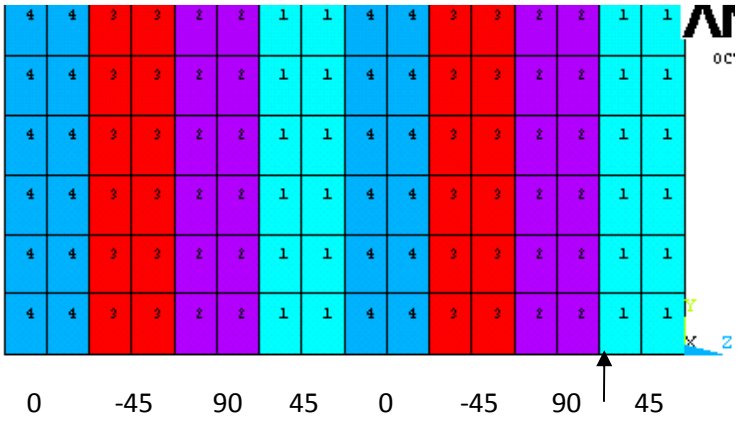

Fig.4.4.1 Edge of the hole near the point of maximum strain concentration.

Fig. 4.4.1 shows the elements of the 3D model stacked together through the thickness of the laminate near the edge of the hole. The numbers 1, 2, 3, 4 stand for the material layers of 45, 90, -45 and 0 respectively for a baseline laminate. The arrow points to the node which is shared by the 45 and 90 degree lamina and there are 7 such nodes shared by different lamina. These nodes were used to evaluate the quadratic delamination criterion using equations 4.4.6.

Table 4.4.1 Delamination initiation stress along with the interfaces delaminated.

Lay-up	FPF using Max-Strain (Ksi)	Delamination stress (Ksi)	DICM UTS(Ksi)	Interface delaminated
BL	9.69	50.42	71	(-45/90)
A	9.18	85.47	73	N/A
B	16.12	73.89	73	N/A
C	11.30	66.67	69	(0/-45)
D	6.23	16.40	29	(45/90)
E	17.02	303	68	N/A
F	9.23	87	73	N/A
G	13.3	15.79	91	(-21/90)
H	23	202.70	100	N/A

Table 4.4.1 provides a comparison of the delamination initiation stress of the lay-ups with their corresponding FPF and UTS. The lamina interfaces that showed the highest failure ratio were assumed to delaminate first.

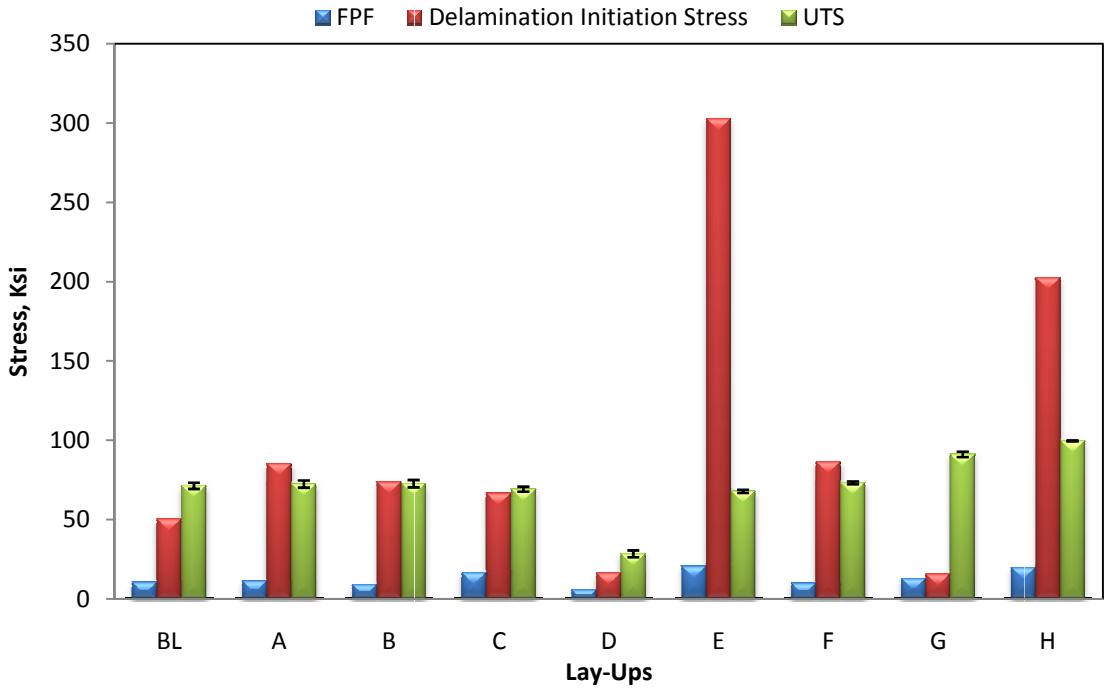

Fig.4.4.2 Comparison between FPF, UTS and Delamination initiation stress of different lay-ups

Fig.4.4.2 shows the comparison between the delamination initiation stress of different lay-ups with the FPF strength calculated by the max-strain theory of 3D model and the ultimate tensile strength (UTS). The laminates designated as BL, C, D and G show delamination initiation at 71%, 96%, 57% and 17% of the UTS respectively. Laminates A, B, F and H have delamination initiation stress higher than UTS which indicates that these laminates should not delaminate at all. Laminate D and G have a delamination initiation stress very close to the first ply failure.

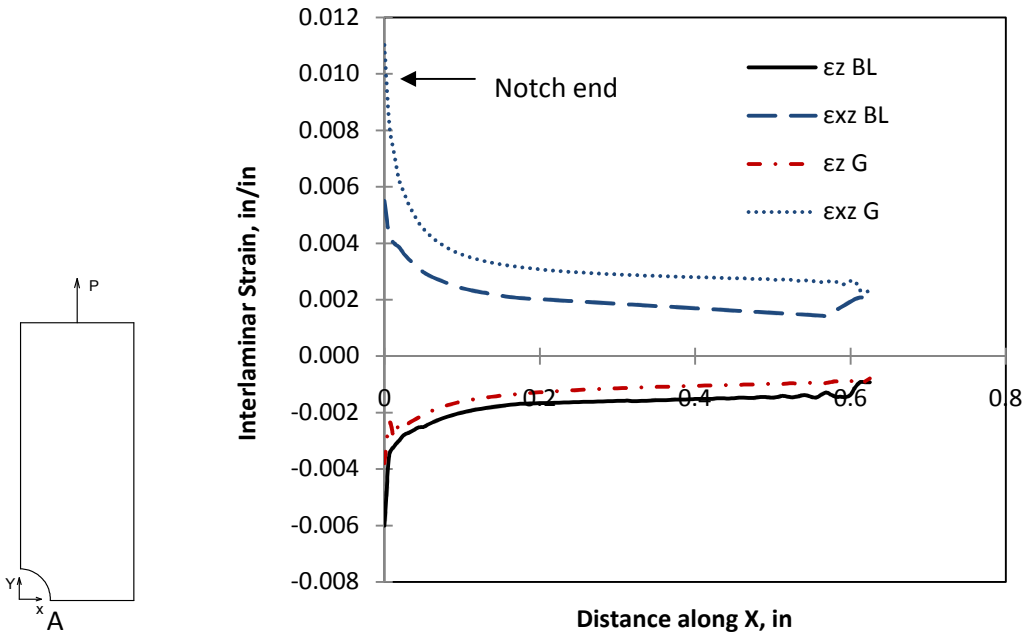

Fig.4.4.3 Comparison of interlaminar strains between Baseline and G laminate

Fig.4.4.3 compares the interlaminar strains between the [$-45^0/90^0$] interface of the baseline and the [$-21^0/90^0$] interface of the G laminate. FE models of both the laminates were subjected to a uniaxial tensile stress of 30000 Psi. As shown in Table 4.4.1, delamination was expected to initiate along these interfaces in these two laminates. The Baseline was chosen as a reference laminate and the G laminate was chosen as it showed the lowest delamination initiation stress. This made the G laminate prone to delamination. From Fig.4.4.3 it can be observed that G laminate experienced a lower interlaminar normal compressive stress and a higher interlaminar shear stress than the Baseline laminate. Interlaminar shear is always harmful for the delamination strength of the laminated composite. On the other hand normal compressive stress increases the resistance of the laminate against delamination failure. Keeping this in mind one can explain the lower delamination strength of the G laminate than the Baseline.

The accuracy of the predictions of the quadratic failure criterion was provided by SEM images. Laminates BL, C, D and G were loaded up to the delamination initiation stress and examined using SEM. Due to some damage while preparing the sample for SEM the images of laminates C and D couldn't be examined

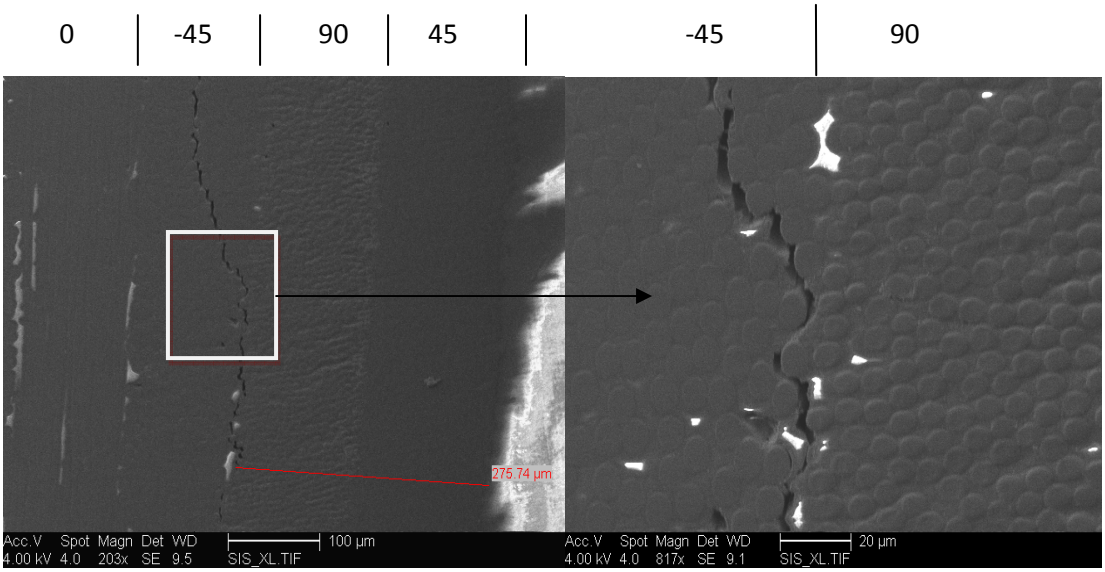

Fig.4.4.4 Crack between the -45/90 degree interface of baseline laminate

Fig. 4.4.4 shows a hairline crack at the interface of -45 and 90 degree laminae. The right hand side of the image shows a section of the crack where it can be seen to propagate into the -45 degree lamina. However, it is quite difficult to determine if the delamination initiation at the -45/90 interface occurred first and then led to the crack propagation inside the -45 degree lamina or vice versa. The Quadratic delamination criterion for this research was based on linear elastic FE model. If delamination in a laminate occurs after the FPF, the accuracy of the predicted stress at which delamination initiation takes place would decrease. In such situation the qualitative results should be used to compare the relative response of laminates to Delamination. The Baseline laminate is one such example where delamination is supposed to set in at 71% of UTS.

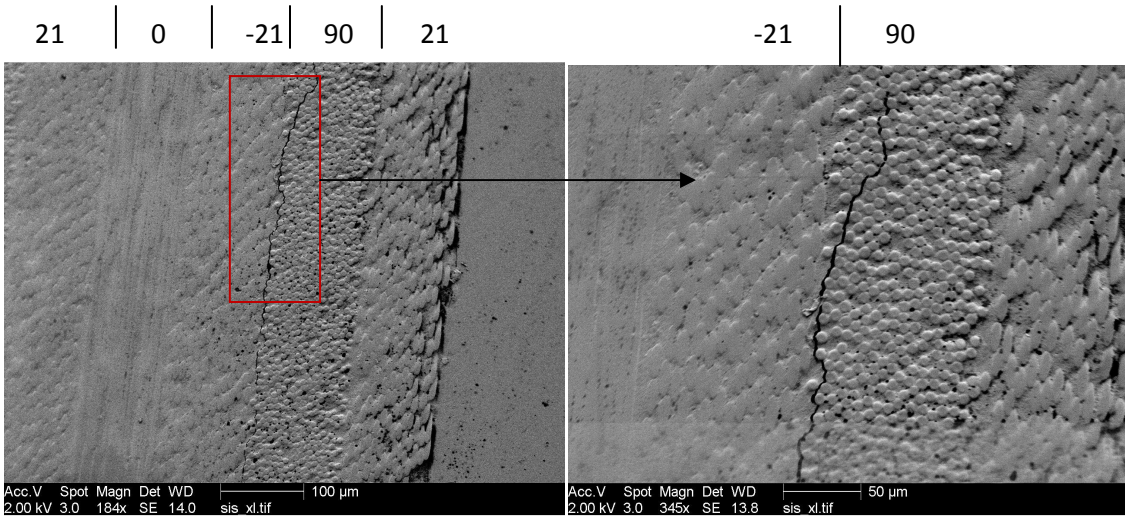

Fig.4.4.5 Crack between the -21/90 degree interface in baseline laminate.

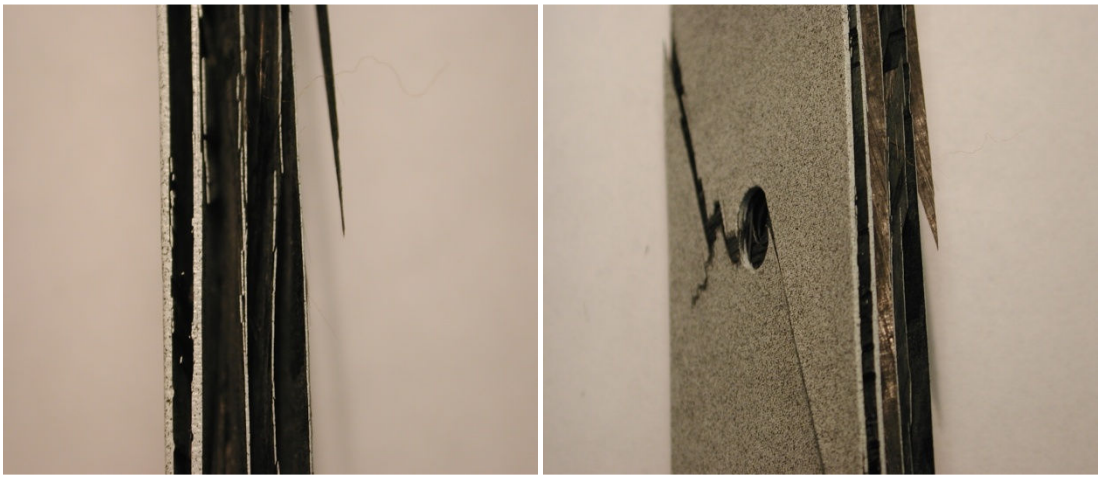

Fig.4.4.6 G laminate at ultimate load

Fig.4.4.5 shows a crack between the -21 and 90 degree layers of the G laminate when the laminate was subjected to a delamination initiation stress of 15.79 Ksi. In the right hand side image of Fig.4.4.5 it can be seen that the crack propagated through the -21/90 interface and then entered the 90 degree lamina. Fig.4.4.6 shows the ultimate failure mode of G laminate. The final failure was due to delamination resulting in separation of the individual laminae. This result

confirms that the delamination initiation stress of the G laminate was very close to the FPF. The onset of delamination at such an early stage resulted into a catastrophic failure.

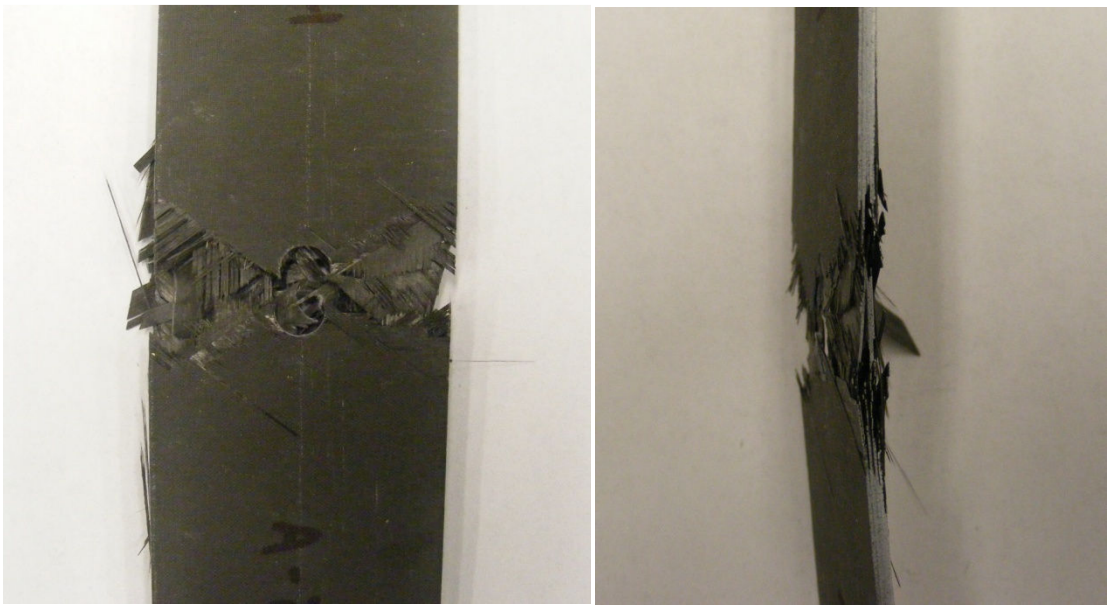

Fig.4.4.7 Laminate A at ultimate load

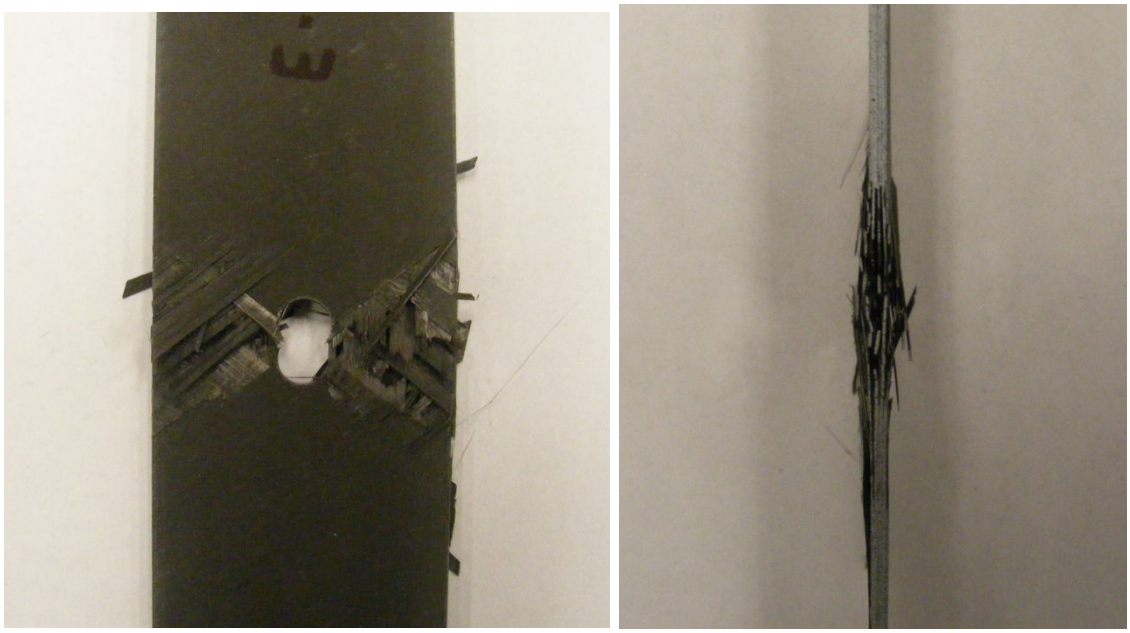

Fig.4.4.8 Laminate E at ultimate load

Fig.4.4.7 shows the front view and the side view of the laminate A (Vary 45) when subjected to ultimate tensile stress of 73 Ksi. Fig.4.4.8 shows the front and the side view of laminate E (vary 45 & 90) when subjected to an ultimate tensile stress of 68 Ksi. According to Fig.4.4.2 quadratic delamination criterion predicted the delamination strength of both laminates A and E higher than their corresponding UTS. This result was used qualitatively to suggest that these laminates won't delaminate. By comparing Fig.4.4.6, Fig.4.4.7 and Fig.4.4.8 it can be clearly seen that unlike G laminate, laminates A and E didn't fail in delamination. This validates the methodology of estimating the response of a notched laminate to delamination failure.

4.5 Chapter Summary

The ability of a 3D model to capture free edge effects makes it an ideal tool for studying interlaminar stresses which may lead to delamination failure. For the current study, the linear elastic 3D model proposed for a composite plate with a circular notch was further used to predict delamination initiation stress. The laminates selected from the K_t and FPF optimization study were used as test samples. Sensitivity of interlaminar stresses to the presence of notch was shown which lead to the belief that the edge of the hole (the one perpendicular to the loading direction) should be prone to delamination failure if any. Quadratic delamination criterion was selected that allowed to compare the relative response of laminates to delamination. One particular laminate "G" was expected to show a final failure in form of delamination. SEM was used to validate the claim.

5. Computational Micromechanics

5.1 Introduction

Stress and deformation analysis of fiber reinforced composites is carried out at different levels. The detail necessary for the description of composite material depends on the level of post processing desired. Fiber reinforced composites can be studied as homogenous or heterogeneous bodies. When treated as homogenous, fiber and matrix are not considered separate and effective elastic properties like Young's Modulus (E), shear modulus (G) and Poisson's Ratio (υ) of the whole lamina are used for numerical analysis. To determine the effective properties (as shown in Table 2.3.1) of the lamina, experimental procedures similar to the one described in section 2.3 are used. Treating composites as heterogeneous media is a rather tedious and expensive process and in most cases homogenous models provide sufficient information to tackle design problems. However, by using heterogeneous models and the elastic properties of the constituent fibers and matrix, the homogenous properties of the lamina can be determined. This is intended to replace the experimental procedure for achieving the same results. The process of using the microstructure to determine the homogenous properties of the composite lamina is called micromechanics and the models proposed for this process are called micromechanical models. These models are classified as empirical, semi-empirical, analytical and numerical. This chapter is aimed implementing micromechanics as a FE based model. The model can be used to cross-check the elastic properties of a composite material system and also to visualize the effect of the applied strain state at the fiber and matrix level.

5.2 Numerical Homogenization

In most commercially fabricated composites, it is not possible to control the placement of fibers very precisely. Fig.5.2.1 shows the random distribution of fibers in the 90 degree lamina of the baseline laminate. The fiber diameter of T300 fibers in Fig.5.2.1 was found to be 6.95µm. For this work the fiber diameter was rounded off to 7µm.

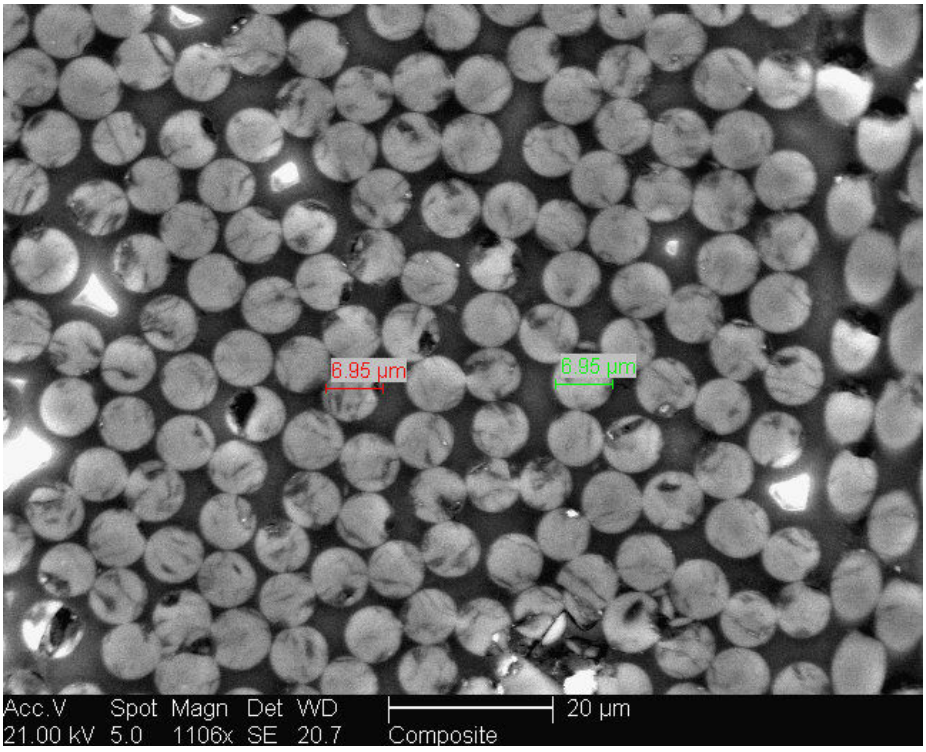

Fig.5.2.1 Random distribution of fibers in 90 degree lamina in baseline laminate

Some [58, 59] have documented that a random microstructure results in transverse isotropic behavior at the meso-scale and a hexagonal array of fibers has been found to simulate this behavior at the micro-level. This is important from the point of view of this study as the stiffness matrices for different laminae in equation 2.3.8 depicted transverse isotropic behavior. From Hook's law the transverse isotropic stiffness tensor © can be obtained given by

$$\begin{Bmatrix} \bar{\sigma}_1 \\ \bar{\sigma}_2 \\ \bar{\sigma}_3 \\ \bar{\sigma}_4 \\ \bar{\sigma}_5 \\ \bar{\sigma}_6 \end{Bmatrix} = \begin{bmatrix} C_{11} & C_{12} & C_{12} & 0 & 0 & 0 \\ C_{12} & C_{22} & C_{23} & 0 & 0 & 0 \\ C_{12} & C_{23} & C_{22} & 0 & 0 & 0 \\ 0 & 0 & 0 & \frac{(C_{22}-C_{23})}{2} & 0 & 0 \\ 0 & 0 & 0 & 0 & C_{66} & 0 \\ 0 & 0 & 0 & 0 & 0 & C_{66} \end{bmatrix} \begin{Bmatrix} \bar{\varepsilon}_1 \\ \bar{\varepsilon}_2 \\ \bar{\varepsilon}_3 \\ \bar{\gamma}_4 \\ \bar{\gamma}_5 \\ \bar{\gamma}_6 \end{Bmatrix} \tag{5.2.1}$$

The subscripts 1, 2, 3 are the normal and 4, 5, 6 are the shear components of stress and strain with tensor strains $\bar{\gamma}_4 = 2\bar{\varepsilon}_{23}$, $\bar{\gamma}_5 = 2\bar{\varepsilon}_{13}$ and $\bar{\gamma}_6 = 2\bar{\varepsilon}_{12}$. The over bar denotes that average of the terms is computed over the volume of a representative volume element (RVE). For this study the RVE is a section of the hexagonal array which represents the behavior of the whole cell. Fig. 5.2.2 shows a hexagonal array of fibers embedded in matrix. Fig. 5.2.2 also shows a section of the hexagonal array which formed the RVE for the current study.

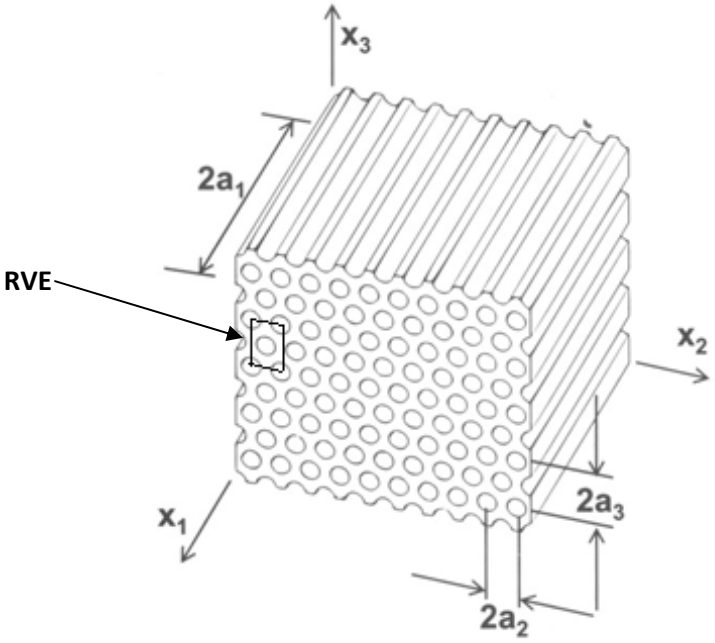

Fig.5.2.2 Composite material with a hexagonal array of fibers [58]

The RVE based FE model was used to determine the components of the stiffness tensor © of the equation 5.2.1. The elastic properties of the homogenized material were then determined using the following relations [58]

$$E_1 = C_{11} - \frac{2C_{12}^{\ 2}}{C_{22} + C_{23}} \tag{5.2.2}$$

$$E_2 = \frac{\left[C_{11}\left(C_{22} + C_{23}\right) - 2C_{12}^{\ 2}\right]\left(C_{22} - C_{23}\right)}{C_{11}C_{22} - C_{12}^{\ 2}} \tag{5.2.3}$$

$$\nu_{12} = \frac{C_{12}}{\left(C_{22} + C_{23}\right)} \tag{5.2.4}$$

$$\nu_{23} = \frac{\left(C_{11}C_{23} - C_{12}^{\ 2}\right)}{\left(C_{11}C_{22} - C_{12}^{\ 2}\right)} \tag{5.2.5}$$

$$G_{12} = C_{66} \tag{5.2.6}$$

where E_1 and E_2 are the longitudinal and transverse Young's moduli, ν_{12} and ν_{23} are the longitudinal and transverse Poisson's ratios and G_{12} is the longitudinal shear modulus of the composite lamina. Since the body is transversely isotropic, therefore

$$E_3 = E_2 \tag{5.2.7}$$

$$\nu_{12} = \nu_{13} \tag{5.2.8}$$

$$G_{12} = G_{13} \tag{5.2.9}$$

$$\text{and } G_{23} = \frac{E_2}{2\left(1 + \nu_{23}\right)} \tag{5.2.10}$$

5.3 RVE Geometry

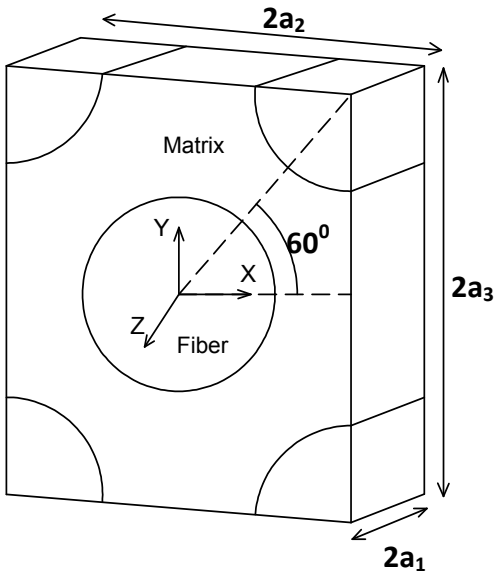

Fig. 5.3.1 Geometry of RVE

The Fiber volume fraction (ν_f) is defined as the ratio of the volume of fibers to the volume of composite. The dimensions a_1, a_2 and a_3 of the RVE were chosen to obtain a particular fiber volume fraction with a hexagonal array. For the RVE in Fig. 5.3.1 with a fiber diameter d_f, the volume of fibers is

$$V_f = 2\left(\frac{\pi}{4} d_f^{\,2}\right) 2a_1 \tag{5.3.1}$$

$$= a_1 \pi d_f^{\,2} \tag{5.3.2}$$

The unit cell volume, V_c is

$$V_c = 2a_1 2a_2 2a_3 \tag{5.3.3}$$

$$= 8a_1 a_2 a_3 \tag{5.3.4}$$

From which the fiber volume fraction can be found as

$$\nu_f = \frac{V_f}{V_c} = \frac{\pi d_f^{\,2}}{8a_2 a_3} \tag{5.3.5}$$

For most of the commercially available composites, a fiber volume fraction of 0.65 is used. Therefore, equation 5.3.5 can be rewritten as

$$\frac{\pi d_f^{\,2}}{8a_2a_3} = 0.65 \tag{5.3.6}$$

From Fig. 5.3.1 the relationship between a_2 and a_3 can be established as

$$a_3 = a_2 \tan 60^0 \tag{5.3.7}$$

The dimension a_1 is chosen arbitrarily. For the current study

$$a_1 = \frac{a_2}{4} \tag{5.3.8}$$

Using equations 5.2.6, 5.3.7 and 5.3.8 and assuming a fiber diameter of 7μm we get $a_1 = 1.033\mu m$, $a_2 = 4.134\mu m$ and $a_3 = 7.16\mu m$. These dimensions were used to generate the geometry of the RVE.

5.4 Material Properties

The elastic properties of the constituent fiber and matrix of T600:125-33 were unavailable. From the literature [34] it was clear that both T300:934 and T600:125-33 had almost identical homogenized elastic properties. For the RVE model the elastic properties of the constituent fibers and matrix of T300:934 (Table 5.4.1) instead of T600:125-33 composite material were used.

Table 5.4.1 Elastic properties of constituent fibers and matrix of T300:934 composite material

Fiber		
$E_{f1} = 32.0\times10^6\,Psi$	$E_{f2} = 2.0\times10^6\,Psi$, $E_{f3} = E_{f2}$	$G_{f12} = 1.3\times10^6\,Psi$, $G_{f13} = G_{f12}$
$G_{f23} = 0.7\times10^6\,Psi$	$\upsilon_{f12} = 0.20$	$\upsilon_{f23} = 0.25$, $\upsilon_{f13} = \upsilon_{f12}$
Matrix		
$E_m = 0.5\times10^6\,Psi$	$G_m = \frac{E_m}{2(1+\upsilon_m)} = 0.185\times10^6\,Psi$	$\upsilon_m = 0.35$

5.5 Boundary Conditions

As stated earlier, the primary objective of the RVE model is to predict homogenized elastic properties of a lamina. Equations (5.2.2-5.2.10) established a relation between the elastic properties of a homogenous composite material and the terms of stiffness matrix. FE based RVE model first evaluates the terms of stiffness matrix. From equation 5.2.1 it is clear that the stiffness matrix can be defined in terms of stresses if the volume average strains $\bar{\varepsilon}_{ij}$ in the RVE are predefined. That means that if $\bar{\varepsilon}_1 = 1$ and $\bar{\varepsilon}_2 = \bar{\varepsilon}_3 = \bar{\gamma}_4 = \bar{\gamma}_5 = \bar{\gamma}_6 = 0$ in equation 5.2.1 then $C_{11} = \bar{\sigma}_1, C_{12} = \bar{\sigma}_2$. Similarly other terms can be evaluated. However volume average strain is not the parameter that the user can control. Instead we can use applied strain $\varepsilon_{ij}^{\,0}$ to induce a desired volume averaged strain $\bar{\varepsilon}_{ij}$ in the RVE. This follows from the relation between the volume averaged strain and the applied strain as [58]

$$\bar{\varepsilon}_{ij} = \frac{1}{V}\int_V \varepsilon_{ij} dv = \varepsilon_{ij}^{\,0} \tag{5.5.1}$$

In the RVE six components of strain $\left(\varepsilon_{ij}^{\,0}\right)$ use the following boundary conditions on the displacement components.

$$u_i(a_1, x, y) - u_i(-a_1, x, y) = 2a_1 \varepsilon_{i1}^{\,0} \quad \begin{bmatrix} -a_2 \le x \le a_2 \\ -a_3 \le y \le a_3 \end{bmatrix} \tag{5.5.2}$$

$$u_i(z, a_2, y) - u_i(z, -a_2, y) = 2a_2 \varepsilon_{i2}^{\,0} \quad \begin{bmatrix} -a_1 \le z \le a_1 \\ -a_3 \le y \le a_3 \end{bmatrix} \tag{5.5.3}$$

$$u_i(z, x, a_3) - u_i(z, x, -a_3) = 2a_3 \varepsilon_{i3}^{\,0} \quad \begin{bmatrix} -a_1 \le z \le a_1 \\ -a_2 \le x \le a_2 \end{bmatrix} \tag{5.5.4}$$

where $i, j = 1..3$ and the superscript $(\,)^0$ indicates the applied strain. The left hand of the equations (5.5.2-5.5.4) indicates the relative displacement between the two opposite faces of the RVE including edges and vertices. Furthermore, $2a_j\varepsilon_{ij}^{\,0}$ is the displacement necessary to enforce the strain $\varepsilon_{ij}^{\,0}$ over a distance $2a_j$. Fig. 5.5.1 is a representation of the RVE block without the distinction between fiber and matrix components. It shows the coordinates of the sides of the RVE and acts as a visual aid in understanding the application of BCs using the equations (5.5.2-5.5.4). As shown in the Fig. 5.5.1 Z represents the 1 (fiber direction) and X and Y represent 2 and 3 directions respectively.

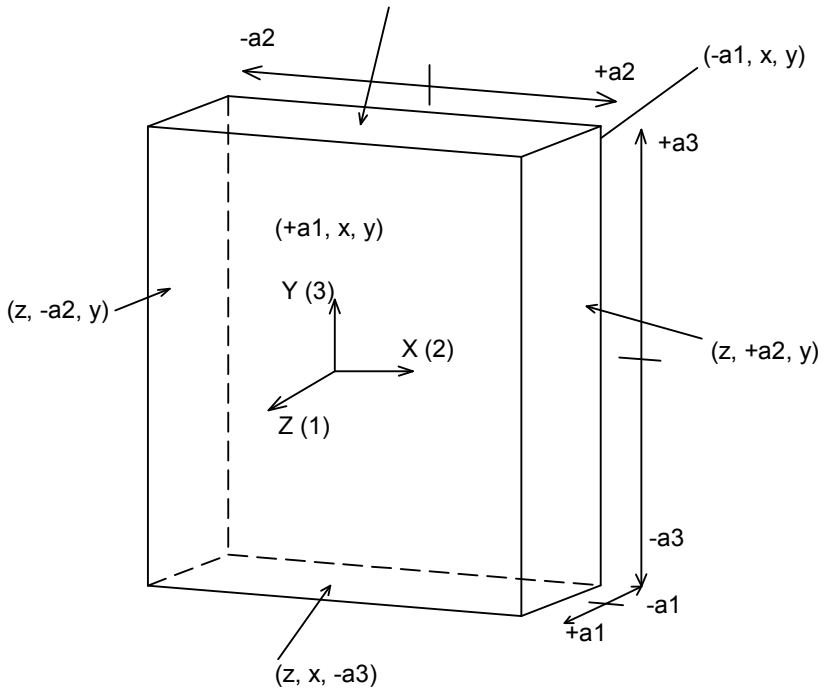

Fig. 5.5.1 Co-ordinates of six faces on the RVE block

To determine the coefficients of stiffness matrix, the boundary conditions 5.2.2-5.2.4 were applied on the RVE in three stages. Each stage exposed the RVE to a particular boundary condition. This three stage condition is true for a transversely isotropic body. This is because in three stages all the necessary coefficients of stiffness matrix are obtained which are necessary to

find the elastic properties of the composite material. The coefficients of the stiffness matrix in equation 5.2.1 were evaluated column wise. The procedure of evaluating the stiffness coefficients in each of the six columns is explained in following steps.

First Column

To determine components in the first column of equation 5.2.1, following strain was applied to the RVE in fiber direction (Z-direction).

$$\varepsilon_1^{\,0} = 1 \text{ and } \varepsilon_2^{\,0} = \varepsilon_3^{\,0} = \gamma_4^{\,0} = \gamma_5^{\,0} = \gamma_6^{\,0} = 0 \tag{5.5.5}$$

Equation 5.5.5 can be applied in terms of terms of DOF as

$$\left.\begin{cases} u_1(a_1, x, y) - u_1(-a_1, x, y) = 2a_1 \\ u_2(a_1, x, y) - u_2(-a_1, x, y) = 0 \\ u_3(a_1, x, y) - u_3(-a_1, x, y) = 0 \end{cases}\right\} -a_3 \le y \le a_3, -a_2 \le x \le a_2 \tag{5.5.6}$$

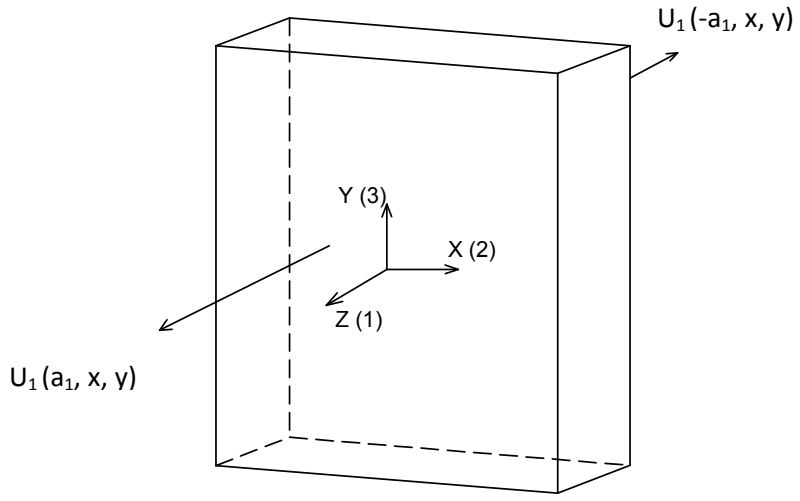

Fig. 5.5.2 Displacement BC on faces (a_1, x, y) and ($-a_1$, x, y)

As shown in Fig. 5.5.2 unit strain is applied between the faces (a_1, x, y) and ($-a_1$, x, y) of the RVE in Z direction (1 direction) while the relative X, Y DOF between the two faces have been

constrained to prevent rigid body rotation. From equation 5.5.6 the displacement necessary to cause this strain in fiber direction is $2a_1$. The FE model generates the first set of stiffness coefficients as[7]

$$C_{11} = \bar{\sigma}_1 = \bar{\sigma}_z \tag{5.5.7}$$

$$C_{12} = \bar{\sigma}_2 = \bar{\sigma}_x \tag{5.5.8}$$

Second Column

For the second column of the stiffness matrix of equation 5.2.1

$$\varepsilon_2^0 = 1 \text{ and } \varepsilon_1^0 = \varepsilon_3^0 = \gamma_4^0 = \gamma_5^0 = \gamma_6^0 = 0 \tag{5.5.9}$$

Equation 5.5.9 can be applied in terms of terms of DOF as

$$\left.\begin{cases} u_1(z,a_2,y) - u_1(z,-a_2,y) = 0 \\ u_2(z,a_2,y) - u_2(z,-a_2,y) = 2a_2 \\ u_3(z,a_2,y) - u_3(z,-a_2,y) = 0 \end{cases}\right\} -a_1 \le z \le a_1 \ , \ -a_3 \le y \le a_3 \tag{5.5.10}$$

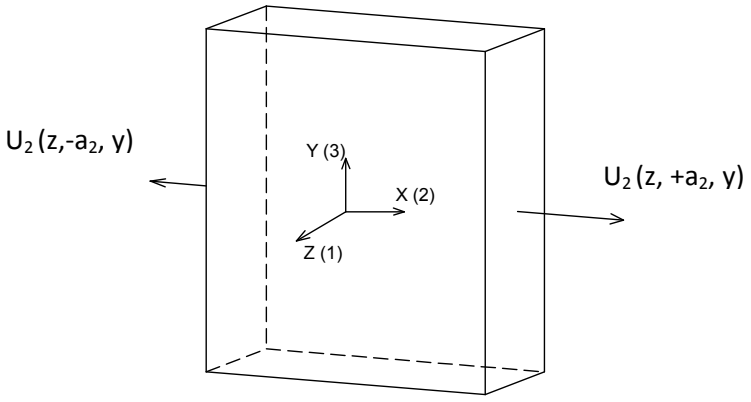

Fig.5.5.3 Displacement BC on faces $(z,-a_2, y)$ and $(z, +a_2, y)$

[7] ANSYS™ 10.0 program used for generating the volume averaged stresses for the RVE has been be explained in sec.5.6.

As shown in Fig. 5.5.3 unit strain is applied between the faces (z, -a_2, y) and (z, +a_2, y) of the RVE. From equation 5.5.10 the displacement necessary to cause this strain in X direction is $2a_2$. The stiffness coefficient that is needed from this column is

$$C_{22} = \bar{\sigma}_2 = \bar{\sigma}_x \tag{5.5.11}$$

$$C_{23} = \bar{\sigma}_3 = \bar{\sigma}_y \tag{5.5.12}$$

Third Column

From equation 5.2.1, all three stiffness matrix coefficients have been obtained from first and second column. Thus there is no need to evaluate any term from this column.

Fourth Column

From equation 5.2.1 it is evident that in the fourth column of the stiffness matrix only one non-zero term (C_{44}) exists which can be evaluated as

$$C_{44} = \frac{1}{2}\left(C_{22} - C_{33}\right) \tag{5.5.16}$$

Fifth Column

Again from equation 5.2.1 it is clear that only term C_{55} is non-zero. Also, relationship between C_{55} and C_{66} for transversely isotropic material is

$$C_{55} = C_{66} \tag{5.5.17}$$

Sixth Column

In order to evaluate C_{66} in the sixth and last column of the stiffness matrix the following relation should be satisfied

$$\gamma_6^{\,0} = 1 \text{ and } \varepsilon_1^{\,0} = \varepsilon_2^{\,0} = \varepsilon_2^{\,0} = \gamma_4^{\,0} = \gamma_5^{\,0} = 0 \tag{5.5.18}$$

$$\text{But } \gamma_6^{\,0} = \varepsilon_{12}^{\,0} + \varepsilon_{21}^{\,0} = 1 \tag{5.5.19}$$

$$\textit{and } \varepsilon_{12}^{\,0} = \varepsilon_{21}^{\,0} \tag{5.5.20}$$

From 5.5.19 and 5.5.20 it implies that $\varepsilon_{21}^{\,0} = \frac{1}{2}$ should be applied between faces (-a_1, x, y) and (a_1, x, y) and other half should be applied between (z, a_2, y) and (z, -a_2, y). This can be simply understood from the equation 5.5.2 and equation 5.5.3 in which i takes values from 1..3. In equation 5.5.2 when $\varepsilon_{21}^{\,0} = \frac{1}{2}$ is applied while keeping $\varepsilon_{11}^{\,0} = \varepsilon_{31}^{\,0} = 0$ we get

$$\left.\begin{cases} u_1(a_1,x,y) - u_1(-a_1,x,y) = 0 \\ u_2(a_1,x,y) - u_2(-a_1,x,y) = a_1 \\ u_3(a_1,x,y) - u_3(-a_1,x,y) = 0 \end{cases}\right\} -a_2 \le x \le a_2 \ , \ -a_3 \le y \le a_3 \tag{5.5.21}$$

Similarly, using equation 5.5.3 the other half of the in-plane shear $\varepsilon_{12}^{\,0} = \frac{1}{2}$ is applied between faces (z, a_2, y) and (z, -a_2, y) while keeping $\varepsilon_{22}^{\,0} = \varepsilon_{32}^{\,0} = 0$ we get

$$\left.\begin{cases} u_1(a_1,x,y) - u_1(-a_1,x,y) = a_2 \\ u_2(a_1,x,y) - u_2(-a_1,x,y) = 0 \\ u_3(a_1,x,y) - u_3(-a_1,x,y) = 0 \end{cases}\right\} -a_1 \le x \le a_1 \ , \ -a_3 \le y \le a_3 \tag{5.5.22}$$

The net effect of equations 5.5.21 and 5.5.22 is shown in Fig. 5.5.5. The FE model under boundary conditions 5.5.21 and 5.5.22 resulted in pure in-plane shear and provided C_{66} as

$$C_{66} = \bar{\sigma}_6 = \bar{\sigma}_{xz} \tag{5.5.23}$$

Fig. 5.5.5 shows the faces over which the shear is applied. The top view of the RVE block in Fig. 5.5.5 shows the shear effect in 12 plane.

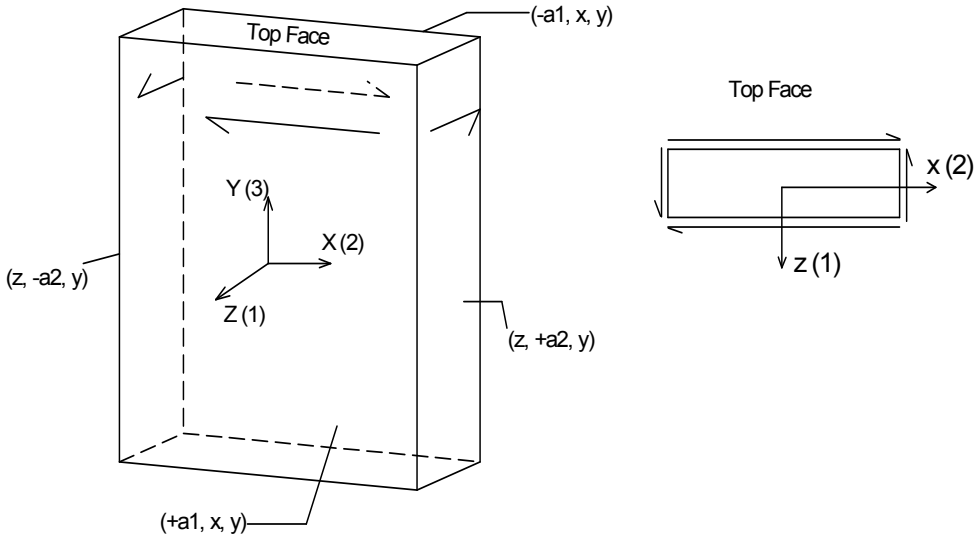

Fig. 5.5.4 Displacement BC on faces (+a_1, x, y) and (-a_1, x, y) and faces (z, -a_2, y) and (z, +a_2, y). Top face showing the shear effect in 12 plane.

5.6 FE Code Implementation

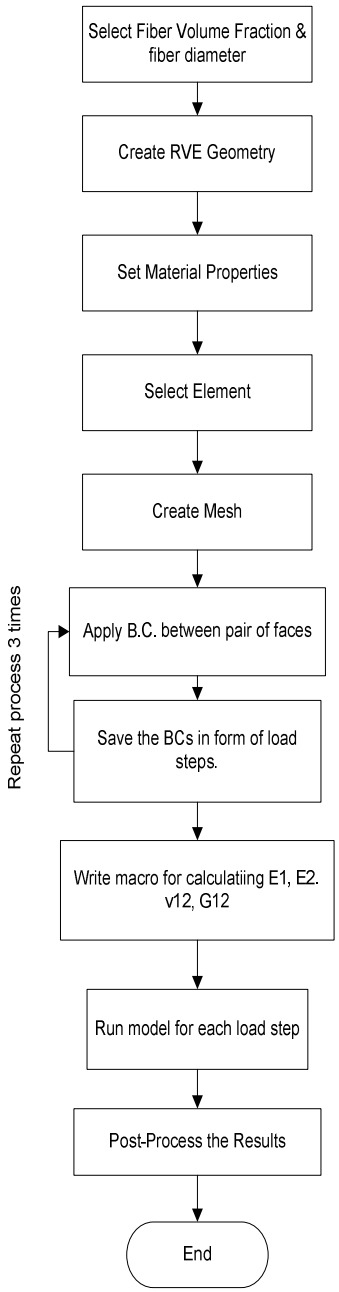

Fig.5.6.1 Flow chart for the RVE model

The flowchart in Fig. 5.6.1 lists the steps for proceeding with the Finite Element model of the RVE. First of all, the parameters - fiber volume fraction $\left(v_f\right)$ and fiber diameter $\left(d_f\right)$ were fixed. As explained in section 5.3 the RVE dimensions (a_1, a_2, a_3) were evaluated using v_f and

d_f. Ansys^{TM} 10.0 FEA package was used for the numerical modeling of the RVE. Using a_1, a_2, a_3 and d_f, the geometry of the RVE model was created. The material model parameters were set. As shown in Table 5.4.1 orthotropic properties were selected for the fiber and isotropic properties were selected for the matrix.

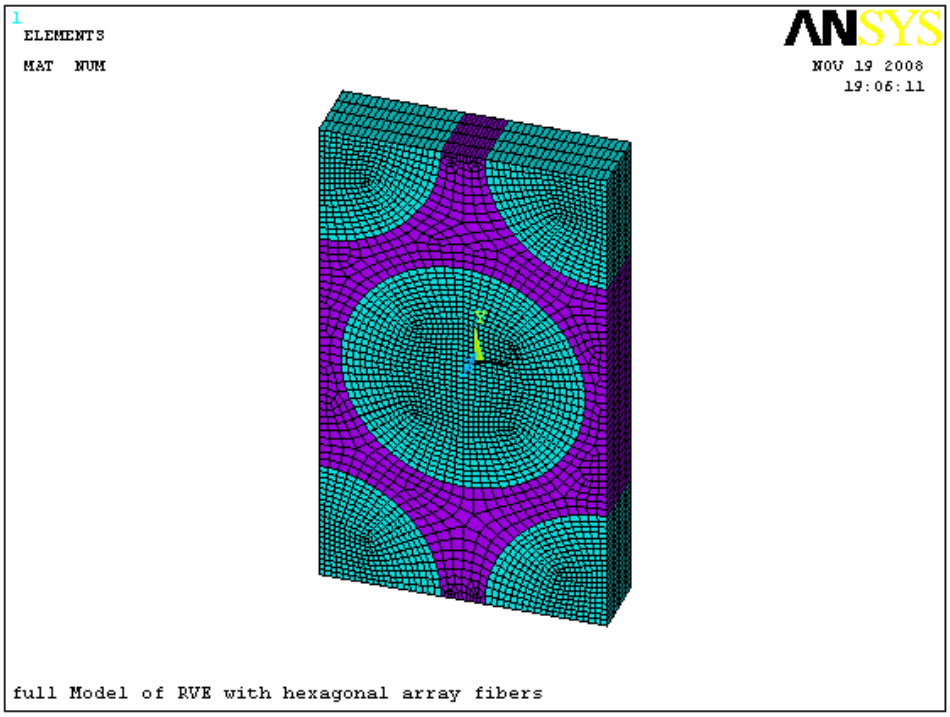

Fig.5.6.2 Full model of RVE

Solid 186 was used for generating the mesh of the RVE. Fig.5.6.2 shows the FE mesh of the RVE model. Solid 186 is a 20 noded brick element with layered and non-layered option. For the RVE model, the non-layered option was chosen by setting ***Keyopt (3) = 0*** in the element settings. After mesh generation the set of boundary conditions as described in sections (5.5.1-5.5.6) were applied. The CE command in the ANSYS Parametric Design Language (APDL) was used for defining BCs using degrees of freedom. After invoking the ***CE*** command the user is prompted for the input: ***CE, NEQN, CONST, NODE1, Lab1, NODE2, Lab2, NODE3, Lab3 .***

NEQN sets the equation reference number. ***CONST*** represents the constant term of the equation. E.g. if the first equation, $u_1(a_1, x, y) - u_1(-a_1, x, y) = 2a_1$ of the equation set 5.5.6 is considered then the constant term is $2a_1$. This term will change if strain other than unity is applied. ***NODE1*** selects one node on one of the faces of the RVE. ***Lab1*** represents the degree of freedom that is to be defined for the node selected in the previous step. ***NODE2*** selects one node on the face opposite to the face selected in ***"NODE1"*** step. ***Lab2*** is the degree of freedom of ***NODE 2*** and will remain same as in ***"Lab 1"***. Since two faces were selected at a time resulting in only two sets of nodes to be defined, hence ***NODE3, Lab3*** portion of the CE command was ignored for this case.

The boundary conditions for each column were applied to the RVE and then saved as a load step. This made sure that while running the model a particular load step/boundary condition could be activated. For this case three sets of boundary conditions were needed to find all the coefficients of the stiffness matrix. Thus the process of creating the BC and saving it as a load step was repeated three times as shown in the flow chart in Fig. 5.6.1.

From equations 5.5.7, 5.5.8, 5.5.11, 5.5.12, 5.5.15 and 5.5.23 the stiffness coefficients can be evaluated using volume averaged stress. Volume averaged stress can be mathematically represented as

$$\bar{\sigma}_{ij} = \frac{1}{V}\int_V \sigma_{ij} dv \tag{5.6.1}$$

A macro was created in Ansys using **"**create, Fname, Ext,"*** command to find the volume average stress and thus the stiffness coefficients. ***Fname*** refers to the name given to the macrofile and ***Ext*** is the file extension. The extension for a macro file is ***.mac***. In the macro file, element volume and element stresses were tabulated using **"*Etable, Lab, Item, Comp"***

command. ***Lab*** refers to any user defined label for use in subsequent commands. ***Item*** refers to the quantity that needs to be extracted into the table. For extracting element volumes ***Item*** can be set to ***Volu*** and for extracting stresses the ***Item*** is ***S.*** This stress is not for any specific node but represents the average of the stress for the gauss integral points in the element. ***Comp*** refers to the component of the item that needs to be extracted. For volumes this command is irrelevant but for stress there are six components $\left(\sigma_x, \sigma_y, \sigma_z, \sigma_{xy}, \sigma_{yz}, \sigma_{xz}\right)$ that can be extracted. So each element stress component is stored separately.

Element volumes were then multiplied with their corresponding element stresses (six components). This is the same as solving for the term $\sigma_{ij} dv$ of equation 5.6.1. The **SMULT, *LabR*, *Lab1*, *Lab2*, *FACT1*, *FACT2*** command was used for this step. ***LabR*** is the label assigned to each results. ***Lab1*** is the first labeled result item in operation. The element volume was assigned as ***Lab1***. ***Lab2*** is the second labeled result item in operation. Since volumes were to be multiplied by stresses hence ***Lab2*** was element stress. Again, in this case six stress components were used.

In the next step, the volume integral of the results of the previous step was calculated. This was same as the $\int_V \sigma_{ij} dv$ portion of equation 5.6.1. This was accomplished by SSUM and *get commands. After finding the volume integrals of the stresses, the last step was to calculate the volume average of the RVE stresses. This was same as finding $\frac{1}{V}\int_V \sigma_{ij} dv$ of equation 5.6.1. The volume integrals of the stresses obtained in the previous step were divided by the total volume of the RVE which produced the volume average of the stresses. The macro explained above was named as “rve.mac” and is shown in Appendix A-4.

Post processing of results was carried out by running the macro for each load step and calculating the stiffness coefficients $(C_{11}, C_{22}, C_{23}, C_{12}, C_{66})$. Using these coefficients all the elastic properties of the composite were calculated.

5.7 Model Validation

The elastic properties $(E_1, E_2, \upsilon_{12}, G_{12})$ predicted by the FE based RVE model were compared with other analytical models in Fig. 5.7.1 and Fig. 5.7.2. From [34] it was found that both E_1 and υ_{12} agreed well with the experimental data when predicted by Rule of Mixtures (ROM) model. The ROM models for determining E_1 and υ_{12} can be written as [34]

$$E_1 = E_{f1}\nu_f + E_m\nu_m \tag{5.7.1}$$

$$\upsilon_{12} = \upsilon_{f12}\nu_f + \upsilon_m\nu_m \tag{5.7.2}$$

where E_1, E_{f1}, E_m are the longitudinal moduli of the composite, the fiber and the matrix respectively. $\upsilon_{12}, \upsilon_{f12}, \upsilon_m$ are the major Poisson's Ratios of the composite, the fiber and the matrix respectively. ν_f and ν_m are the fiber volume fraction and the matrix volume fraction of the composite respectively with ν_m = 1-ν_f. From Fig. 5.7.1 (a) and (b) it is clear that RVE predictions for E_1 are almost identical with those of ROM model and vary by a maximum of 2.8% for υ_{12}.

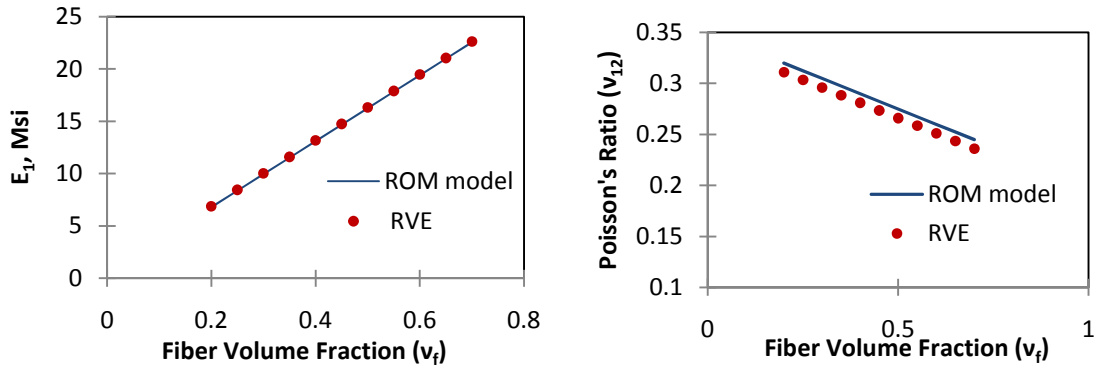

Fig.5.7.1 (a) Comparison of longitudinal modulus predicted by rule of mixtures (ROM) model with RVE model **(b)** Comparison of Poisson's Ratio predicted by rule of mixtures (ROM) with RVE model.

From [34] it was also observed that the inverse Rule of Mixture models were not effective for predicting the transverse modulus (E_2) and the shear modulus (G_{12}). The inverse rule of mixture models for estimating E_2 and G_{12} can be written as [34]

$$\frac{1}{E_2} = \frac{v_f}{E_{f2}} + \frac{v_m}{E_m} \tag{5.7.3}$$

$$\frac{1}{G_{12}} = \frac{v_f}{G_{f12}} + \frac{v_m}{G_m} \tag{5.7.4}$$

where E_2, E_{f2}, E_m are the transverse moduli of the composite, the fiber and the matrix respectively. G_{12}, G_{f12}, G_m are the in-plane shear moduli of the composite, the fiber and the matrix respectively.

Both ROM and inverse ROM models were based on simplified mechanics of materials approach and the equations were not tied to any particular fiber-packing geometry[8]. Since the results for E_1 and υ_{12} were found so favorable in [34], it was safe to conclude that these properties would be

[8] Fiber volume geometry should not be confused with fiber volume fraction. Fiber volume geometry can be triangular, square or hexagonal. Fiber volume fraction is a factor that then depends on the fiber volume geometry.

independent of fiber packing geometry. But a poor co-relation of inverse ROM models for E_2 and G_{12} with the experimental values lead to the conclusion that these properties were sensitive to fiber packing geometry [34]. To predict E_2 and G_{12} of the composite materials, different models have been proposed. Semi-empirical models such as Halpin-Tsai and Tsai-Hahn were used for this study to compare the results from the RVE model. Halpin-Tsai model can be mathematically written as [34]

$$E_2 = E_m \left[\frac{1 + \xi \eta \nu_f}{1 - \eta \nu_f} \right] \tag{5.7.5}$$

$$\text{where } \eta = \left(\frac{\frac{E_{f2}}{E_m} - 1}{\frac{E_{f2}}{E_m} + \xi} \right) \tag{5.7.6}$$

and ξ is a curve fitting parameter. Halpin-Tsai [60] found that $\xi = 2$ gave an excellent fit to the finite difference elasticity solution of Adams and Doner [61] for transverse modulus $\left(E_2\right)$. So $\xi = 2$ was used in equations 5.7.5 and 5.7.6. Similar expression could be written for shear modulus as

$$G_{12} = G_m \left[\frac{1 + \xi \eta \nu_f}{1 - \eta \nu_f} \right] \tag{5.7.7}$$

$$\text{where } \eta = \left(\frac{\frac{G_{f12}}{G_m} - 1}{\frac{G_{f12}}{G_m} + \xi} \right) \tag{5.7.8}$$

For finding G_{12} by Halpin-Tsai semi-empirical model $\xi = 1$ was used in equations 5.7.7 and 5.7.8. This value was found to provide a good co-relation to the Adams and Doner [60] for shear modulus $\left(G_{12}\right)$. Another semi-empirical model was used to determine E_2 and G_{12}. This model was proposed by Tsai and Hahn [62]. E_2 and G_{12} were evaluated by Tsai-Hahn model by the following expressions.

$$\frac{1}{E_2} = \frac{1}{\nu_f + \eta_2 \nu_m} \left[\frac{\nu_f}{E_{f2}} + \frac{\eta_2 \nu_m}{E_m} \right] \tag{5.7.9}$$

$$\frac{1}{G_{12}} = \frac{1}{\nu_f + \eta_2 \nu_m} \left[\frac{\nu_f}{G_{f12}} + \frac{\eta_2 \nu_m}{G_m} \right] \tag{5.7.10}$$

where η_2 is the stress parameter. $\eta_2 = 1$ and $\eta_2 = 0.5$ were used as inputs for equations 5.7.9 and 5.7.10 respectively.

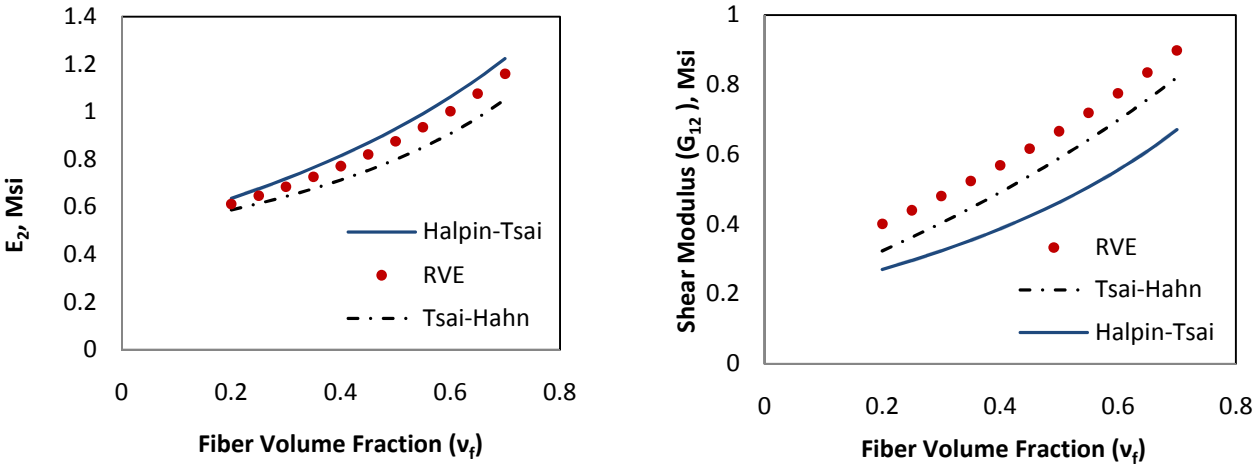

(a) **(b)**

Fig.5.7.2 (a) Comparison of Transverse Modulus predicted by Halpin-Tsai and Tsai-Hahn with the RVE model **(b)** Comparison of Shear modulus predicted by Halpin-Tsai and Tsai-Hahn with the RVE model

From Fig.5.7.2 (a) it is observed that the transverse modulus (E_2) predicted by RVE model agreed well with both Halpin-Tsai and Tsai-Hahn model. Maximum % error between the transverse modulus predicted by the RVE and that between Halpin-Tsai and Tsai-Hahn model was 5.22% and 9.3% respectively. From Fig.5.7.2 (b) it is observed that the shear moduli (G_{12}) values predicted by the RVE model for different fiber volume fractions followed the values predicted by Tsai-Hahn closely with a maximum % error of 8.6%. However, the Halpin-Tsai model that showed good co-relation with the RVE model for the transverse modulus values didn't co-relate well with it for the shear modulus values. The predicted shear modulus of the Halpin-Tsai model for the fiber volume fraction of 0.7 was 25% lower than that of RVE model. This poor co-relation can be attributed to the fact that the semi-empirical models are based on curve fitting parameters. A good co-relation of a semi-empirical model for a particular set of data may not necessarily guarantee a good co-relation with a different set. In this case when Halpin-Tsai used $\xi = 1$ for estimating the shear modulus for E-glasss/epoxy material, it provided the an excellent fit to the finite difference elasticity solution of Adam and Doner [61]. However, the

same assumption didn't hold true for our study. The elastic properties predicted by the FE based RVE model for T300-934 material were also compared with the experimental values available for the same material for a fiber volume fraction of 0.65 [34]. The comparison is shown in table 5.7.1.

Table 5.7.1 Elastic properties of T300:934 (graphite/epoxy) composite material by using experimental methods and RVE model for a fiber volume fraction of 0.65

	$E_1(Msi)$	$E_2(Msi)$	υ_{12}	$G_{12}(Msi)$
RVE Model	21	1.07	0.24	0.89
Experiment	19	1.03	0.22	1

5.8 Chapter Summary

From Table 5.7.1 it is observed that the RVE model predictions compare well with those of the experimental values. From the comparison of the RVE model with ROM models, semi-empirical models and the experimentally obtained values it is clear that FE based RVE model can be used as a tool for finding homogenized elastic properties of the composite materials. Further, all the elastic properties were obtained by a single model. This is a better numerical practice than using different models viz. ROM models for E_1 and v_{12} and semi-empirical models for E_2 *and* G_{12}.

6. Conclusion

The strength of traditional laminated composites with a circular hole can be increased by changing the lay-ups and the stacking sequence of the constituent laminae. This study has shown the relevance of using a 3D model to optimize strength. The laminate strain concentration factor (K_t) was an unreliable indictor of lay-ups with increased strength. The stress-strain response showed material and geometric non-linearities. Thus, the linear 3D model was used to determine the FPF. Of all the seven failure theories used in this work only Maximum-Stress and Maximum-Strain predicted FPF within 10% error of the measured values. By comparing the non-traditional laminates with the baseline, some observation could be made. When 90 degree plies were replaced by other angles both FPF and UTS of the laminates increased. Laminates where 90 degree plies were changed showed a shift in the failure mode from transverse to shear. Changing 0 degree plies had severe effect on the FPF as well as the UTS of the laminates. As far as the off axis plies are concerned, the FPF and the UTS increased when their angles approached the loading direction and decreased when they deviated away from it.

The presence of circular notches exposed some laminates to high interlaminar stresses. A 3D model of un-notched specimen agreed well with qualitative analytical solution of Pipes and Pagano. A Quadratic Delamination Criterion used in conjunction with the FE model provided good agreement with experimental observations of delamination.

Computational micromechanics was used as an FE based RVE model to predict elastic properties of composites without the need for experimentation. The model showed good correlation with the experimental values and proved to be a better numerical technique of determining the elastic properties of a composite lamina. For achieving the same results different analytical and semi-empirical models had to be used which is not a very reliable approach.

References

1. Aryjal, B. P., "In-situ stress/strain Measurement in Composites Using an Aramid Fiber as Sensor," *Ph.D. diss.*, University of London (1998).

2. Soden, P. D., Kaddour, A. S., Hinton, M. J., "Recommendations for designers and researchers resulting from the world-wide failure exercise," *Composite Science and Technology*, 64, 2004, 589.

3. Daniel, I.M., and Ishai, O., "Engineering Mechanics of Composite Materials," *Oxford University Press*, 2006.

4. Miller, E., "Introduction to Plastics and Composites," *Marcel Dekker, Inc.*, 1995.

5. Tan, S.C., "Mixed-Mode Fracture of Notched Unidirectional and Off-Axis Laminates Under Tensile Loading," *Journal of Composite Materials*, 23, 1989, 1082.

6. Lo, K.H., Wu, E.M. and Konishi, D.Y., "Failure Strength of Notched Composite Laminates," *Journal of Composite Materials,* 17, 1983, 384.

7. Greszezuk, L.B., "Stress Concentration and Failure Criteria for Orthotropic and Anisotropic Plates with Circular Openings," *ASTM STP 497*, 1988, 363.

8. Tan, S.C., "Finite-Width Correction factor for Anisotropic Plate Containing a Central Openings," *Journal of Composite Materials*, 22, 1988, 1080.

9. Tan, S.C., "An Iterative Method of Optimal Design with Composite Laminates Containing an Elliptical Opening," *Journal of Composite Materials*, 4, 1985, 297.

10. Lakshiminarayan, H.V., "Stress Distribution Around a Semi-Circular Edge-Notch in a finite Size Laminated Composite Plate Under Uniaxial Tension," *Journal of Composite Materials*, 17, 1983, 357.

11. Lin, C.C. and Ko, C.C., "Stress and Strength Analysis of Finite Composite Laminates with Elliptical Holes," *Journal of Composite Materials,* 22, 1988, 374.

12. Chang, K.Y., Liu, S. and Chang, F.K., "Damage Tolerance of Laminated Composite Containing an Open Hole and Subjected to Tensile Loading," *Journal of Composite Materials*, 5, 1990, 274.

13. Lekhnitskii, S.G., "Theory of Elasticity of an Anisotropic Body," *Holden-Day Inc.*, SanFrancisco, CA, 1963.

14. Konish, H.J. and Whitney, J.M., "Approximate Stresses in an Orthotropic Plate Containing a circular hole," *Journal of Composite Materials*, 9, 1975, 157.

15. Karlak, R.F., "Hole Effects in a Related Series of Symmetrical Laminates," Proc. 4th Joint ASM, Metallurgical Society of the AIME, Warrendale, PA, 1979,105.

16. Kim, J., Kim, D. and Takeda, N., "Notched Strength and Fracture Criterion in Fabric Composite Plates Containing a Circular Hole," *Journal of Composite Materials*, 29, 1995,982.

17. Whitworth, H.A., Mahase, A. Stress concentration in graphite/epoxy laminates containing a circular hole. Journal of Advanced Materials 31 (1999) 45-51.

18. Yan, U.M., Sun, H.T., Wei, W.D., Chang, F.K., "Response and Failure of Composite Plates with Bolt-Filled Hole," National Technical Information Service (NTIS), DOT/FAA/AR-97/85, 1998.

19. Daniel, I.M. Rowlands, R.E., Whiteside J.B., " Effects of Material and Stacking Sequence on Behavior of Composite Plates with Holes," Experimental Mechanics, 14, 1974, 1.

20. Park, H.J., "Bearing failure analysis of mechanical fastened joints in composite laminates," *Composite Structures*, 53, 2001,199.

21. Quinn, W.J., "The effect of stacking sequence on laminate strength," *Journal of Composite materials*, 11, 1971, 139.

22. Marshall, I.H., Arnold. W.S., Wood J., "Observations on bolted connections in composite structures," *Composite Structure*, 13, 1989, 133.

23. Chen, W.H., Lee S.S., Yeh J.T., "Three-dimentional contact stress analysis of a composite laminate with bolted joint," *Composite Structure*, 29, 1995, 329.

24. Park, H.J., "Effect of stacking sequence and clamping force on the bearing strengths of mechanically fastened joints in composite laminates," *Composite Structures*, 50, 2000, 287.

25. Kaminski, B.E., "On the Determination of the Failure Surface for an Orthotropic Quasi-Homogenous Material," *Master's Thesis*, Georgia Institute of Technology, June 1969.

26. Jenkins, C.F., "Report on Materials of Construction used in Aircraft and Aircraft Engines," *Great Britain Aeronautical Research Committee*, 1920.

27. Kelly, A., "Strong Solids," *Clarendon Press*, Oxford, 1966.

28. Waddoups, M.E., "Advanced Composite Material Mechanics for the design and Stress Analyst," *General Dynamics*, Fort Worth, TX, 1967

29. Hashin, Z. and Rothem, A., " A Fatigue Failure Criterion for Fiber Reinforced Materials," *Journal of Composite Materials*, 7, 1973, 448.

30. Hashin, Z., "Failure Criteria for Unidirectional Fiber Composites," *Journal of Applied Mechanics*, 47, 1980, 329.

31. Rattanawangcharoen, N., "First-ply Failure Analysis of Laminated Composite Cylindrical Panels," *Journal of Reinforced Composites*, 24, 2005, 1521.

32 Tsai, S.W., Wu, E.M., "A General Theory of Strength of Anisotropic Materials", 5, 1971, 58.

33. Gol'denblat, I., Kopnov, V.A., "Strength of Glass Reinforced Plastics in the Complex Stress State," *Polymer Mechanics*, 1, 1966, 54.

34. Gibson, R.F., "Principles of Composite Material Mechanics," *McGraw-Hill, Inc.*, 1994.

35. Barakat, S.A., Abu-Farsakh, G.A., "The Use of an Energy based Criterion to Determine Optimum Configuration of Fibrous Composites," *Composite Science and Technology*, 59, 1999, 1891.

36. Sun, C.T., Quinn, B.J., "Evaluation of Failure Crietria Using Off-Axis Laminate Specimens," *Proc. American Society of Composites*, Ninth Technical Conference, Sept. 1994, 97.

37. Sun, C.T., "Strength Analysis of Unidirectional Composites and Laminates," in Comprehensive Composite Materials, Kelly, A. and Zweben, C, *Ch. 1.20, Elsevier Science, Ltd.*, Oxford, 2000.

38. Soden, P.D., Kaddour, A.S., Hinton, M.J., "Recommendations for Designers and Researchers Resulting from the World-Wide Failure Exercise," *Composite Science and Technology*, 64, 2004, 589.

39. Tay, T.E., Tan, V.B.C, Tan, S.H.N., "Element Failure: An Alternative to Material Property Degradation Method for Progressive Damage in Composite Structures," *Journal of Composite Material*, 39, 2005, 1659.

40. Gosse, J.H., Christensen, S., "Strain Invariant Failure Criteria For Polymers in Composite Materials," *AIAA-2001-1184*, 2001.

41. Wang, J., Callus, P.J., Bannister, M.K., "Experimental and Numerical Investigation of the Tension and Compression Strength of un-notched and notched quasi-isotropic laminates," *Composite Structures*, 64, 2004, 297.

42. Ugural, A.C., Fenster, S.K.., "Advanced Strength and Applied Elasticity," *Pretence Hall PTR*, 2003.

43. Mallick, P.K., "Composite Engineering Handbook, CRC, 1997.

44. Arjyal, B.P., Katerelos, D.G., Filiou, C., Galiotis C., "Measurement and Modeling of Stress Concentration around a Circular Notch," *Experimental Mechanics*, 40, 2000, 248.

45. Tan, S.C., "Finite-width Correction Factors for Anisotropic Plates Containing a Central Opening," *Journal of Composite Materials*, 22, 1988, 1080.

46. Stone, D.P., "The influence of Ply Orientation in the Open-Hole Tension Strength of Composite Laminates", *Master's Thesis*, Washington State University (2007).

47. Cheng, P., Michael, S.A., Schreir, H.W., McNeill, S.R., "Full-field Speckle Pattern Image Correlation with B-spline Deformation Function," *Experimental Mechanics*, 42, 2002, 344

48. Lagattu, F., Brillaud, J., Lafarie-Frenot M.C., "High Strain Gradient Measurement by Using Digital Image Correlation Technique," *Material Characterization*, 53, 2004, 17.

49. Schreier, H.W., Sutton, M.A., "Systematic Error in Digital Image Correlation Due to Undermatched Subset Shape Functions," *Experimental Mechanics*, 42, 2002, 303.

50. Strong, A.B., "Fundamentals of Composite Manufactuing: Materials, Methods and Applications," *Technology and Engineering*, 2007

51. Pipes, R.B. and Pagano, N.J., "Interlaminar Stresses in Composite Laminates under Uniform Axial Extension", *Journal of Composite Materials*, 4, 1970, 538.

52. Pipes, R.B. and Pagano, N.J., "The Influence of Stacking Sequence on Laminate Strength", *Journal of Composite Materials*, 5, 1971, 50.

53. Foye, R.L. and Baker, D.J., "Design of Orthotropic Laminates", presented at the 11th Annual AIAA Structures, *Structural Dynamics, and Materials Conference*, Denver, Colorado, April 1970.

54. Newaz, G.M., "Delamination in Advanced Composites", *Technomic Publishing Co*., Lancaster, PA (1991).

55. Brewer, J.C. and Lagace, P.A., "Quadratic Stress Criterion for Initiation of Delamination", *Journal of Composite Materials*, 22, 1988, 1141.

56. Kim, R.Y and Soni, S.R., "Experimental and Analytical Studies on the Onset of Delamination in Laminated Composites", *Journal of Composite Materials*, 18,1984,70.

57. O'Brien, T.K., "Characterization of Delamination Onset and Growth in a Composite Laminate", Damage in Composite Materials, ASTM STP 775, *American Society for Testing and Materials*, 1982, 140

58. Barbero, E.J., "Finite Element Analysis of Composite Materials", *CRC Press*, 2007.

59. Barbero, E.J., Luciano, R. "Micromechanical Formulas for the Relaxation Tensor of Linear Viscoelastic Composites with Transversely Isotropic Fibers", *International Journal of Solids and Structures*, 32, 1995, 1859.

60. Halpin, J.C. and Tsai, S.W., "Effects of Environmental Factors on Composite Material", *AFML-TR-67-423*, 1969

61. Adams, D.F., Doner, D.R., "Transverse Normal Loading of a Unidirectional Composite", Journal of Composite Material, 1, 1967, 152.

62. Tsai, S.W., Hahn, H.T., "Introduction to Composite Materials", *Technomic Publishing Co.*, 1980.

APPENDIX

Appendix A-1

Recovery shear strain Vs recovery time

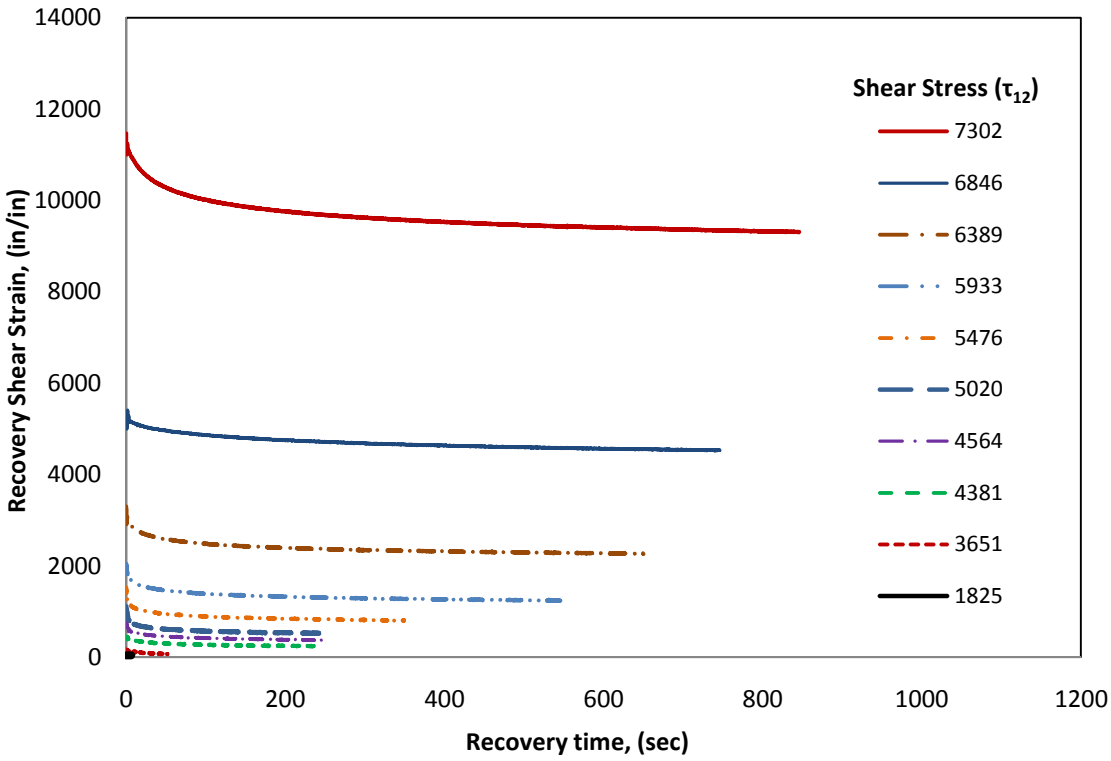

Appendix A-2

```
!Code for linear static analysis of 1/8th notched composite plate

!create geometry

BATCH

/PREP7

PI=3.1415926

H_radius=0.125 !hole radius (in)

P_width = 0.75 !plate width (in)

P_height = 1.25 !plate height (in)

P_thickness = 0.07 ! plate thickness (in)

B_point = 0.3 ! bifurcation point for mesh around the hole

a= 16     ! Mesh refinement factor near hole

b= 30 ! Mesh refinement factor away from the hole

!Create keypoints

/PREP7

K,1,H_radius,0,0,

K,2,B_point,0,0,

K,3,P_width,0,0,

K,4,P_width,B_point,0,

K,5,P_width,P_height,0,

K,6,B_point,P_height,0,

K,7,0,P_height,0,

K,8,0,B_point,0,

K,9,0,H_radius,0,

K,10,H_radius*cos (PI/4),H_radius*sin (PI/4),0,

K,11,B_point,B_point,0,

K,12,H_radius,0,-(P_thickness)/2,

K,13,B_point,0,-(P_thickness)/2,

K,14,P_width,0,-(P_thickness)/2,

K,15,P_width,B_point,-(P_thickness)/2,

K,16,P_width,P_height,-(P_thickness)/2,

K,17,B_point,P_height,-(P_thickness)/2,

K,18,0,P_height,-(P_thickness)/2,
```

K,19,0,B_point,-(P_thickness)/2,

K,20,0,H_radius,-(P_thickness)/2,

K,22,H_radius*cos (PI/4),H_radius*sin (PI/4),-(P_thickness)/2,

K,23,B_point,B_point,-(P_thickness)/2,

K,100,0,0,0,

K,101,0,0,-(P_thickness)/2,

!Create lines using keypoints

LSTR, 1, 2

LSTR, 2, 3

LSTR, 3, 4

LSTR, 4, 5

LSTR, 5, 6

LSTR, 6, 7

LSTR, 7, 8

LSTR, 8, 9

LSTR, 8, 11

LSTR, 11, 4

LSTR, 12, 13

LSTR, 13, 14

LSTR, 14, 15

LSTR, 15, 16

LSTR, 16, 17

LSTR, 17, 18

LSTR, 18, 19

LSTR, 19, 20

LSTR, 19, 23

LSTR, 23, 15

LSTR, 9, 20

LSTR, 8, 19

LSTR, 7, 18

LSTR, 6, 17

LSTR, 5, 16

LSTR, 4, 15

LSTR, 3, 14

LSTR, 2, 13

LSTR, 1, 12

LSTR, 10, 22

LSTR, 11, 23

LSTR, 2, 11

LSTR, 13, 23

LSTR, 10, 11

LSTR, 22, 23

LSTR, 11, 6

LSTR, 23, 17

!Create arc for representing circular notch

LARC,10,9,100,H_radius

LARC,1,10,100,H_radius

LARC,12,22,101,H_radius

LARC,22,20,101,H_radius

KDELE,100,101 !Delete keypoints initially needed for arc generation

!Create Areas using lines

AL,1,39,34,32

AL,1,29,11,28

AL,29,39,30,40

AL,34,30,35,31

AL,11,40,35,33

AL,28,32,31,33

AL,34,30,35,31

AL,34,38,8,9

AL,8,21,18,22

AL,9,22,19,31

AL,30,38,21,41

AL,41,18,19,35

AL,2,28,12,27

AL,28,32,31,33

AL,10,31,20,26

AL,27,3,26,13

AL,3,2,32,10

AL,13,12,33,20

AL,9,22,19,31

AL,22,7,23,17

AL,6,23,16,24

AL,36,24,37,31

AL,9,7,6,36

AL,19,17,16,37

AL,10,31,20,26

AL,31,36,24,37

AL,5,24,15,25

AL,4,25,14,26

AL,10,36,5,4

AL,20,37,15,14

!Create volumes using areas

VA,1,2,3,4,5,6

VA,4,7,8,9,10,11

VA,6,12,13,14,15,16

VA,9,17,18,19,20,21

VA,19,13,22,23,24,25

wpstyle,0.004375,0.1,-1,1,0.003,0,2,,5

!Dividing volume into layers for applying composite properties

!current model which is one-eighth uses 8 plies and thus work

!plane is called 7 times to create the desired number of layers.

*do,i,1,7,1

wpof,,,-0.004375

VSBW,ALL

*end do

VGLUE, ALL !Glue all the volumes together

!Use mathcad to calculate stiffness matrix for each ply

!since four plies are repeated so 4 sets of stiffness matrices are used as input.

TOFFST,273

TB,ANEL,1,1,21,0

TBTEMP,28

TBDATA,,1.59e6,6.429e5,5.7e5,0,0,0

TBDATA,,2.011e7,6.429e5,0,0,0,1.59e6

TBDATA,,0,0,0,1.624e6,0,0

TBDATA,,1.624e6,0,1.624e6,,,

TB,ANEL,2,1,21,0

TBTEMP,28

TBDATA,,1.59e6,6.429e5,5.7e5,0,0,0

TBDATA,,2.011e7,6.429e5,0,0,0,1.59e6

TBDATA,,0,0,0,1.624e6,0,0

TBDATA,,1.624e6,0,1.624e6,,,

TB,ANEL,3,1,21,0

TBTEMP,28

TBDATA,,1.59e6,6.429e5,5.7e5,0,0,0

TBDATA,,2.011e7,6.429e5,0,0,0,1.59e6

TBDATA,,0,0,0,1.624e6,0,0

TBDATA,,1.624e6,0,1.624e6,,,

TB,ANEL,4,1,21,0

TBTEMP,28

TBDATA,,1.59e6,6.429e5,5.7e5,0,0,0

TBDATA,,2.011e7,6.429e5,0,0,0,1.59e6

TBDATA,,0,0,0,1.624e6,0,0

TBDATA,,1.624e6,0,1.624e6,,,

!Define the element used. For this work Solid 64 which is 8 noded

!brick element is used. The element coordinate system can be set

!parallel to global. The y axis in this work corresponds to 1-dir.

ET,1,SOLID64

KEYOPT,1,1,0

KEYOPT,1,5,0

KEYOPT,1,6,0

!Assigning material properties to each layer.

FLST,5,10,6,ORDE,10

FITEM,5,12,14,6,8,10,34,35,11,23,33,

CM,_Y,VOLU

VSEL, , , ,P51X

CM,_Y1,VOLU

CMSEL,S,_Y

CMSEL,S,_Y1

VATT,1, ,1,0

CMSEL,S,_Y

CMDELE,_Y

CMDELE,_Y1

FLST,5,10,6,ORDE,10

FITEM,5,19,20,16,17,18,39,40,36,37,38

CM,_Y,VOLU

VSEL, , , ,P51X

CM,_Y1,VOLU

CMSEL,S,_Y

CMSEL,S,_Y1

VATT,2, ,1,0

CMSEL,S,_Y

CMDELE,_Y

CMDELE,_Y1

FLST,5,10,6,ORDE,10

FITEM,5,24,25,9,13,21,44,45,15,41,43

CM,_Y,VOLU

VSEL, , , ,P51X

CM,_Y1,VOLU

CMSEL,S,_Y

CMSEL,S,_Y1

VATT,3, ,1,0

CMSEL,S,_Y

CMDELE,_Y

CMDELE,_Y1

FLST,5,10,6,ORDE,10

FITEM,5,29,30,26,27,28,32,42,7,22,31

CM,_Y,VOLU

VSEL, , , ,P51X

CM,_Y1,VOLU

CMSEL,S,_Y

CMSEL,S,_Y1

VATT,4, ,1,0

CMSEL,S,_Y

CMDELE,_Y

CMDELE,_Y1

!Mesh the layers

FLST,5,27,4,ORDE,27

FITEM,5,2

FITEM,5,5

FITEM,5,10

FITEM,5,12

FITEM,5,15

FITEM,5,20

FITEM,5,62

FITEM,5,65

FITEM,5,77

FITEM,5,82

FITEM,5,85

FITEM,5,93

FITEM,5,114

FITEM,5,117

FITEM,5,127

FITEM,5,134

FITEM,5,137

FITEM,5,145

FITEM,5,164

FITEM,5,167

FITEM,5,177

FITEM,5,186

FITEM,5,189

FITEM,5,197

FITEM,5,216

FITEM,5,219

FITEM,5,229

CM,_Y,LINE

LSEL, , , ,P51X

CM,_Y1,LINE

CMSEL,,_Y

!*

LESIZE,_Y1, , ,2*a, , , , ,1

FLST,5,27,4,ORDE,27

FITEM,5,4

FITEM,5,7

FITEM,5,14

FITEM,5,17

FITEM,5,36

FITEM,5,-37

FITEM,5,71

FITEM,5,-72

FITEM,5,76

FITEM,5,89

FITEM,5,-90

FITEM,5,92

FITEM,5,123

FITEM,5,-124

FITEM,5,126

FITEM,5,141

FITEM,5,-142

FITEM,5,144

FITEM,5,173

FITEM,5,-174

FITEM,5,176

FITEM,5,193

FITEM,5,-194

FITEM,5,196

FITEM,5,223

FITEM,5,-224

FITEM,5,228

CM,_Y,LINE

LSEL, , , ,P51X

CM,_Y1,LINE

CMSEL,,_Y

!*

LESIZE,_Y1, , ,2*b, , , , ,1

FLST,5,70,4,ORDE,61

FITEM,5,1

FITEM,5,6

FITEM,5,9

FITEM,5,11

FITEM,5,16

FITEM,5,19

FITEM,5,23

FITEM,5,-24

FITEM,5,26

FITEM,5,-28

FITEM,5,34

FITEM,5,-35

FITEM,5,38

FITEM,5,-42

FITEM,5,44

FITEM,5,47

FITEM,5,-50

FITEM,5,52

FITEM,5,-53

FITEM,5,57

FITEM,5,-58

FITEM,5,60

FITEM,5,66

FITEM,5,-67

FITEM,5,70

FITEM,5,73

FITEM,5,79

FITEM,5,-81

FITEM,5,83

FITEM,5,88

FITEM,5,94

FITEM,5,97

FITEM,5,105

FITEM,5,109

FITEM,5,-110

FITEM,5,113

FITEM,5,115

FITEM,5,120

FITEM,5,122

FITEM,5,131

FITEM,5,-133

FITEM,5,135

FITEM,5,140

FITEM,5,146

FITEM,5,149

FITEM,5,157

FITEM,5,159

FITEM,5,161

FITEM,5,-163

FITEM,5,165

FITEM,5,170

FITEM,5,172

FITEM,5,183

FITEM,5,-184

FITEM,5,192

FITEM,5,198

FITEM,5,201

FITEM,5,209

FITEM,5,213

FITEM,5,-214

FITEM,5,222

CM,_Y,LINE

LSEL, , , ,P51X

CM,_Y1,LINE

CMSEL,,_Y

!*

LESIZE,_Y1, , ,2*a, , , , ,1

FLST,5,70,4,ORDE,60

FITEM,5,3

FITEM,5,8

FITEM,5,13

FITEM,5,18

FITEM,5,25

FITEM,5,27

FITEM,5,-29

FITEM,5,31

FITEM,5,-35

FITEM,5,38

FITEM,5,-41

FITEM,5,46

FITEM,5,-49

FITEM,5,55

FITEM,5,-56

FITEM,5,58

FITEM,5,-59

FITEM,5,64

FITEM,5,66

FITEM,5,-67

FITEM,5,80

FITEM,5,-81

FITEM,5,83

FITEM,5,-84

FITEM,5,86

FITEM,5,91

FITEM,5,97

FITEM,5,99

FITEM,5,105

FITEM,5,-106

FITEM,5,108

FITEM,5,110

FITEM,5,112

FITEM,5,-113

FITEM,5,115

FITEM,5,-116

FITEM,5,132

FITEM,5,-133

FITEM,5,135

FITEM,5,-136

FITEM,5,143

FITEM,5,149

FITEM,5,151

FITEM,5,157

FITEM,5,-160

FITEM,5,162

FITEM,5,-163

FITEM,5,165

FITEM,5,-166

FITEM,5,169

FITEM,5,184

FITEM,5,188

FITEM,5,201

FITEM,5,203

FITEM,5,209

FITEM,5,211

FITEM,5,-212

FITEM,5,214

FITEM,5,218

FITEM,5,226

CM,_Y,LINE

LSEL, , , ,P51X

CM,_Y1,LINE

CMSEL,,_Y

!*

LESIZE,_Y1, , ,2*a, , , , ,1

FLST,5,88,4,ORDE,43

FITEM,5,42

FITEM,5,-43

FITEM,5,45

FITEM,5,47

FITEM,5,50

FITEM,5,-51

FITEM,5,54

FITEM,5,-55

FITEM,5,61

FITEM,5,63

FITEM,5,68

FITEM,5,-69

FITEM,5,73

FITEM,5,-75

FITEM,5,78

FITEM,5,94

FITEM,5,-105

FITEM,5,107

FITEM,5,111

FITEM,5,-112

FITEM,5,118

FITEM,5,-121

FITEM,5,125

FITEM,5,128

FITEM,5,-130

FITEM,5,146

FITEM,5,-157

FITEM,5,159

FITEM,5,168

FITEM,5,-171

FITEM,5,175

FITEM,5,178

FITEM,5,-182

FITEM,5,198

FITEM,5,-211

FITEM,5,215

FITEM,5,217

FITEM,5,220

FITEM,5,-221

FITEM,5,225

FITEM,5,-227

FITEM,5,230

FITEM,5,-234

CM,_Y,LINE

LSEL, , , ,P51X

CM,_Y1,LINE

CMSEL,,_Y

!*

LESIZE,_Y1, , ,2, , , , ,1

MSHAPE,0,3D

MSHKEY,1

VMESH,ALL

!Apply boundary condition

/SOL

FLST,2,16,5,ORDE,16

FITEM,2,26

FITEM,2,31

FITEM,2,40

FITEM,2,42

FITEM,2,53

FITEM,2,66

FITEM,2,73

FITEM,2,86

FITEM,2,89

FITEM,2,106

FITEM,2,113

FITEM,2,130

FITEM,2,133

FITEM,2,146

FITEM,2,153

FITEM,2,173

DA,P51X,SYMM

FLST,2,16,5,ORDE,16

FITEM,2,35

FITEM,2,50

FITEM,2,59

FITEM,2,70

FITEM,2,77

FITEM,2,98

FITEM,2,110

FITEM,2,117

FITEM,2,121

FITEM,2,123

FITEM,2,138

FITEM,2,150

FITEM,2,157

FITEM,2,164

FITEM,2,167

FITEM,2,178

DA,P51X,SYMM

FLST,2,5,5,ORDE,5

FITEM,2,5

FITEM,2,11

FITEM,2,16

FITEM,2,21

FITEM,2,25

DA,P51X,SYMM

!Apply load

FLST,2,16,5,ORDE,16

FITEM,2,49

FITEM,2,57

FITEM,2,76

FITEM,2,80

FITEM,2,97

FITEM,2,100

FITEM,2,116

FITEM,2,120

FITEM,2,137

FITEM,2,140

FITEM,2,156

FITEM,2,160

FITEM,2,163

FITEM,2,171

```
FITEM,2,177
FITEM,2,180
/GO
!*
SFA,P51X,1,PRES,-30000
```

Appendix A-3

Strain Vs X distance

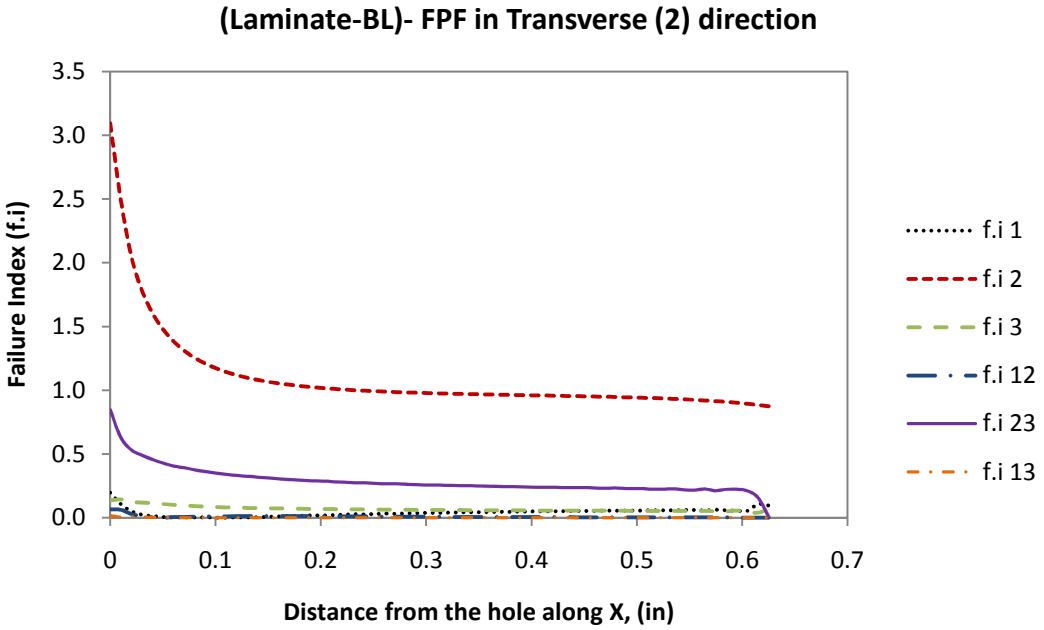

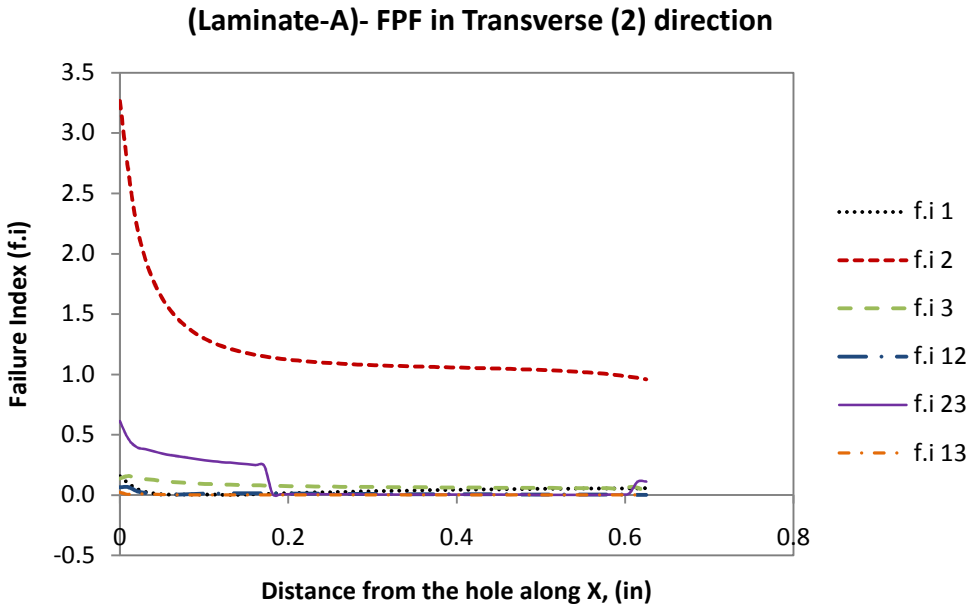

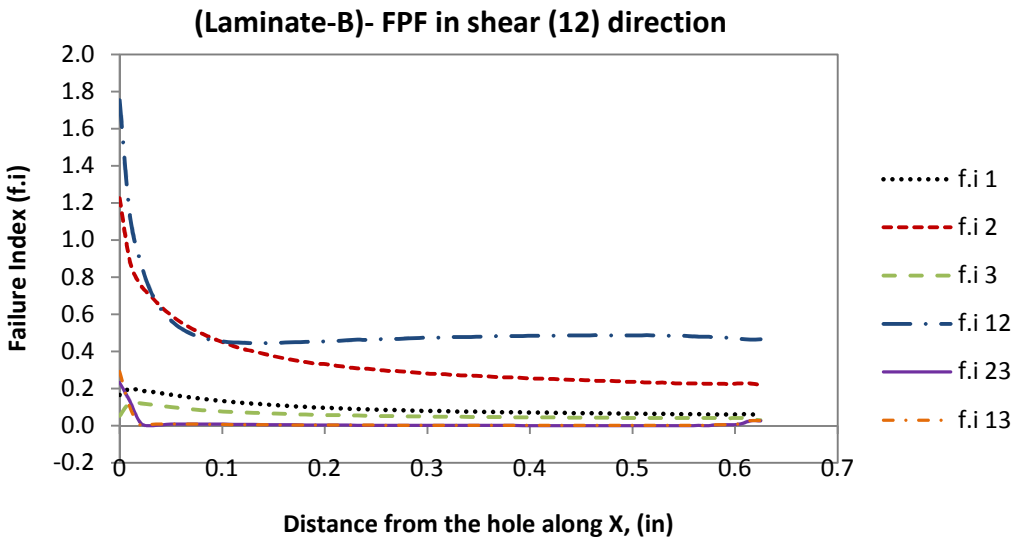
(Laminate-B)- FPF in shear (12) direction
Failure Index (f.i)
2.0
1.8
1.6
1.4
1.2
1.0
0.8
0.6
0.4
0.2
0.0
-0.2
0
0.1
0.2
0.3
0.4
0.5
0.6
0.7
Distance from the hole along X, (in)
f.i 1
f.i 2
f.i 3
f.i 12
f.i 23
f.i 13

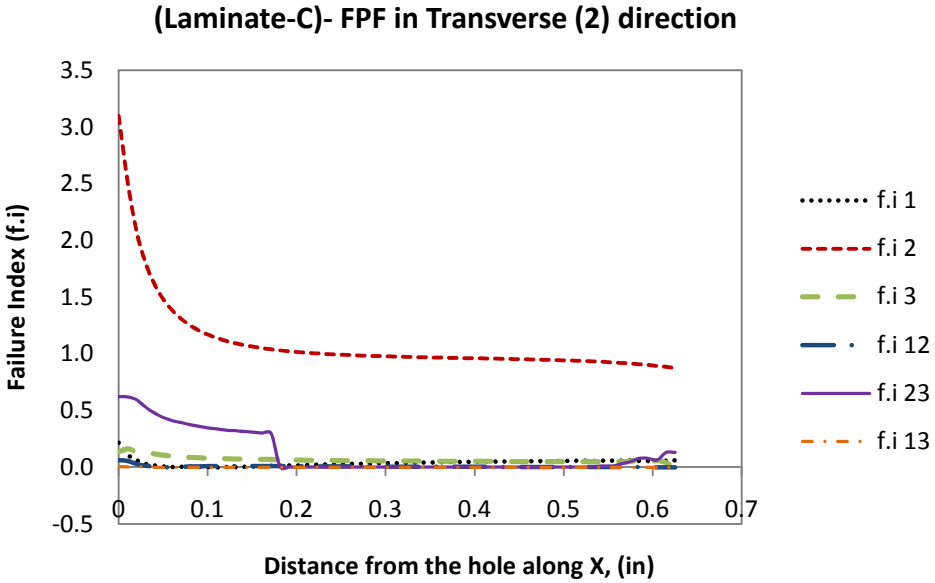
(Laminate-C)- FPF in Transverse (2) direction
Failure Index (f.i)
3.5
3.0
2.5
2.0
1.5
1.0
0.5
0.0
-0.5
0
0.1
0.2
0.3
0.4
0.5
0.6
0.7
Distance from the hole along X, (in)
f.i 1
f.i 2
f.i 3
f.i 12
f.i 23
f.i 13

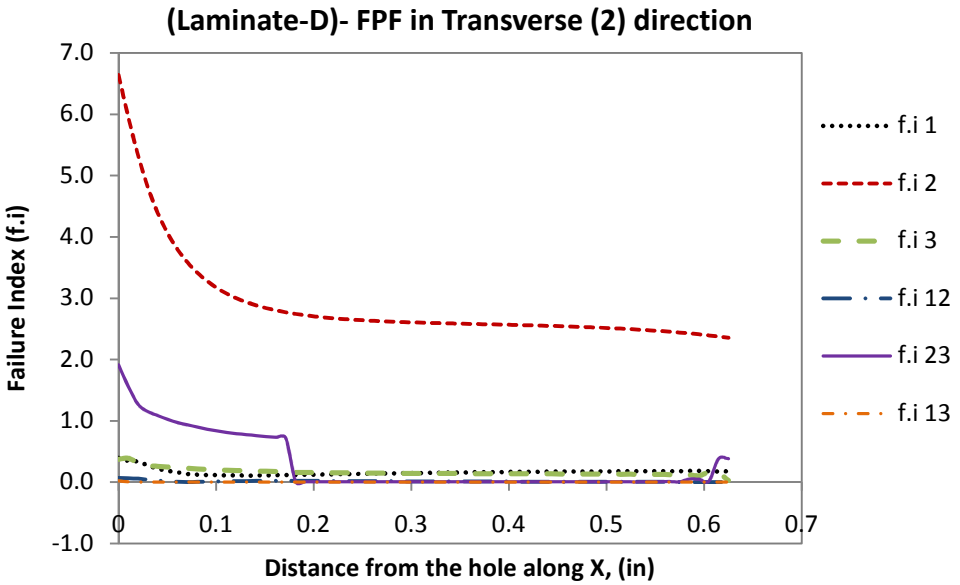
(Laminate-D)- FPF in Transverse (2) direction
Failure Index (f.i)
7.0
6.0
5.0
4.0
3.0
2.0
1.0
0.0
-1.0
0
0.1
0.2
0.3
0.4
0.5
0.6
0.7
Distance from the hole along X, (in)
f.i 1
f.i 2
f.i 3
f.i 12
f.i 23
f.i 13

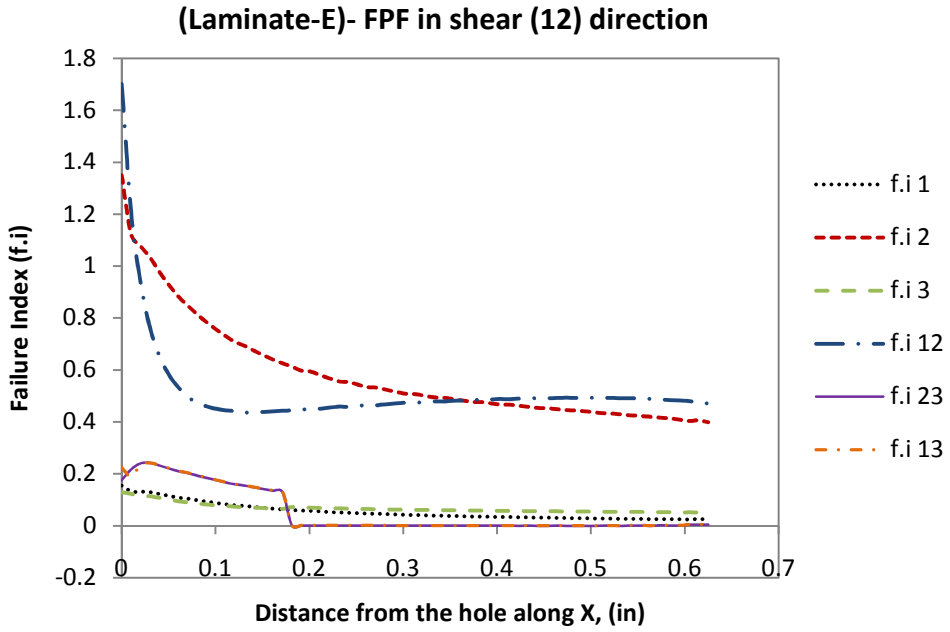
(Laminate-E)- FPF in shear (12) direction
Failure Index (f.i)
1.8
1.6
1.4
1.2
1
0.8
0.6
0.4
0.2
0
-0.2
0
0.1
0.2
0.3
0.4
0.5
0.6
0.7
Distance from the hole along X, (in)
f.i 1
f.i 2
f.i 3
f.i 12
f.i 23
f.i 13

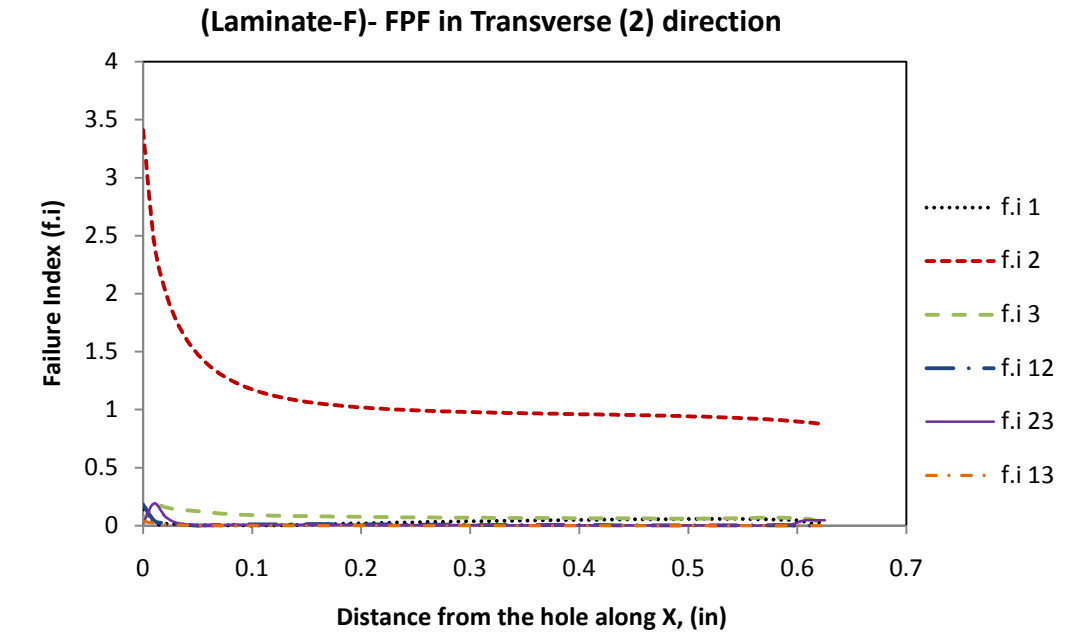
(Laminate-F)- FPF in Transverse (2) direction
Failure Index (f.i)
4
3.5
3
2.5
2
1.5
1
0.5
0
0
0.1
0.2
0.3
0.4
0.5
0.6
0.7
Distance from the hole along X, (in)
f.i 1
f.i 2
f.i 3
f.i 12
f.i 23
f.i 13

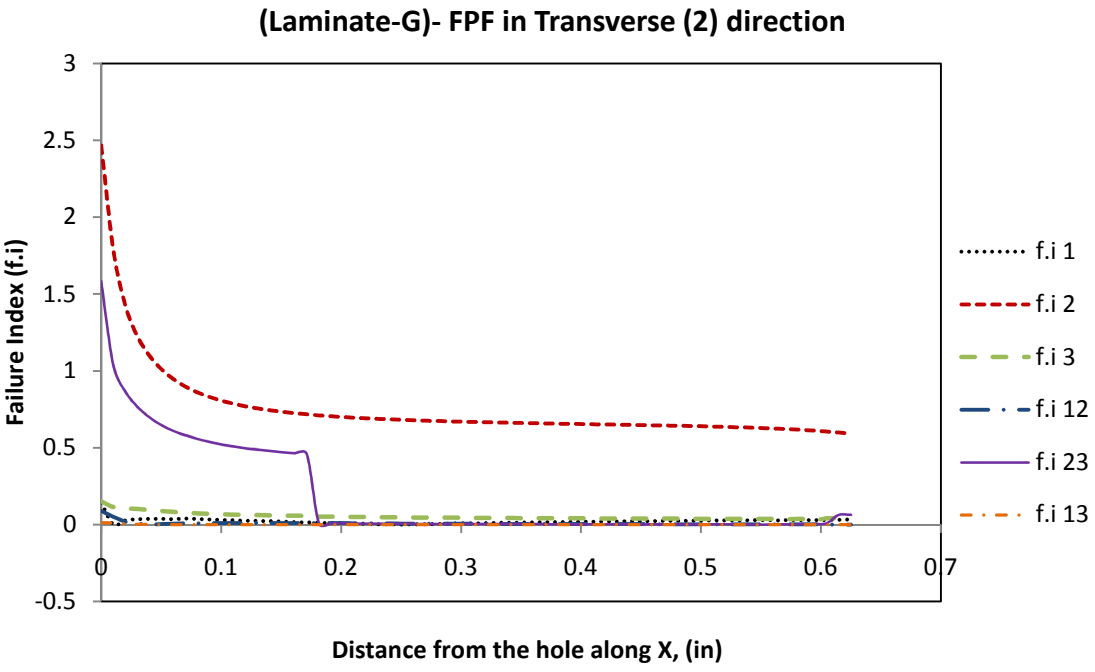
(Laminate-G)- FPF in Transverse (2) direction
Failure Index (f.i)
3
2.5
2
1.5
1
0.5
0
-0.5
0
0.1
0.2
0.3
0.4
0.5
0.6
0.7
Distance from the hole along X, (in)
f.i 1
f.i 2
f.i 3
f.i 12
f.i 23
f.i 13

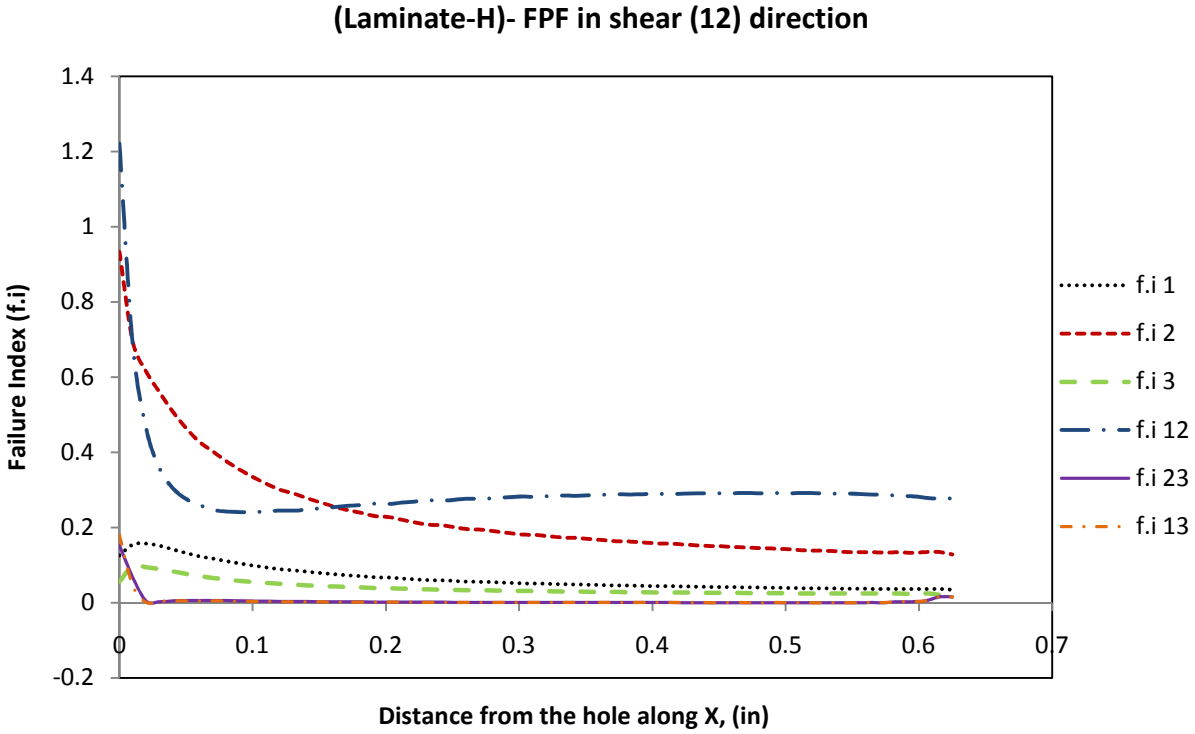
(Laminate-H)- FPF in shear (12) direction
Failure Index (f.i)
1.4
1.2
1
0.8
0.6
0.4
0.2
0
-0.2
0
0.1
0.2
0.3
0.4
0.5
0.6
0.7
Distance from the hole along X, (in)
f.i 1
f.i 2
f.i 3
f.i 12
f.i 23
f.i 13

Appendix A-4

Macro to calculate volume averaged stress in ANSYS

! Create macro to calculate average stress

*create,rve !,mac

/nopr

! Get element volume

ETABLE, ,VOLU

! Get element stress

ETABLE, ,S,X

ETABLE, ,S,Y

ETABLE, ,S,Z

ETABLE, ,S,XY

ETABLE, ,S,XZ

ETABLE, ,S,YZ

! Stress by element volume

!This is same as $\sigma_{ij} dv$

SMULT,SXV,VOLU,SX,1,1,

SMULT,SYV,VOLU,SY,1,1,

SMULT,SZV,VOLU,SZ,1,1,

SMULT,SXYV,VOLU,SXY,1,1,

SMULT,SXZV,VOLU,SXZ,1,1,

SMULT,SYZV,VOLU,SYZ,1,1,

SSUM

! Integer stress along total volume

!This is same as $\int_V \sigma_{ij} dv$

*get,totvol,ssum,,item,volu

*get,totsx ,ssum,,item,sxv

*get,totsy ,ssum,,item,syv

*get,totsz ,ssum,,item,szv

*get,totsxy ,ssum,,item,sxyv

*get,totsxz ,ssum,,item,sxzv

*get,totsyz ,ssum,,item,syzv

! Compute average RVE stress

!This is same as $\frac{1}{V}\int_V \sigma_{ij} dv$

Sxx0 = totsx/totvol

Syy0 = totsy/totvol

Szz0 = totsz/totvol

Sxy0 = totsxy/totvol

Sxz0 = totsxz/totvol

Syz0 = totsyz/totvol

/gopr

*end !srecover

/POST1 ! Post-processor module

SET,1 ! First column coefficients

! First column coefficients

!As explained in the sec. 5.5.1-5.5.6 only 3 load steps are needed to find all the

!elastic properties of the composite.

*use,Rve

C11 = Szz0

C12 = Sxx0

SET,2 ! Second column coefficients

*use,Rve

C22 = Sxx0

C23 = Syy0

SET,3 ! Sixth column coefficients

*use,Rve

C66 = Sxz0

E1=C11-2*C12*C12/(C22+C23)

E2 = (C11*(C22+C23)-2*C12*C12)*(C22-C23)/(C11*C22-C12*C12)

Nu12 = C12/(C22+C23)

Nu23 = (C11*C23-C12*C12)/(C11*C22-C12*C12)

G23 = (C22-C23)/2 ! or GT=E1/(2(1+Nu23))

G12=C66

FINISH ! Exit post-processor module